



Characterization of Magnetospheric Spacecraft Charging Environments Using the LANL Magnetospheric Plasma Analyzer Data Set

V.A. Davis, M.J. Mandell, and M.F. Thomsen

Science Applications International Corporation, San Diego, California



Prepared for Marshall Space Flight Center
under H-Order 32492D
and sponsored by
the Space Environments and Effects Program
managed at the Marshall Space Flight Center

The NASA STI Program Office...in Profile

Since its founding, NASA has been dedicated to the advancement of aeronautics and space science. The NASA Scientific and Technical Information (STI) Program Office plays a key part in helping NASA maintain this important role.

The NASA STI Program Office is operated by Langley Research Center, the lead center for NASA's scientific and technical information. The NASA STI Program Office provides access to the NASA STI Database, the largest collection of aeronautical and space science STI in the world. The Program Office is also NASA's institutional mechanism for disseminating the results of its research and development activities. These results are published by NASA in the NASA STI Report Series, which includes the following report types:

- **TECHNICAL PUBLICATION.** Reports of completed research or a major significant phase of research that present the results of NASA programs and include extensive data or theoretical analysis. Includes compilations of significant scientific and technical data and information deemed to be of continuing reference value. NASA's counterpart of peer-reviewed formal professional papers but has less stringent limitations on manuscript length and extent of graphic presentations.
- **TECHNICAL MEMORANDUM.** Scientific and technical findings that are preliminary or of specialized interest, e.g., quick release reports, working papers, and bibliographies that contain minimal annotation. Does not contain extensive analysis.
- **CONTRACTOR REPORT.** Scientific and technical findings by NASA-sponsored contractors and grantees.

- **CONFERENCE PUBLICATION.** Collected papers from scientific and technical conferences, symposia, seminars, or other meetings sponsored or cosponsored by NASA.
- **SPECIAL PUBLICATION.** Scientific, technical, or historical information from NASA programs, projects, and mission, often concerned with subjects having substantial public interest.
- **TECHNICAL TRANSLATION.** English-language translations of foreign scientific and technical material pertinent to NASA's mission.

Specialized services that complement the STI Program Office's diverse offerings include creating custom thesauri, building customized databases, organizing and publishing research results...even providing videos.

For more information about the NASA STI Program Office, see the following:

- Access the NASA STI Program Home Page at <http://www.sti.nasa.gov>
- E-mail your question via the Internet to help@sti.nasa.gov
- Fax your question to the NASA Access Help Desk at (301) 621-0134
- Telephone the NASA Access Help Desk at (301) 621-0390
- Write to:
NASA Access Help Desk
NASA Center for AeroSpace Information
7121 Standard Drive
Hanover, MD 21076-1320
(301)621-0390



Characterization of Magnetospheric Spacecraft Charging Environments Using the LANL Magnetospheric Plasma Analyzer Data Set

V.A. Davis, M.J. Mandell, and M.F. Thomsen

Science Applications International Corporation, San Diego, California

Prepared for Marshall Space Flight Center
under H-Order 32492D
and sponsored by
the Space Environments and Effects Program
managed at the Marshall Space Flight Center

National Aeronautics and
Space Administration

Marshall Space Flight Center • MSFC, Alabama 35812

Acknowledgments

This effort was accomplished with resources provided by NASA's Living With a Star (LWS) Space Environment Testbeds (SET) Program.



Available from:

NASA Center for AeroSpace Information
7121 Standard Drive
Hanover, MD 21076-1320
(301) 621-0390

National Technical Information Service
5285 Port Royal Road
Springfield, VA 22161
(703) 487-4650

CONTENTS

Figures.....	iv
Tables	xiii
1 Objective	1
2 Summary of Work Completed.....	1
2.1 Reports, Meetings, Presentation, and Publication.....	3
2.2 Conclusions	4
3 Data	4
3.1 Spectra Of A Charged Spacecraft	5
3.2 Adjusting Spectra To Account For Chassis Potential	7
3.3 Spectra Of An Uncharged Spacecraft	8
3.4 Spectra In Sunlight	9
4 Moments.....	9
5 Fluxes	24
6 Chassis Potential Computation.....	30
6.1 Net Current	30
6.2 Zero In Net Current	31
6.3 Error Bars	32
6.4 Results	32
7 Calculational Techniques	33
7.1 Yield Functions	33
7.2 High Energy Extrapolation.....	41
7.3 Low Energy Electron Cutoff.....	42
7.4 Fraction Of Low Energy Electrons Escaping.....	45
7.5 Modeling Sunlit Charging	48
7.6 Alternative Predictors.....	51
8 Comparison Of Solar Maximum And Solar Minimum	53
9 Comparison With Data From Another LANL Spacecraft	56
10 Fitting Techniques And Results.....	57
11 References	94

Figures

Figure	Page
1 Ion fluxes at day 245.70276, with spacecraft at -2800.	6
2 Electron fluxes at day 245.70276, with spacecraft at -2800 V. The vertical line of triangles is locally created electrons.	7
3 Measured electron and ion spectra at day 244.69426 with chassis at -5.4 V.	8
4 Spectra over a 144-minute period on day 272 of 2001, starting in eclipse. The spectra with the higher fluxes at lower energies are sunlit. The potential as determined by the ion line ranges between -6339 V and -948 V in eclipse and between -718 V and -141 V in sunlight. The line is the flux corresponding to one-count.	9
5 Validity of electron density moment calculational technique for eclipse data.	11
6 Validity of electron density moment calculational technique for sunlit data.	11
7 Validity of electron temperature moment calculational technique for eclipse data. LANL uses the full angular spectrum to compute temperatures parallel and perpendicular to the magnetic field.....	12
8 Validity of electron temperature moment calculational technique for sunlit data. LANL uses the full angular spectrum to compute temperatures parallel and perpendicular to the magnetic field.....	12
9 Validity of ion density moment calculational technique in eclipse. Integral using full angular spectrum gives higher densities than spin-averaged spectrum.	13
10 Validity of ion density moment calculational technique in sunlight. Integral using full angular spectrum gives higher densities than spin-averaged spectrum.	13
11 Validity of low energy ion density moment calculational technique in eclipse. Spectra for chassis potential more negative than -100 V have a low energy ion density of zero...14	14
12 Validity of low energy ion density moment calculational technique in sunlight. Spectra for chassis potential more negative than -100 V have a low energy ion density of zero.	14
13 Validity of ion temperature moment calculational technique in eclipse. Integral using full angular spectrum gives lower temperatures than spin-averaged spectrum.	15
14 Validity of ion temperature moment calculational technique in sunlight. Integral using full angular spectrum gives lower temperatures than spin-averaged spectrum.	15
15 Validity of ion temperature moment calculational technique in eclipse using density from full angular spectrum.....	16

16	Validity of ion temperature moment calculational technique in sunlight using density from full angular spectrum.....	17
17	Temperature-density relationship for electrons during eclipse. Points plotted with open triangles have a value of $\theta n^{0.75} < 300 \text{ eVcm}^{-2.25}$	18
18	Temperature-density relation for electrons in sunlit data. Points plotted with open triangles have a value of $\theta n^{0.75} < 300 \text{ eVcm}^{-2.25}$	18
19	Temperature-density relationship for ions in eclipse.....	19
20	Temperature-density relationship for ions in sunlight.	19
21	Ion and electron densities are correlated and comparable in eclipse. Points plotted with open triangles have a value of $\theta n^{0.75} < 300 \text{ eVcm}^{-2.25}$ for electrons.....	20
22	Ion and electron densities are correlated and comparable in sunlight. Points plotted with open triangles have a value of $\theta n^{0.75} < 300 \text{ eVcm}^{-2.25}$ for electrons.....	20
23	Ion and electron temperatures are independent in eclipse. Ion temperatures are generally higher and vary less. Points plotted with open triangles have a value of $\theta n^{0.75} < 300 \text{ eVcm}^{-2.25}$ for electrons.....	21
24	Ion and electron temperatures are independent in sunlight. Ion temperatures are higher and vary less. Points plotted with open triangles have a value of $\theta n^{0.75} < 300 \text{ eVcm}^{-2.25}$ for electrons.....	21
25	Correlation between chassis potential and electron temperature in eclipse. Points plotted with open triangles have a value of $\theta n^{0.75} < 300 \text{ eVcm}^{-2.25}$ for electrons.....	22
26	Correlation between chassis potential and electron temperature in sunlight. Points plotted with open triangles have a value of $\theta n^{0.75} < 300 \text{ eVcm}^{-2.25}$ for electrons.....	23
27	Correlation between chassis potential and electron temperature in eclipse. Points plotted with open triangles have a value of $\theta n^{0.75} < 300 \text{ eVcm}^{-2.25}$ for electrons.....	23
28	Correlation between chassis potential and electron temperature in sunlight. Points plotted with open triangles have a value of $\theta n^{0.75} < 300 \text{ eVcm}^{-2.25}$ for electrons.....	24
29	Electron fluxes at all potentials in eclipse.....	25
30	Electron fluxes at all potentials in sunlight.....	26
31	Ion fluxes at all potentials in eclipse.....	26
32	Ion fluxes at all potentials in sunlight.	27

33	Net flux in eclipse. A complete spectrum, correct yield functions, and proper accounting for suppression of secondaries by barriers would give a value of zero for all potentials.	28
34	Net flux in sunlight. The net flux, as defined here, does NOT include photoemission. The photoemission needed for current balance is increasing with potential.	28
35	Net flux in eclipse.	29
36	Net flux in sunlight.	29
37	For Sept 01 eclipse data, measured potential as a function of the potential computed from the zero in the net flux. The lines are $y = 1.5 x$ and $y = x/1.5$. The bar chart at the right shows the number of spectra for which no solution was found for each value of measured potential. These points are represented in the plot on the left by a single diamond along the left hand axis.	32
38	For Sept 01, eclipse data, measured potential as a function of the potential computed from the minimum in the net flux. The lines are $y = 1.5 x$ and $y = x/1.5$. The bar chart at the right shows the number of spectra for which no solution was found for each value of measured potential.	33
39	Secondary electron yield from incident electron impact for materials defined in the SEE Spacecraft Charging Handbook and the Carbon material used here.	35
40	Backscattered electron yield from incident electron impact for materials defined in the SEE Spacecraft Charging Handbook and the Carbon material used here.	35
41	Sum of secondary and backscattered electron yields from incident electron impact for materials defined in the SEE Spacecraft Charging Handbook and the Carbon material used here.	36
42	Secondary electron yields from incident ion impact for materials defined in the SEE Spacecraft Charging Handbook and the Carbon material used here.	36
43	Net flux in eclipse using material properties of Gold as defined in the SEE Spacecraft Charging Handbook.	37
44	For Sept 01, eclipse data, measured potential as a function of the potential computed from the minimum in the net flux using material properties of Gold as defined in the SEE Spacecraft Charging Handbook.	37
45	Net flux in eclipse using material properties of Kapton as defined in the SEE Spacecraft Charging Handbook.	38
46	For Sept 01, eclipse data, measured potential as a function of the potential computed from the minimum in the net flux using material properties of Kapton as defined in the SEE Spacecraft Charging Handbook.	38

47	Net flux in eclipse using material properties of Solar cell coverglass material as defined in the SEE Spacecraft Charging Handbook.	39
48	For Sept 01, eclipse data, measured potential as a function of the potential computed from the minimum in the net flux using material properties of Solar cell coverglass material as defined in the SEE Spacecraft Charging Handbook.....	39
49	Net flux in eclipse using material properties of OSR as defined in the SEE Spacecraft Charging Handbook.	40
50	For Sept 01, eclipse data, measured potential as a function of the potential computed from the minimum in the net flux using material properties of OSR as defined in the SEE Spacecraft Charging Handbook.	40
51	Net flux in eclipse including contribution from extrapolated fluxes.	41
52	Net flux in sunlight, including contribution from extrapolated fluxes.	42
53	Minimum energy used in the calculations up to this point (LANL barrier) and an alternative as a function of potential for sunlit calculations.	43
54	Net flux in eclipse using “alternative barrier” as the minimum electron energy.....	43
55	For Sept 01, eclipse data, measured potential as a function of the potential computed from the minimum in the net flux using “alternative barrier” as the minimum electron energy.....	44
56	Net flux in sunlight using “alternative barrier” as the minimum electron energy.	44
57	Measures of escaping and returning low energy fluxes in eclipse.....	46
58	Measures of escaping and returning low energy fluxes in sunlight.....	46
59	Net flux in eclipse with alternative minimum electron energy and 81% escape fraction.	47
60	For Sept 01, eclipse data, measured potential as a function of the potential computed from the minimum in the net flux with alternative minimum electron energy and 81% escape fraction.	47
61	Net flux in sunlight with alternative minimum electron energy, 81% escape fraction, and ignoring photoemission.....	49
62	For Sept 01, sunlit data, assuming 81% of the secondary electrons escape, and ignoring photoemission, measured potential as a function of potential computed from the minimum in the net flux. The lines are $y = 1.5 x$ and $y = x/1.5$	49
63	Average net flux (ignoring photoemission) as a function of potential for the Sept 01, sunlit dataset. The line is a fit to the average net flux for potentials between -30 and -948 V.....	50

64	Net flux in sunlight with alternative minimum electron energy, 81% escape fraction, and including photoemission.	50
65	For Sept 01, sunlit data, assuming 81% of the secondary electrons escape, and including photoemission, measured potential as a function of potential computed from the minimum in the net flux. The lines are $y = 1.5x$ and $y = x/1.5$. The bar chart at the right shows the number of spectra for which no solution was found for each value of measured potential. These points are represented in the plot on the left by a single diamond along the left hand axis.....	51
66	For Sept 01, eclipse data, measured potential as a function of $\phi = 1.74 \times 10^{-5} \theta^{2.26}$ for eclipse Sept 01 dataset.	52
67	For Sept 01, sunlit data, measured potential as a function of $\phi = 2.4 \times 10^{-7} \theta^{2.51}$ for sunlit Sept 01 dataset.	52
68	For Sept 01, eclipse data, measured potential as a function of $1.359 \times 10^{-12} \sum_{E>9123} (\text{measured flux} \times \text{bin width})^{2.03}$ for sunlit Sept 01 dataset.	53
69	For Sept 96, net flux in eclipse with alternative minimum electron energy and 81% escape fraction. (Compare with Figure 59.).....	54
70	For Sept 96, eclipse data, assuming 81% of the secondary electrons escape, measured potential as a function of potential computed from the minimum in the net flux. (Compare with Figure 60.).....	54
71	For Sept 96, net flux in sunlight with alternative minimum electron energy, 81% escape fraction, and including photoemission. (Compare with Figure 64.)	55
72	For Sept 96, sunlit data, assuming 81% of the secondary electrons escape, and including photoemission, measured potential as a function of potential computed from the minimum in the net flux. (Compare with Figure 65.).....	55
73	For LANL 97 spacecraft, net flux in eclipse with alternative minimum electron energy and 81% escape fraction. (Compare with Figure 59.).....	56
74	For Sept 01, eclipse data from LANL 97 spacecraft, assuming 81% of the secondary electrons escape, measured potential as a function of potential computed from the minimum in the net flux. (Compare with Figure 60.).....	56
75	A sample charging flux spectrum and various fits to it using different functional forms.	60
76	A sample non-charging flux spectrum and various fits to it using different functional forms.	60
77	Electron density computed from data compared with electron density computed from fit to Maxwellian. Integral over fit extends from 1 eV to 100 keV.	61

78	Electron temperature computed from data compared with electron temperature computed from fit to Maxwellian. Integral over fit extends from 1 eV to 100 keV.....	61
79	Ion density computed from data compared with ion density computed from fit to Maxwellian. Integral over fit extends from 1 eV to 100 keV.	62
80	Ion temperature computed from data compared with ion temperature computed from fit to Maxwellian. Integral over fit extends from 1 eV to 100 keV.	62
81	Electron density computed from data compared with electron density computed from fit to Single Maxwellian. Integral over fit extends from 1 eV to 100 keV.	63
82	Electron temperature computed from data compared with electron temperature computed from fit to Single Maxwellian. Integral over fit extends from 1 eV to 100 keV.	63
83	Ion density computed from data compared with ion density computed from fit to Single Maxwellian. Integral over fit extends from 1 eV to 100 keV.....	64
84	Ion temperature computed from data compared with ion temperature computed from fit to Single Maxwellian. Integral over fit extends from 1 eV to 100 keV.	64
85	Electron density computed from data compared with electron density computed from fit to Double Maxwellian. Integral over fit extends from 1 eV to 100 keV.	65
86	Electron temperature computed from data compared with electron temperature computed from fit to Double Maxwellian. Integral over fit extends from 1 eV to 100 keV.	65
87	Ion density computed from data compared with ion density computed from fit to Double Maxwellian. Integral over fit extends from 1 eV to 100 keV.	66
88	Ion temperature computed from data compared with ion temperature computed from fit to Double Maxwellian. Integral over fit extends from 1 eV to 100 keV.	66
89	Electron density computed from data compared with electron density computed from fit to Kappa. Integral over fit extends from 1 eV to 100 keV.....	67
90	Electron temperature computed from data compared with electron temperature computed from fit to Kappa. Integral over fit extends from 1 eV to 100 keV.	67
91	Ion density computed from data compared with ion density computed from fit to Kappa. Integral over fit extends from 1 eV to 100 keV.....	68
92	Ion temperature computed from data compared with ion temperature computed from fit to Kappa. Integral over fit extends from 1 eV to 100 keV.....	68
93	Electron density computed from data compared with electron density computed from fit to Maxwellian. Integral over fit only includes energy bins used to create fit.	69

94	Electron temperature computed from data compared with electron temperature computed from fit to Maxwellian. Integral over fit only includes energy bins used to create fit.	69
95	Ion density computed from data compared with ion density computed from fit to Maxwellian. Integral over fit only includes energy bins used to create fit.....	70
96	Ion temperature computed from data compared with ion temperature computed from fit to Maxwellian. Integral over fit only includes energy bins used to create fit.	70
97	Electron density computed from data compared with electron density computed from fit to Single Maxwellian. Integral over fit only includes energy bins used to create fit.	71
98	Electron temperature computed from data compared with electron temperature computed from fit to Single Maxwellian. Integral over fit only includes energy bins used to create fit.	71
99	Ion density computed from data compared with ion density computed from fit to Single Maxwellian. Integral over fit only includes energy bins used to create fit.....	72
100	Ion temperature computed from data compared with ion temperature computed from fit to Single Maxwellian. Integral over fit only includes energy bins used to create fit.	72
101	Electron density computed from data compared with electron density computed from fit to Double Maxwellian. Integral over fit only includes energy bins used to create fit.	73
102	Electron temperature computed from data compared with electron temperature computed from fit to Double Maxwellian. Integral over fit only includes energy bins used to create fit.	73
103	Ion density computed from data compared with ion density computed from fit to Double Maxwellian. Integral over fit only includes energy bins used to create fit.	74
104	Ion temperature computed from data compared with ion temperature computed from fit to Double Maxwellian. Integral over fit only includes energy bins used to create fit.	74
105	Electron density computed from data compared with electron density computed from fit to Kappa. Integral over fit only includes energy bins used to create fit.....	75
106	Electron temperature computed from data compared with electron temperature computed from fit to Kappa. Integral over fit only includes energy bins used to create fit.	75
107	Ion density computed from data compared with ion density computed from fit to Kappa. Integral over fit only includes energy bins used to create fit.	76
108	Ion temperature computed from data compared with ion temperature computed from fit to Kappa. Integral over fit only includes energy bins used to create fit.....	76

109	Electron fluxes in eclipse computed from Maxwellian fit at all potentials. Integral extends from 1 eV to 100 keV.	77
110	Ion fluxes in eclipse computed from Maxwellian fit at all potentials. Integral extends from 1 eV to 100 keV.	77
111	Net flux in eclipse computed from Maxwellian fit at all potentials. Integral extends from 1 eV to 100 keV.	78
112	Measured potential as a function of the potential computed from the minimum in the net flux, where the fluxes are computed from Maxwellian fits to the electron and ion fluxes.	78
113	Electron fluxes in eclipse computed from Single Maxwellian fit at all potentials. Integral extends from 1 eV to 100 keV.	79
114	Ion fluxes in eclipse computed from Single Maxwellian fit at all potentials. Integral extends from 1 eV to 100 keV.	79
115	Net fluxes in eclipse computed from Single Maxwellian fit at all potentials. Integral extends from 1 eV to 100 keV.	80
116	Measured potential as a function of the potential computed from the minimum in the net flux, where the fluxes are computed from Single Maxwellian fits to the electron and ion fluxes.	80
117	Electron fluxes in eclipse computed from Double Maxwellian fit at all potentials. Integral extends from 1 eV to 100 keV.	81
118	Ion fluxes in eclipse computed from Double Maxwellian fit at all potentials. Integral extends from 1 eV to 100 keV.	81
119	Net fluxes in eclipse computed from Double Maxwellian fit at all potentials. Integral extends from 1 eV to 100 keV.	82
120	Measured potential as a function of the potential computed from the minimum in the net flux, where the fluxes are computed from Double Maxwellian fits to the electron and ion fluxes.	82
121	Electron fluxes in eclipse computed from Kappa fit at all potentials. Integral extends from 1 eV to 100 keV.	83
122	Ion fluxes in eclipse computed from Kappa fit at all potentials. Integral extends from 1 eV to 100 keV.	83
123	Net fluxes in eclipse computed from Kappa fits at all potentials. Integral extends from 1 eV to 100 keV.	84
124	Measured potential as a function of the potential computed from the minimum in the net flux, where the fluxes are computed from Kappa fits to the electron and ion fluxes.	84

125	Measured potential computed from the minimum in the net flux, where the fluxes are computed from a Maxwellian fit to the electron flux and a Single Maxwellian fit to the ion flux.	85
126	Measured potential computed from the minimum in the net flux, where the fluxes are computed from a Maxwellian fit to the electron flux and a Double Maxwellian fit to the ion flux.	85
127	Measured potential computed from the minimum in the net flux, where the fluxes are computed from a Maxwellian fit to the electron flux and a Kappa fit to the ion flux.	86
128	Measured potential computed from the minimum in the net flux, where the fluxes are computed from a Single Maxwellian fit to the electron flux and a Maxwellian fit to the ion flux.	86
129	Measured potential computed from the minimum in the net flux, where the fluxes are computed from a Single Maxwellian fit to the electron flux and a Double Maxwellian fit to the ion flux.	87
130	Measured potential computed from the minimum in the net flux, where the fluxes are computed from a Single Maxwellian fit to the electron flux and a Kappa fit to the ion flux.	87
131	Measured potential computed from the minimum in the net flux, where the fluxes are computed from a Double Maxwellian fit to the electron flux and a Maxwellian fit to the ion flux.	88
132	Measured potential computed from the minimum in the net flux, where the fluxes are computed from a Double Maxwellian fit to the electron flux and a Single Maxwellian fit to the ion flux.	88
133	Measured potential computed from the minimum in the net flux, where the fluxes are computed from a Double Maxwellian fit to the electron flux and a Kappa fit to the ion flux.	89
134	Measured potential computed from the minimum in the net flux, where the fluxes are computed from a Kappa fit to the electron flux and a Maxwellian fit to the ion flux.	89
135	Measured potential computed from the minimum in the net flux, where the fluxes are computed from a Kappa fit to the electron flux and a Single Maxwellian fit to the ion flux.	90
136	Measured potential computed from the minimum in the net flux, where the fluxes are computed from a Kappa fit to the electron flux and a Double Maxwellian fit to the ion flux.	90
137	Net fluxes in eclipse at all potentials with electron fluxes computed from Kappa fit and ion fluxes computed from Kappa fit. Integral extends from 1 eV to 100 keV.	91

Tables

Table	Page
1 Material properties used average material “Carbon”	34
2 Quality of potential predictions made from various fits to measured incident fluxes.....	92
3 Comparison of the accuracy of potential predictions from the fits when the flux integrals was done using only those energy bins used to create the flux and when the flux integrals extended from 1 eV to 100 keV.	93

1 Objective

The objective of this contract is to use the detailed particle energy spectra measured by the Los Alamos Magnetospheric Plasma Analyzer (MPA) on several satellites in geosynchronous orbit to model the potential of the chassis due to surface charging of those satellites, as derived also from MPA measurements. In particular, we seek to identify a relatively simple characterization of the full particle distributions that yields an accurate prediction of the observed charging under a wide variety of conditions. The three-dimensional computer codes that can compute spacecraft charging in a tenuous plasma (NASCAP/GEO [Katz, *et al.*, 1979], SEE Spacecraft Charging Handbook [Katz, *et al.*, 2000], and NASCAP-2K [Davis *et al.*, 2002]) assume that the environment can be adequately modeled by a Maxwellian or Double Maxwellian distribution function. We seek to verify this or determine an appropriate alternative formulation.

2 Summary of Work Completed

In preparation for this effort, we reviewed three previous closely related studies: [Garrett, *et al.*, 1980], [Lai, *et al.*, 2001], and an internal study done by LANL.

The measurements used in this study were taken by the LANL MPA, which is described in [Bame, *et al.*, 1993]. The determination of the spacecraft potential, the moments of the distribution, and the distribution function from the measurements are described in the following publications: [Lawrence, *et al.*, 1999], [McComas, *et al.*, 1993], [Thomsen, *et al.*, 1996], [Thomsen, *et al.*, 1999]. Very simplified descriptions of some of this processing are included below in order to explain how the measurements are being used in this project.

Seven datasets were constructed for this investigation. Each dataset record consists of an electron and an ion spin-averaged, differential flux spectrum, along with a time tag, the chassis potential derived from the ion line, and various moments of the distribution. The first two datasets consist of spectra from September 2001 for satellite 1994-084. These datasets were filtered for data quality and existence of an ion line. The first dataset was for spectra taken during eclipse while the second included times before and after eclipse. These datasets were used for construction and testing of the software needed to handle a large number of spectra at once.

After the preliminary investigation was complete and the bulk of the software built, five additional datasets were constructed. All the results reported here use these five datasets. Four of the datasets are from the satellite 1994-084. This includes two months near the peak of the solar cycle, March 2001 and September 2001, and two months near the minimum, March 1996 and September 1996. The fifth dataset is from September 2001 for the LANL-97a spacecraft. This final dataset allows us to confirm that our results are valid for a different spacecraft of the same design.

We developed software to examine a large number of spectra at once. The software, written in Java, does the following:

- Read in a dataset,
- Determine if the spacecraft is in eclipse or sunlight,

- Filter the dataset for sunlit/eclipse, presence of a potential computed from an ion line, and data quality,
- Compute the moments, fluxes, and derived potential described in this report from measured fluxes and analytic fits to measured fluxes,
- Fit a measured distribution function with an analytic form, and
- Compute statistical measures.

We created Excel workbooks to display the results as shown in this report and compute additional statistical measures.

For the various datasets, we computed electron and ion density and temperature moments for the measured spectra. The results verify that the calculations done at SAIC using the Java software using the spin-averaged spectrum give the same results as those done at LANL using the full angular distribution, with the exception of the density of ions with measured energies over 100 eV. The density and temperature moments of electrons with incident energies above 30 eV, the temperature moments of ions with incident energies above 100 eV, and the density moments of the ions with incident energies below 100 eV all agree well. The SAIC computed density moments of ions with incident energies above 100 eV are consistently lower than the LANL computed values. In addition to providing verification that the calculations are done correctly, doing these calculations allowed us to refine the calculational technique and become familiar with the data.

For the various datasets, we computed incident electron and ion fluxes, secondary electron fluxes from incident electron and ion impact, backscattered electron fluxes, and the resulting net fluxes. We investigated how material properties, some choices in techniques to do the energy integral, and assumptions regarding the fraction of low energy particles escaping effect the calculated net current.

We also investigated techniques to compute the photoemission fluxes. Geometric effects are important enough in the sunlit charging of the LANL spacecraft that current balance results in sunlight are more suggestive than quantitative.

In order to gain a better measure of the quality of our flux computations, we computed the spacecraft chassis potential that we expect given incident electron and ion spectra for the various datasets. This approach provides a better prediction of chassis potentials than the measured temperature or the integrated measured flux between 9 and 47 keV.

Using the measured spectra, we determined that computing the fluxes using a set of material properties for graphite carbon and a low-energy secondary electron escape fraction of 81%, gives computed potentials consistent with measured values. The estimated potential is within a factor of 1.5 of the measured potential 65% of the time and within a factor of 3 of the measured potential 87% of the time.

Our goal is to provide guidance to those doing spacecraft surface charging calculations. We compared the results of calculations using various simple analytic fits with calculations using the

data. We developed an automated fitting procedure and computed moments, fluxes, and predicted potentials using Maxwellian, Double Maxwellian, and Kappa distribution functional forms. Christon, *et al* [1989] have shown that the Kappa distribution, which is a Maxwellian at low energies and a power law at high energies, often provides a good fit to the quiescent plasma sheet environment. (The spectrum is typically much more complex during disturbed conditions [Christon, *et al*, 1991].)

The potentials computed using Maxwellian fits for both ions and electrons are within a factor of 1.5 of the measured potential 30 to 58% of the time and within a factor of 3 of the measured potential 61 to 71 % of the time, depending on the fitting procedure. Using a Kappa distribution for the electrons and a Maxwellian distribution for the ions gave results within a factor of 1.5 of the measured potential 65% of the time and within a factor of 3 of the measured potential 84% of the time. Potential predictions using the Kappa-Maxwellian fit combination gives results similar to those obtained from using the measured fluxes directly. Energy bins with spurious measurements must be discarded from the flux integral when using the measured fluxes directly. These energy bins and the energy range above the maximum measured can be included when using fit spectra. Using all energy bins from 1 eV to 100 keV does not improve the agreement.

2.1 Reports, Meetings, Presentation, and Publication

This report includes the conclusions of the year-long study, as well as, all the techniques used and the results previously reported. Appendix A includes the quarterly reports for the LANL portion of this effort, including the final report.

The kick-off presentation for this contract was held at SAIC in San Diego on January 29, 2002. The presentation summarized the intended work plan.

Dr. Davis (Principal investigator) and Dr. Thomsen (Co-Investigator) were able to meet in person three times to discuss this contract. Dr. Thomsen traveled to SAIC in San Diego, CA, to attend the contract kick-off meeting and discuss the initial work on this contract. Dr. Davis traveled to LANL in Las Alamos, NM, where we had a productive full day meeting during which we reviewed how the data is handled, how the various integrals are calculated, and the meaning of the results. We also took advantage of an unrelated meeting that Dr. Thomsen had in Los Angeles, CA, to meet in San Diego, CA, for a half-day, where we discussed the appropriate high energy cut off for the integrals and improved the explanation of the justification for the technique used to compute the potential given the incident fluxes.

A presentation at the Fall Meeting of the American Geophysical Union is included as Appendix B.

A paper summarizing the results of this study will be submitted to the *Journal of Geophysical Research*. This final report and the paper will make the results of this study available to other researchers.

2.2 Conclusions

The LANL dataset has proved to be a powerful tool for the investigation of spacecraft surface charging. The spectra provide the resolution and accuracy adequate for “post-diction” spacecraft charging calculations.

It is necessary to include all the current components--incident electrons and ions, secondary electrons, backscattered electrons, and photoelectrons--to accurately “post-dict” chassis potentials from measured spectra. Eclipse calculations provide good accuracy. Calculations in sunlit conditions were significantly less successful. Estimates of photoemission and fraction of low energy electrons escaping are strongly dependent on geometric effects and sun angle. The quality of the data is high enough that with additional effort, we believe that the photoemission as a function of sun angle and chassis potential could be determined. This procedure would only work if the spacecraft surfaces are primarily conducting, as are most geosynchronous spacecraft. Potential “post-dictions” using a Kappa distribution to fit the incident electron spectrum and a Maxwellian distribution to fit the incident ion spectrum give results similar to “post-dictions” using the measured spectra directly. Better results would be obtained if additional intelligence were added to the ion flux fitting procedure.

We recommend the addition of the Kappa distribution to the selection of options in the three-dimensional spacecraft charging codes. The addition of the capability of using measured fluxes would also be a useful addition to the NASCAP-2K software.

3 Data

The measurements used in this study were taken by Magnetospheric Plasma Analyzer (MPA) instruments built by the Los Alamos National Laboratory (LANL) and flown on a series of geosynchronous spacecraft. The MPA is a spherical-sector electrostatic analyzer with a bending angle of 60° . The field of view is divided into six separate but contiguous detectors covering the range of polar angle from about 25° to 155° . The satellite spin allows the instrument to view 360 degrees in azimuth, which is divided into 24 sectors of 15 degrees. Thus in one spin the MPA views ~92% of the unit sphere, divided into six polar by 24 azimuthal view directions. The spin axis of the spacecraft points continuously at the center of the Earth, so the two polar angle detectors which view nearly perpendicular to the spin axis give very complete pitch angle coverage. While the spacecraft spins through a 15° azimuthal sector, the MPA plate voltage is swept through 40 logarithmically spaced energy channels ranging from ~40 keV/e down to ~1 eV/e. A complete three-dimensional (40 energies x 24 azimuths x 6 polar angles) distribution is obtained in one 10-s spin. Since the same analyzer is used for ion and electron measurements (by changing the polarity of the plate voltage and channel electron multiplier bias [Bame *et al.*, 1993]), the ion and electron distributions are measured alternately. In 86 s, the instrument cycles through one three-dimensional electron distribution and two three-dimensional ion distributions, as described above, as well as three two-dimensional electron distributions and two high-angular-resolution modes [Bame *et al.*, 1993].

The determination of the spacecraft potential, the moments of the distribution, and the distribution function from the measurements are described in the following publications:

[Lawrence, *et al.*, 1999], McComas, *et al.*, 1993], [Thomsen, *et al.*, 1996], [Thomsen, *et al.*, 1999]. Simplified descriptions of some of this processing are included below in order to explain how the measurements are being used in this project.

Seven datasets were constructed. Each dataset record consists of an electron and an ion spin-averaged, differential flux spectrum, along with a time tag, the chassis potential derived from the ion line, and various moments of the distribution.

The first two datasets consist of spin-averaged, differential flux spectra from September 2001 for satellite 1994-084. The first dataset is confined to times when the spacecraft was between -0.6 and +0.5 local time; for almost all the points the spacecraft was in eclipse. The second dataset consists of measurements taken when the spacecraft was between 22.4 local time to +2.0 local time; both sunlit and eclipse data are included. These initial datasets include only spectra for which a clear potential determination can be made from the ion line. These initial two datasets consist of 839 and 1195 spectra respectively. These datasets were used for construction and testing of the software needed to compute moments and fluxes of a large number of spectra at once.

After the preliminary investigation was complete and the bulk of the software built, five additional datasets were constructed. All the results reported here use these five datasets. Four of the datasets are from the satellite 1994-084. This includes two months near the peak of the solar cycle, March 2001 and September 2001, and two months near the minimum, March 1996 and September 1996. (Solar cycle 23 began in May 1996 and peaked in April 2000.) The fifth dataset is from September 2001 for the LANL-97a spacecraft. This final dataset allows us to confirm that our results are valid for a different spacecraft of the same design.

The datasets include one record for each 86-second measurement period during the time period covered. The analysis software filters the data to keep only spectra for which the ion spectrum provides a distinct ion line to determine the potential along with sunlit/eclipse condition and acceptable data quality flags. Each record includes several derived quantities. The most important of these are the measured potential and its quality flag. Additionally, there are ion and electron densities and parallel and perpendicular temperatures, along with an estimated potential barrier height and its quality flag. The estimated potential barrier is the energy of the minimum electron count rate between 30 eV and 400 eV. Each record also includes a timestamp and the geocentric position from which the determination of sunlit or eclipse condition is made. Each of these quantities is further described in the section below on moments.

3.1 Spectra Of A Charged Spacecraft

Figure 1 and Figure 2 show the ion flux spectrum and the electron flux spectrum, respectively, for day 245.70276. (The fractional part of the day gives the time (GMT)). The points labeled “Flux at spacecraft” are the spin-averaged, measured fluxes. The points labeled “One-count” are the fluxes that would be measured if one particle hit one of the six detectors. This is an approximate value as the six detectors have different geometric factors and efficiencies. For this work, we treat flux values under twice the one-count rate as zero.

The energy channel in which the ion count rate increases dramatically determines the spacecraft potential. LANL computed values are used here. In Figure 1, the lowest energy channel with a significant count rate is 2450 to 3200 eV. The chassis potential is taken to be the geometric mean of the channel edges, -2800 V. An ion with nearly zero energy at infinity is accelerated to 2800 eV by the time it reaches the detector, which is why no ions are seen below the 2450 to 3200 eV energy channel. The negatively charged spacecraft repels electrons. An electron with energy of 2800 eV reaches the detector with zero energy, and lower energy electrons do not reach the detector at all. However, most of the electrons that reach the detector with energies of less than 30 eV (and on highly charged spacecraft, sometimes even 200 eV) are generated on the spacecraft surface or in the spacecraft vicinity. The low energy peak seen in Figure 2 is electrons trapped by differential charging electric fields.

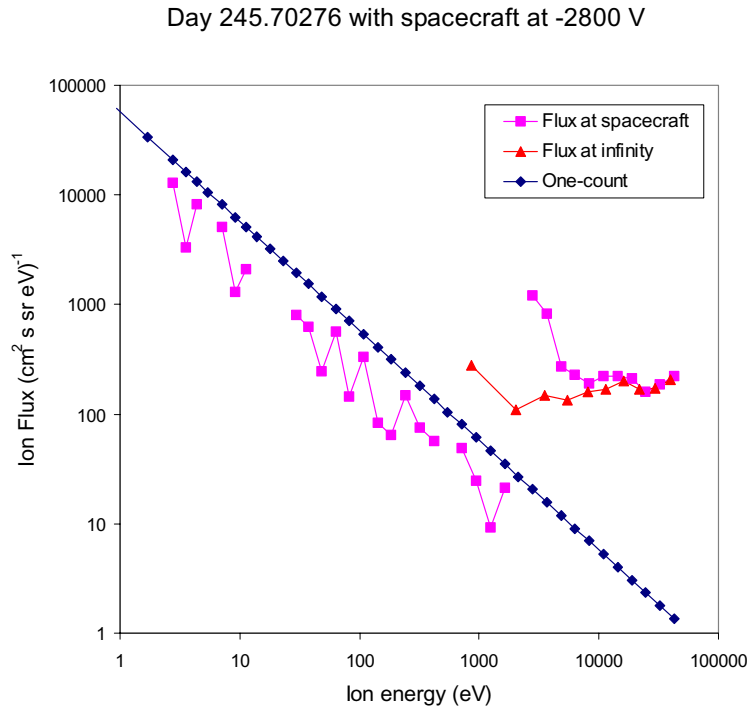


Figure 1. Ion fluxes at day 245.70276, with spacecraft at -2800.

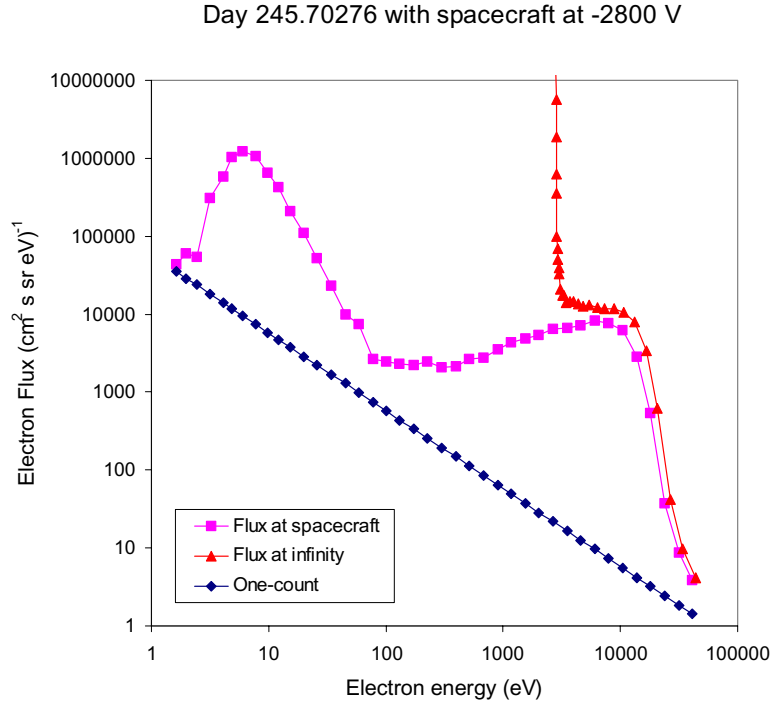


Figure 2. Electron fluxes at day 245.70276, with spacecraft at -2800 V. The vertical line of triangles is locally created electrons.

The accuracy of the energy of each measurement can be estimated as of the order of half the energy bin in which the measurement is made plus half the energy bin of the ion line. The accuracy of the flux is given by Poisson statistics to be the geometric mean of the measured spin-averaged flux and the one-count flux.

3.2 *Adjusting Spectra To Account For Chassis Potential*

The ambient fluxes can be derived from the fluxes at the spacecraft. The formula is derived from a consideration of the distribution function. The differential flux as a function of energy is related

to the distribution function by the formula $F(E) = \frac{2Ee^2}{m^2} f(E)$, where F is the flux and f is the distribution function. The measured energy is shifted from the energy at infinity by the potential; $E_m = E_\infty \mp \phi$, where the “-” sign is for ions and the “+” sign is for electrons.

Liouville’s theorem gives that “the density of system in the neighborhood of some given system in phase space remains constant in time.” [Goldstein, 1950a] Krall and Trivelpiece [1986] state Liouville’s theorem as “ $f(\mathbf{x}, \mathbf{v}, t)$ is constant along any particle trajectory.” For our purposes, we can state Liouville’s theorem as “if all possible particle trajectories that begin at the spacecraft end at infinity, the distribution function at the spacecraft is the same as the distribution function at infinity.” As we are treating the spacecraft as a uniform sphere, the potential varies only radially. All particles in a attractive radially symmetric potential field that varies more slowly than the inverse distance square connect to infinity. If the potential field varies faster than the

inverse distance squared, some particle trajectories both begin and end on the sphere due to angular momentum. [Goldstein, 1950b]. In a repulsive radially symmetric potential field, all particle trajectories connect to infinity.

As the distribution function at the spacecraft is the same as the distribution function at infinity, we have that

$$f_{\infty}(E_{\infty}) = f_m(E_m)$$

$$\frac{m^2}{2E_{\infty}} F_{\infty}(E_{\infty}) = \frac{m^2}{2E_m} F_m(E_m)$$

$$F_{\infty}(E_m \pm \phi) = F_m(E_m) \left(1 \pm \frac{\phi}{E_m} \right)$$

where the “+” sign is for ions and the “-” sign is for electrons.

Figure 1 and Figure 2 show the flux spectra shifted to infinity. The ion spectrum is fairly flat and the electron spectrum shows a spurious peak just above the spacecraft potential. The lower energy electrons were generated at the spacecraft surface and therefore do *not* reflect the properties of the spectrum at infinity.

3.3 Spectra Of An Uncharged Spacecraft

Figure 3 shows electron and ion flux spectra for an uncharged spacecraft (-5.4 V). The spectrum is definitely not Maxwellian. There is a low energy (about 7 eV) population for both species. The electron spectrum is very broad and steadily decreasing with energy. The ion flux is below measurable in the 30 to 1000 eV range and then approximately flat to the highest energies measured.

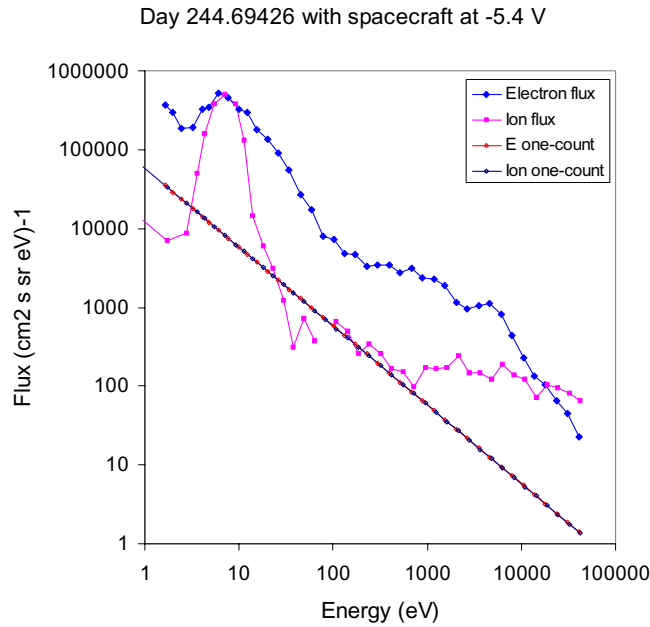


Figure 3. Measured electron and ion spectra at day 244.69426 with chassis at -5.4 V.

3.4 Spectra In Sunlight

Figure 4 shows how the electron spectra can change over time during eclipse and after eclipse exit. The lower set of curves were measured during eclipse, when the spacecraft chassis potential was -1 to -6 kV. The low energy electrons, which peak at about 10 eV, are secondary electrons trapped and accelerated by local electric fields (due to differential charging). When the spacecraft exits eclipse, the sunlit surfaces photoemit, generating a large number of low energy electrons. Some of these low-energy electrons are also trapped and accelerated by the local electric fields. Figure 4 shows enhanced fluxes up to about 60 eV.

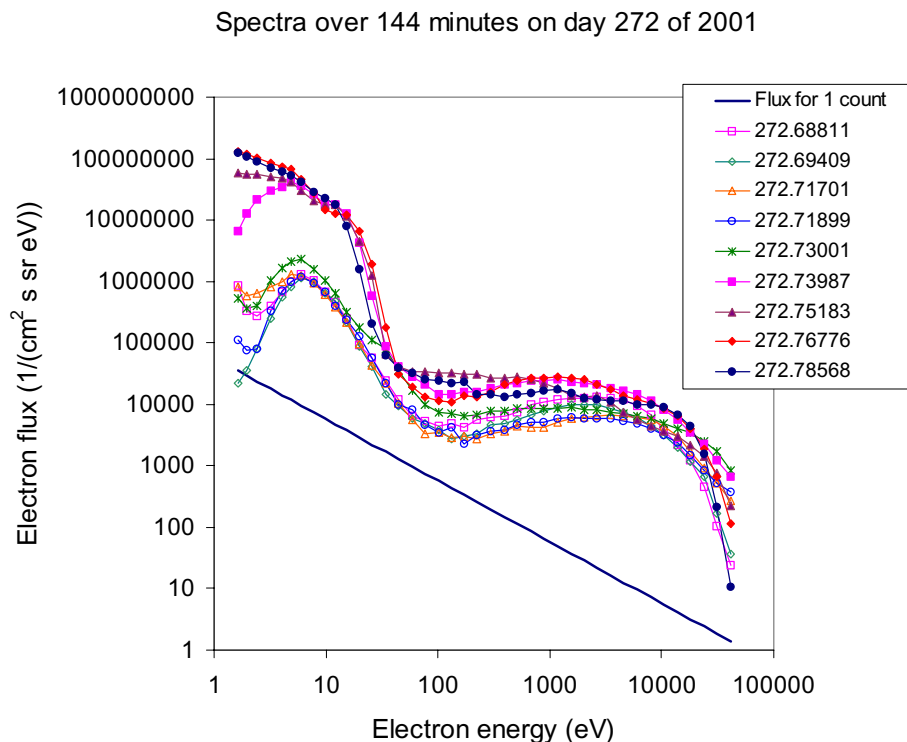


Figure 4. Spectra over a 144-minute period on day 272 of 2001, starting in eclipse. The spectra with the higher fluxes at lower energies are sunlit. The potential as determined by the ion line ranges between -6339 V and -948 V in eclipse and between -718 V and -141 V in sunlight. The line is the flux corresponding to one-count.

The position and the universal time can be used to determine if the spacecraft is sunlit and the incident sun direction. To do this, we implemented the GEOPACK algorithm developed at the Goddard Space Flight Center. We confirmed that the algorithm is implemented correctly by checking the location of the terminator. All of the spectra checked by hand were correctly identified as eclipse or sunlit.

4 Moments

For the various datasets, we computed electron and ion density and temperature moments for the measured spectra. The results verify that the calculations done at SAIC using the Java software using the spin-averaged spectrum give the same results as those done at LANL using the full

angular distribution, with the exception of the density of ions with measured energies over 100 eV. In addition to providing verification that the calculations are done correctly, doing these calculations allowed us to refine the calculational technique and become familiar with the data.

The phase space density is derived from the differential flux using the formula

$$f = \left(\frac{m^2}{2Ee^2} \right) F$$

where f is in $s^3 m^{-6}$, E is in eV, and F is in $(m^2 s sr eV)^{-1}$. The electron density and temperature moments are given by

$$n = \frac{4\pi e}{m} \sqrt{\frac{2e}{m}} \int_0^\infty f(E_\infty) \sqrt{E_\infty} dE_\infty = 2\pi \sqrt{\frac{2m}{e}} \sum_{E>E_{min}} \frac{F(E)}{E} \sqrt{E-\phi} \Delta E$$

$$\theta = \frac{2}{3en} \pi m \left(\frac{2e}{m} \right)^{5/2} \int_0^\infty f(E_\infty) \sqrt{E_\infty}^3 dE_\infty = 2\pi \frac{2}{3n} \sqrt{\frac{2m}{e}} \sum_{E>E_{min}} \frac{F(E)}{E} (E-\phi)^{3/2} \Delta E$$

where E_∞ is the energy at infinity, E is the geometric mean of the edges of the energy channel, and ΔE is the width of the energy channel. The value of E_{min} for electrons is the maximum of the barrier energy (the energy at which the minimum electron count rate between 30 eV and 400 eV is observed) and 30 eV. (There are some additional factors that go into the computation of E_{min} that are described in [Thomsen, *et al.*, 1999].) The value of E_{min} for ions is 124 eV. The minimum for electrons is chosen to filter out the secondary and photoelectrons accelerated by local electric fields into the MPA.

For ions, a “low energy” density is also computed in which the sum is over all energy bins *below* $E_{min} = 124$ eV.

The figures below show the density and temperature moments for electrons and ions in eclipse and in sunlight. While only the Sept 01 moments are shown here, the moments using the other datasets are similar.

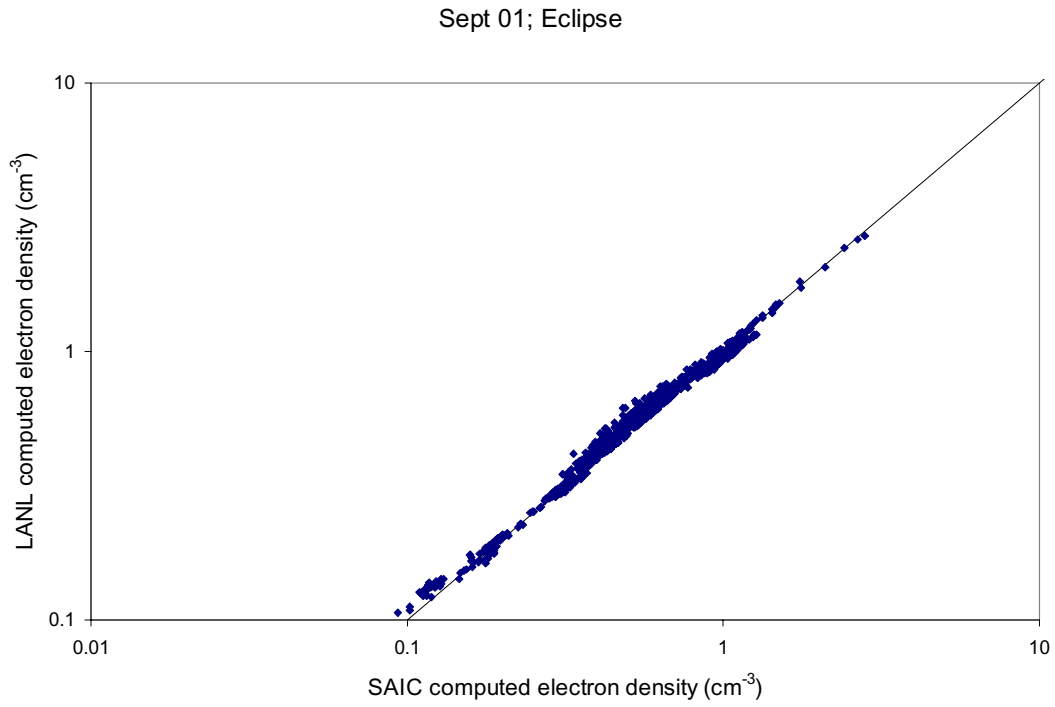


Figure 5. Validity of electron density moment calculational technique for eclipse data.

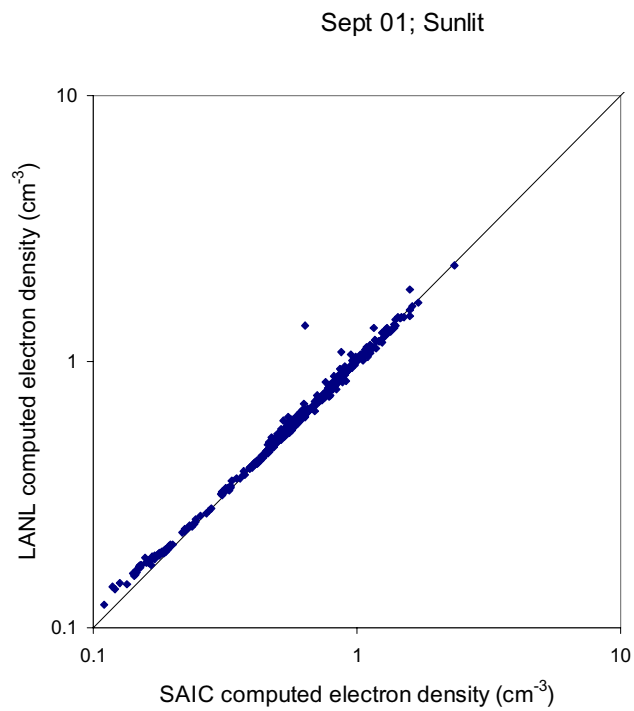


Figure 6. Validity of electron density moment calculational technique for sunlit data.

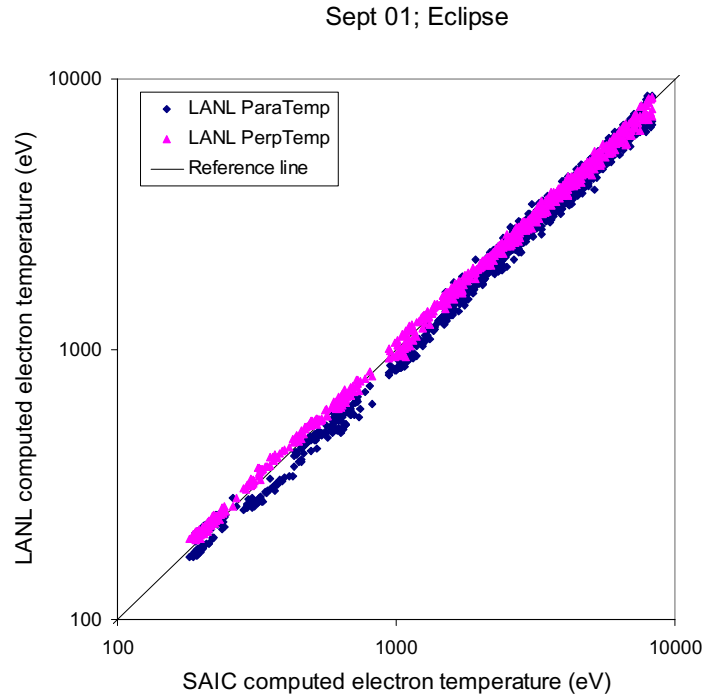


Figure 7. Validity of electron temperature moment calculational technique for eclipse data. LANL uses the full angular spectrum to compute temperatures parallel and perpendicular to the magnetic field.

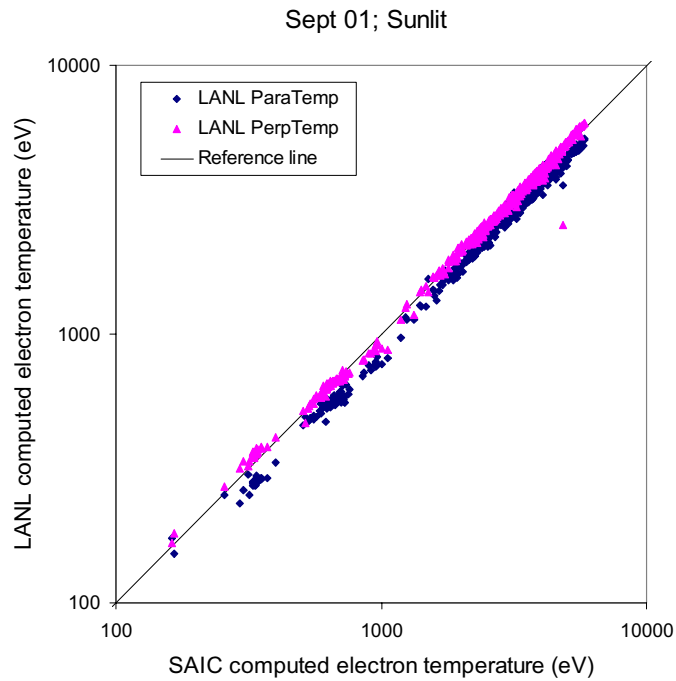


Figure 8. Validity of electron temperature moment calculational technique for sunlit data. LANL uses the full angular spectrum to compute temperatures parallel and perpendicular to the magnetic field.

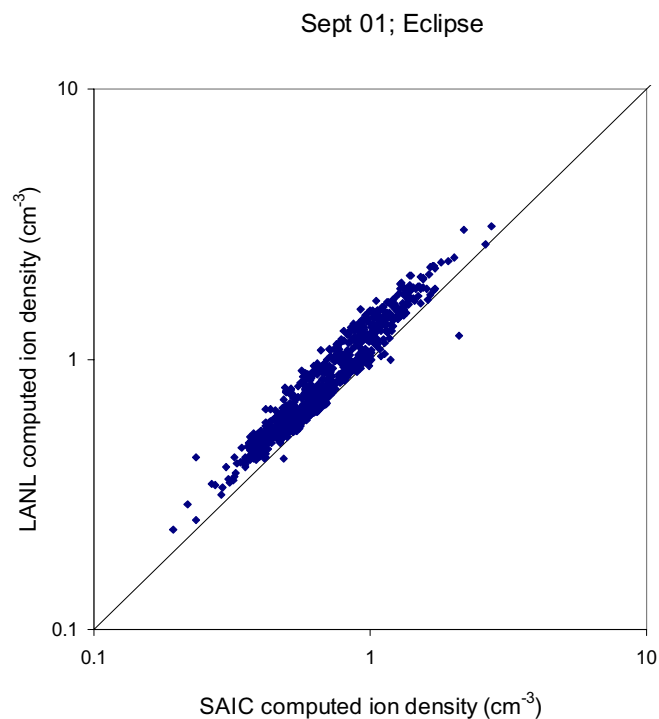


Figure 9. Validity of ion density moment calculational technique in eclipse. Integral using full angular spectrum gives higher densities than spin-averaged spectrum.

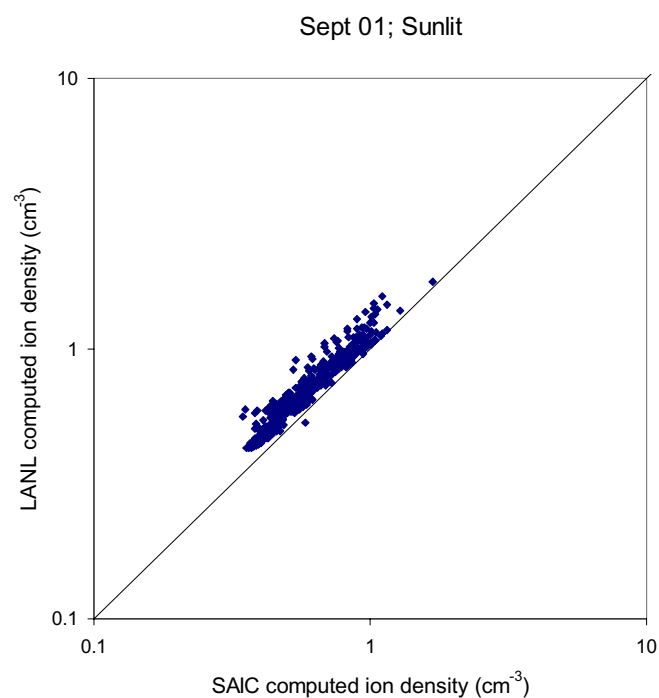


Figure 10. Validity of ion density moment calculational technique in sunlight. Integral using full angular spectrum gives higher densities than spin-averaged spectrum.

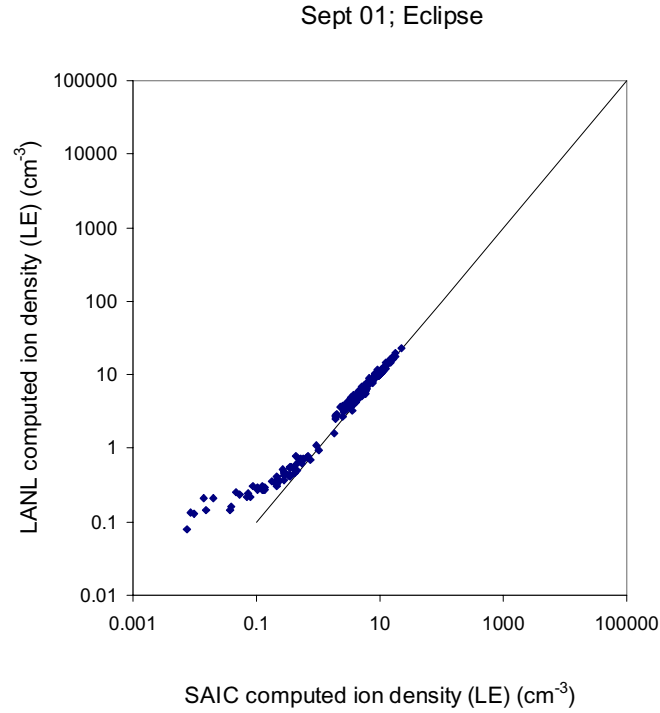


Figure 11. Validity of low energy ion density moment calculational technique in eclipse. Spectra for chassis potential more negative than -100 V have a low energy ion density of zero.

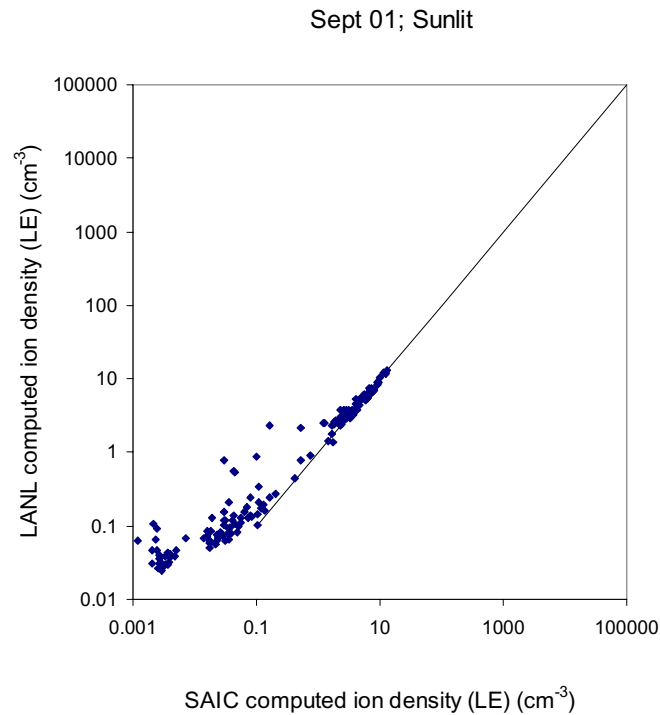


Figure 12. Validity of low energy ion density moment calculational technique in sunlight. Spectra for chassis potential more negative than -100 V have a low energy ion density of zero.

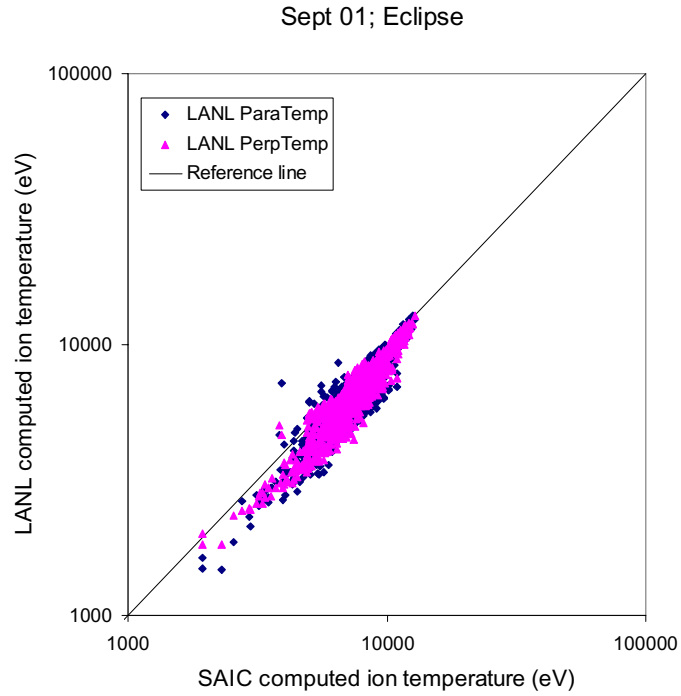


Figure 13. Validity of ion temperature moment calculational technique in eclipse. Integral using full angular spectrum gives lower temperatures than spin-averaged spectrum.

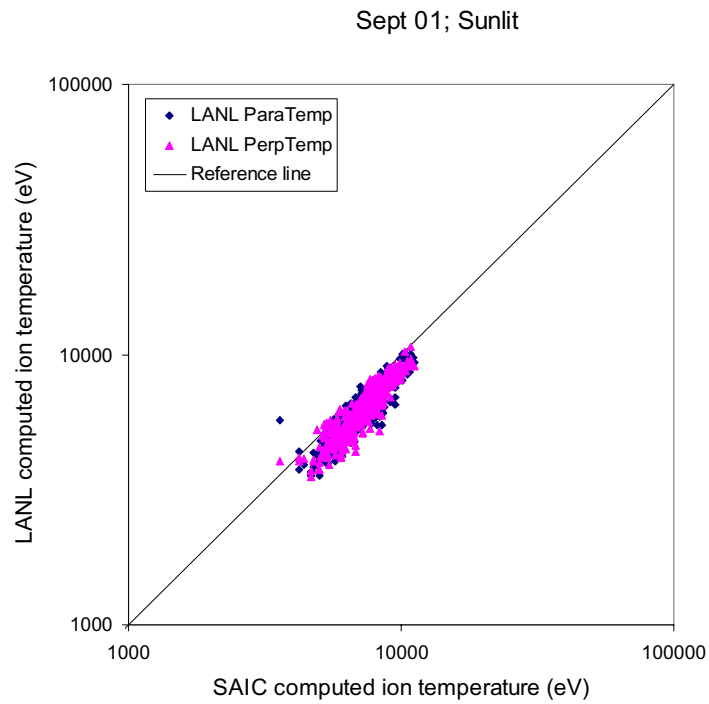


Figure 14. Validity of ion temperature moment calculational technique in sunlight. Integral using full angular spectrum gives lower temperatures than spin-averaged spectrum.

The electron moment results computed at SAIC and LANL are in good agreement. This suggests that the SAIC implementation of the integrals correctly follows LANL's approach. There is a systematic difference in the ion moments. The density integral using the full angular spectrum gives higher densities than the spin-averaged spectrum does. In the temperature moments of Figure 13 and Figure 14, the density used in the SAIC computation is the SAIC computed density. If the LANL density computed using the full angular spectrum is used instead, Figure 15 and Figure 16 result. When computed in this way, the spin-averaged temperatures are close to the parallel temperatures, while the agreement with the perpendicular temperature is only good on average.

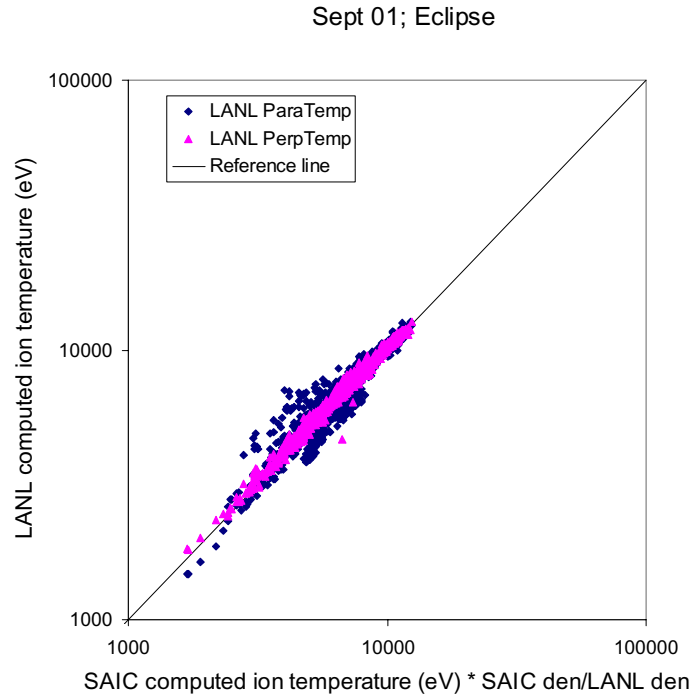


Figure 15. Validity of ion temperature moment calculational technique in eclipse using density from full angular spectrum.

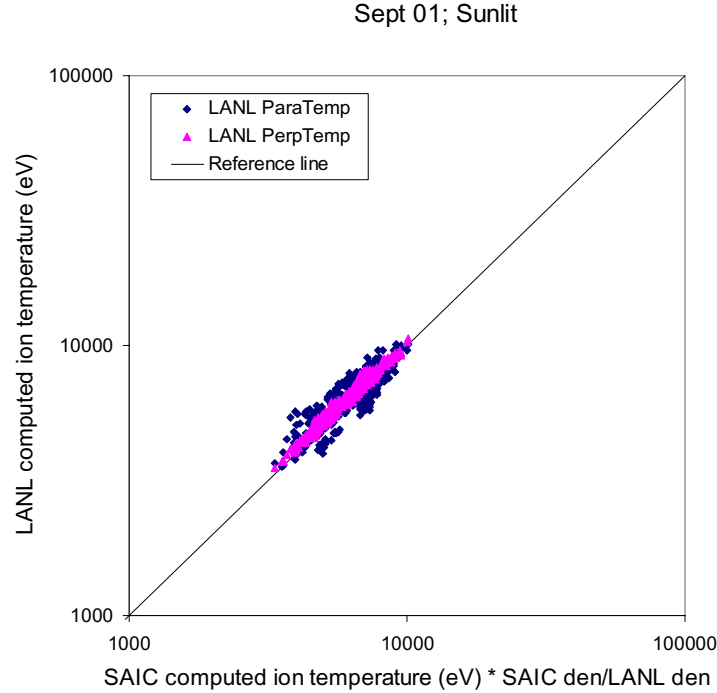


Figure 16. Validity of ion temperature moment calculational technique in sunlight using density from full angular spectrum

The following figures show relationships between the various moments. For both electrons and ions, the temperature varies as the inverse 3/4 power of the density with a great deal of scatter. This dependency was determined by plotting the temperature density relation for electrons in eclipse and selecting the power that matches the lower curve best. For electrons, there are two separate populations that can be present. The higher temperature population is the fresh nightside plasma sheet and the lower temperature population is plasma that has drifted around the earth. Open triangles are used to distinguish the lower temperature population in several of the figures that follow. Points plotted with an open triangle are those that satisfy the relation $\theta n^{0.75} < 300 \text{ eVcm}^{-2.25}$.

The ion and electron densities are correlated and comparable. This is consistent with the fact that we expect the plasma to be neutral on a length scale comparable with the Debye length (hundreds of meters). The ion and electron temperatures are independent. Ion temperatures are generally higher and vary over a smaller range.

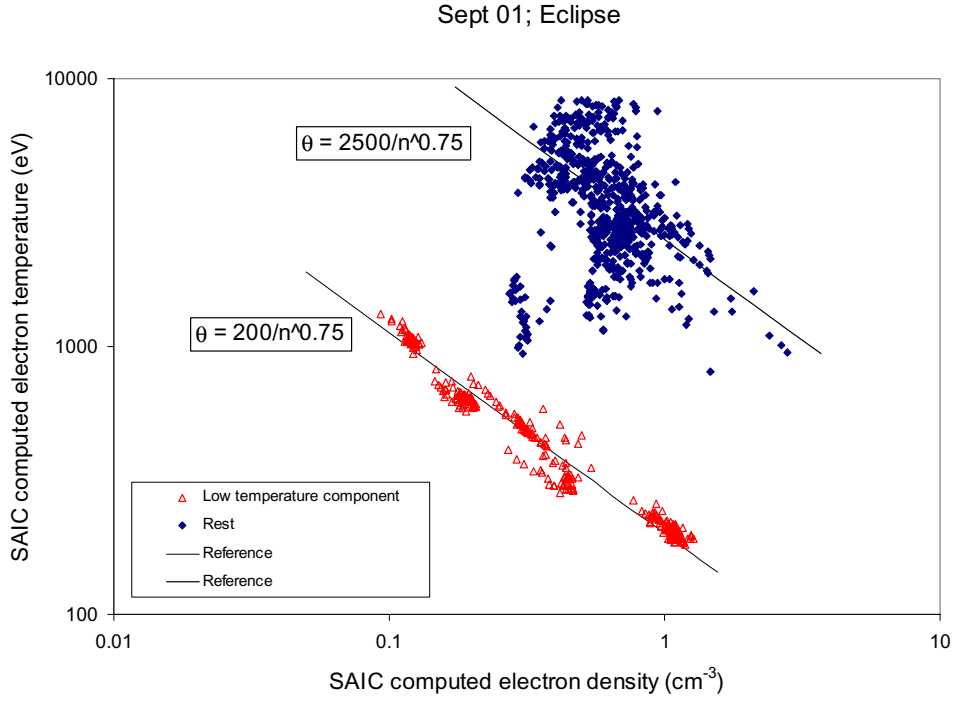


Figure 17. Temperature-density relationship for electrons during eclipse. Points plotted with open triangles have a value of $\theta n^{0.75} < 300 \text{ eVcm}^{-2.25}$.

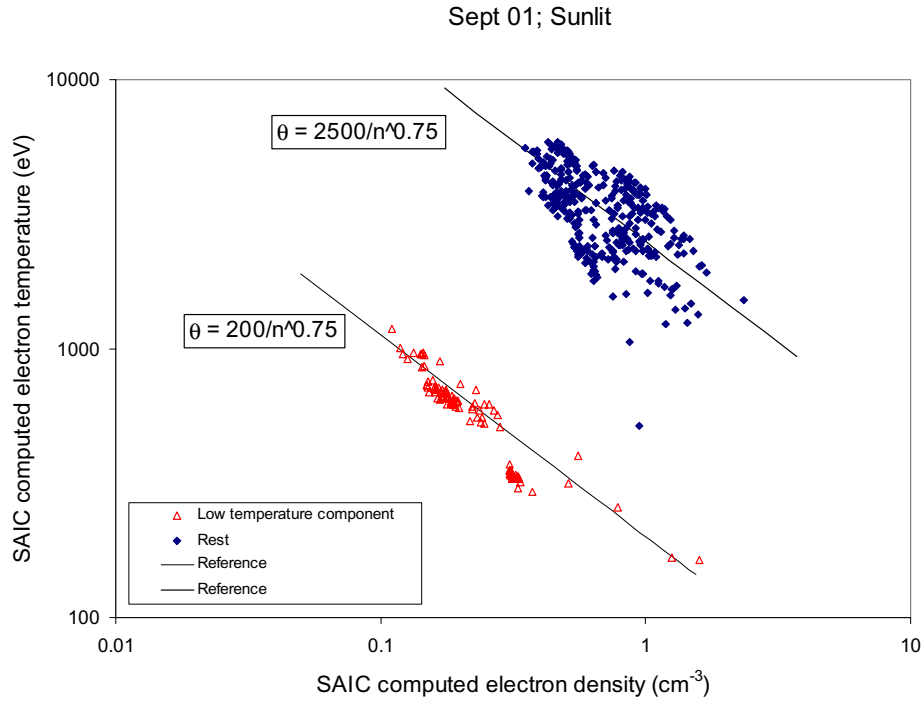


Figure 18. Temperature-density relation for electrons in sunlit data. Points plotted with open triangles have a value of $\theta n^{0.75} < 300 \text{ eVcm}^{-2.25}$.

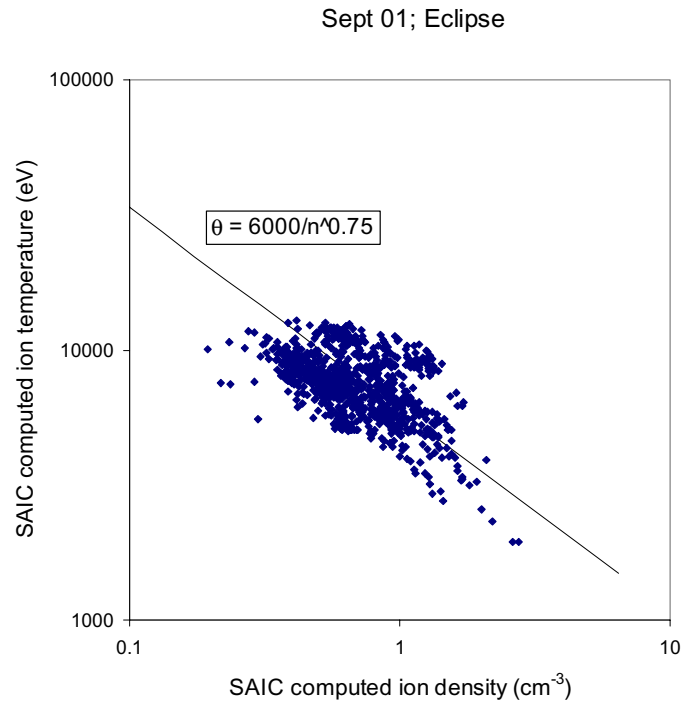


Figure 19. Temperature-density relationship for ions in eclipse.

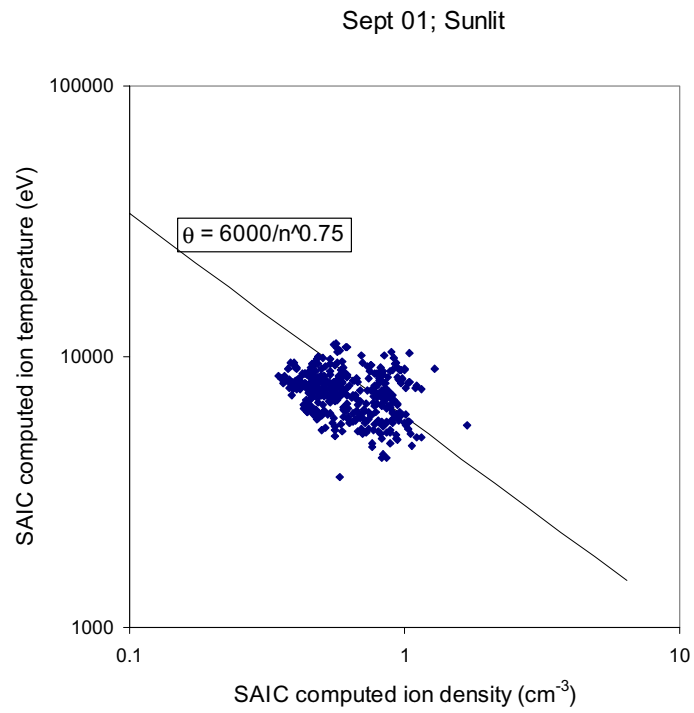


Figure 20. Temperature-density relationship for ions in sunlight.

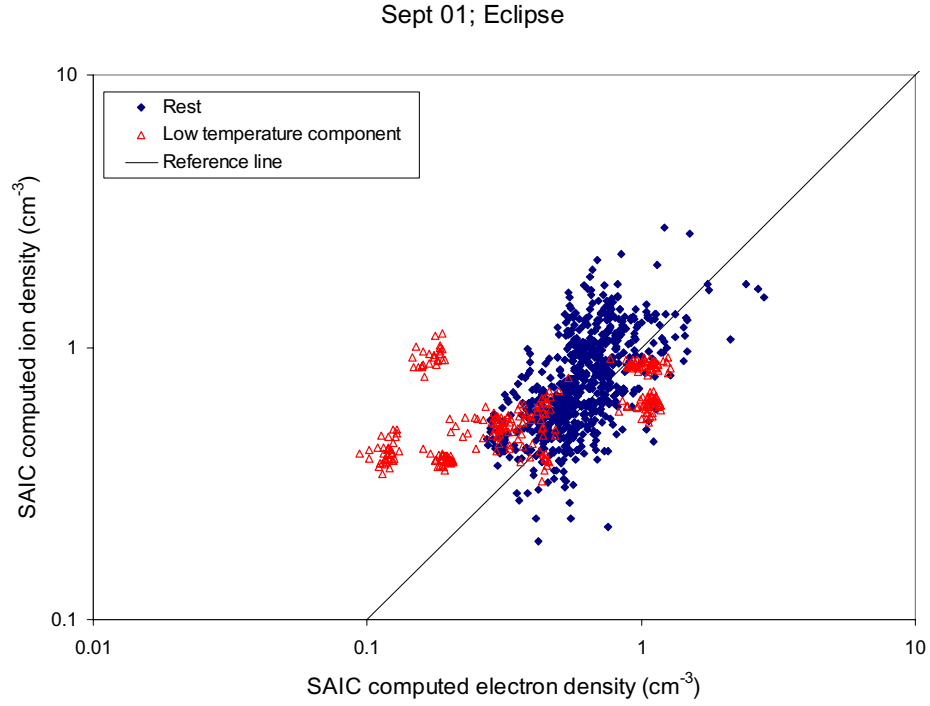


Figure 21. Ion and electron densities are correlated and comparable in eclipse. Points plotted with open triangles have a value of $\theta n^{0.75} < 300 \text{ eVcm}^{-2.25}$ for electrons.

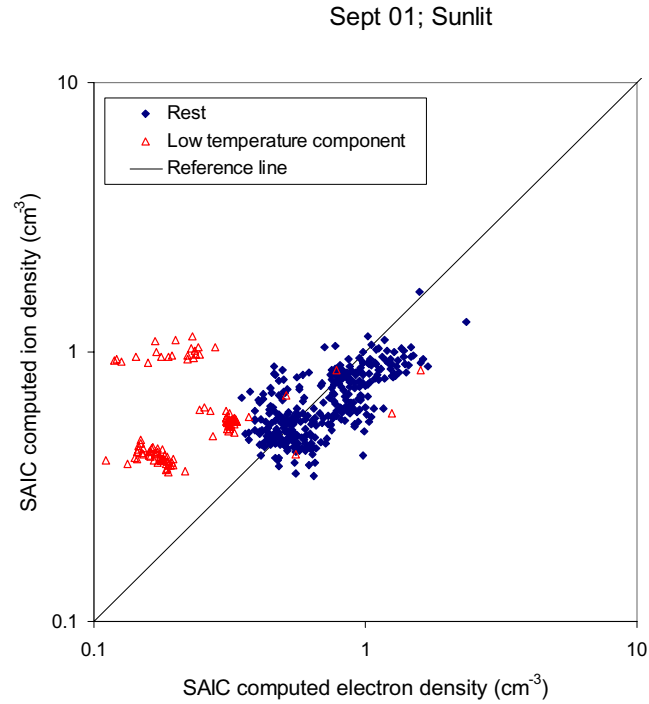


Figure 22. Ion and electron densities are correlated and comparable in sunlight. Points plotted with open triangles have a value of $\theta n^{0.75} < 300 \text{ eVcm}^{-2.25}$ for electrons.

Sept 01; Eclipse

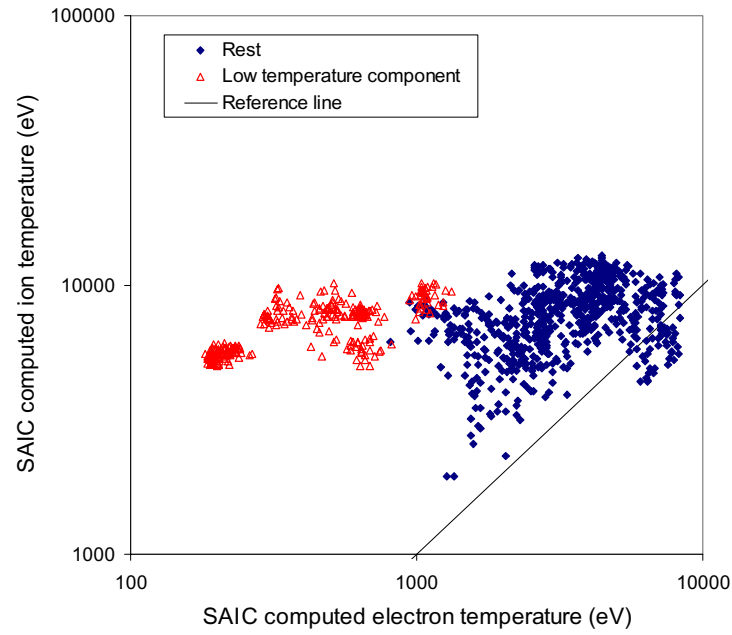


Figure 23. Ion and electron temperatures are independent in eclipse. Ion temperatures are generally higher and vary less. Points plotted with open triangles have a value of $\theta n^{0.75} < 300 \text{ eVcm}^{-2.25}$ for electrons.

Sept 01; Sunlit

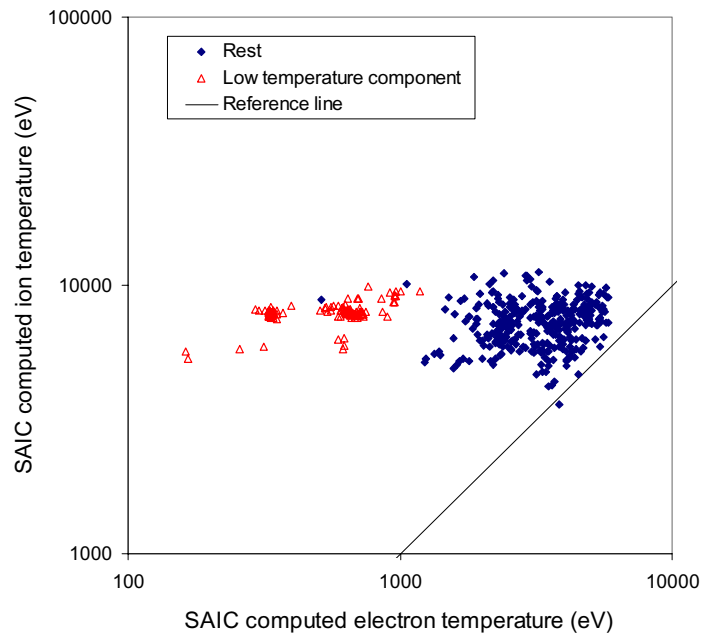


Figure 24. Ion and electron temperatures are independent in sunlight. Ion temperatures are higher and vary less. Points plotted with open triangles have a value of $\theta n^{0.75} < 300 \text{ eVcm}^{-2.25}$ for electrons.

LANL has previously reported that there is a relationship between the electron temperature calculated as described above and the spacecraft chassis potential. Separate power law fits were developed for eclipse and sunlit conditions. For eclipse

$$\phi = 1.74 \times 10^{-5} \theta^{2.26}$$

and for sunlight

$$\phi = 2.4 \times 10^{-7} \theta^{2.51}.$$

The following figures show this relationship for the September 01 and March 01 datasets being used here. The previous fit, shown by the lines in the figures, is consistent with these datasets. The potentials of the low energy electron population points, shown with open triangles, are under 30 eV and independent of the temperature.

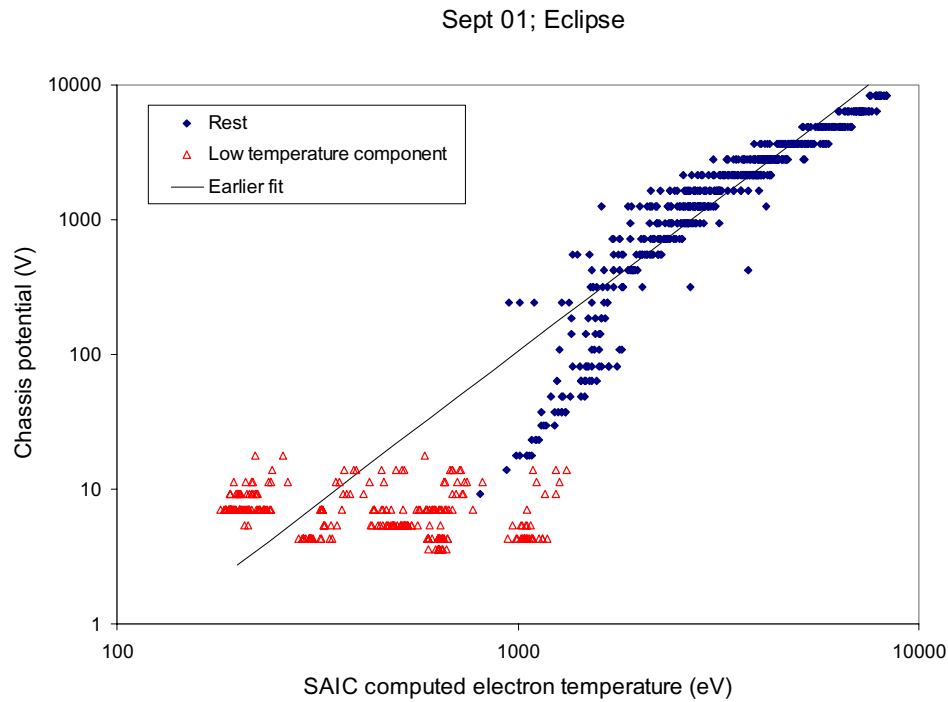


Figure 25. Correlation between chassis potential and electron temperature in eclipse. Points plotted with open triangles have a value of $\theta n^{0.75} < 300 \text{ eVcm}^{-2.25}$ for electrons.

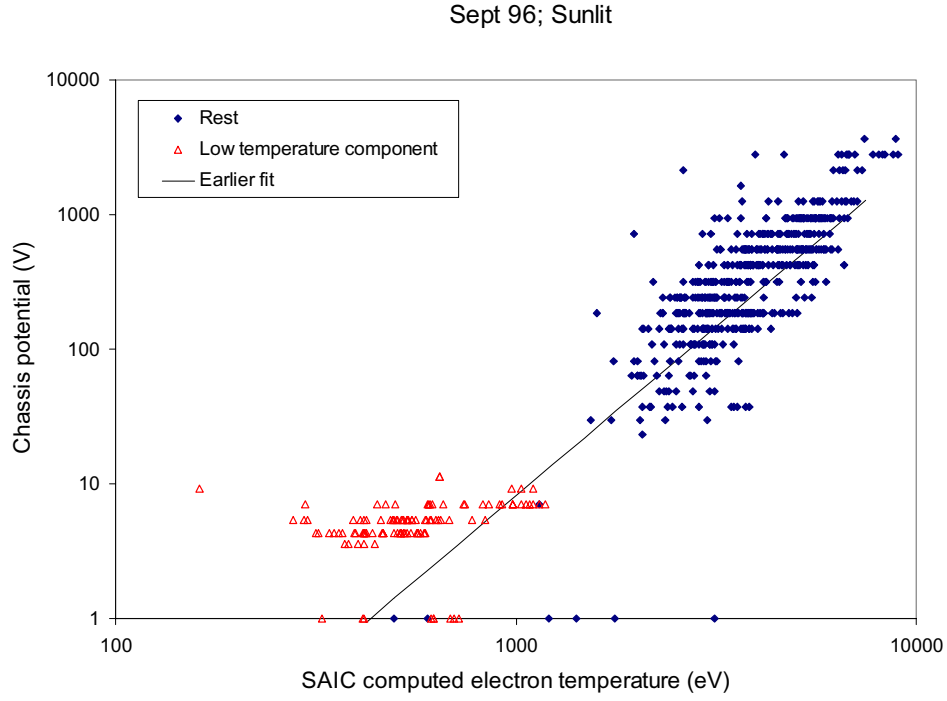


Figure 26. Correlation between chassis potential and electron temperature in sunlight. Points plotted with open triangles have a value of $\theta n^{0.75} < 300 \text{ eVcm}^{-2.25}$ for electrons.

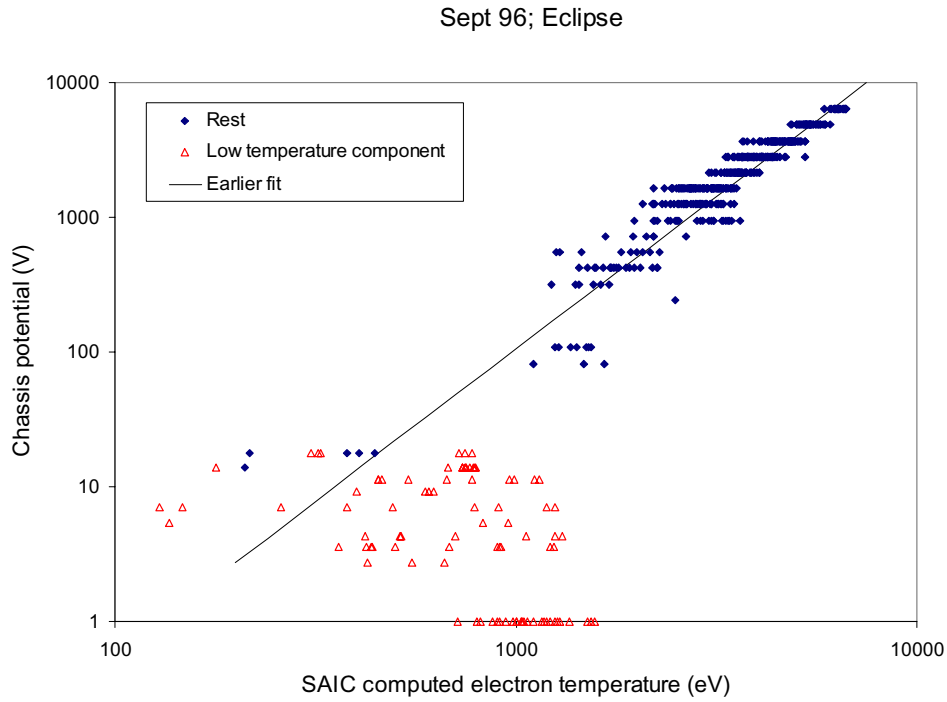


Figure 27. Correlation between chassis potential and electron temperature in eclipse. Points plotted with open triangles have a value of $\theta n^{0.75} < 300 \text{ eVcm}^{-2.25}$ for electrons.

Sept 96; Sunlit

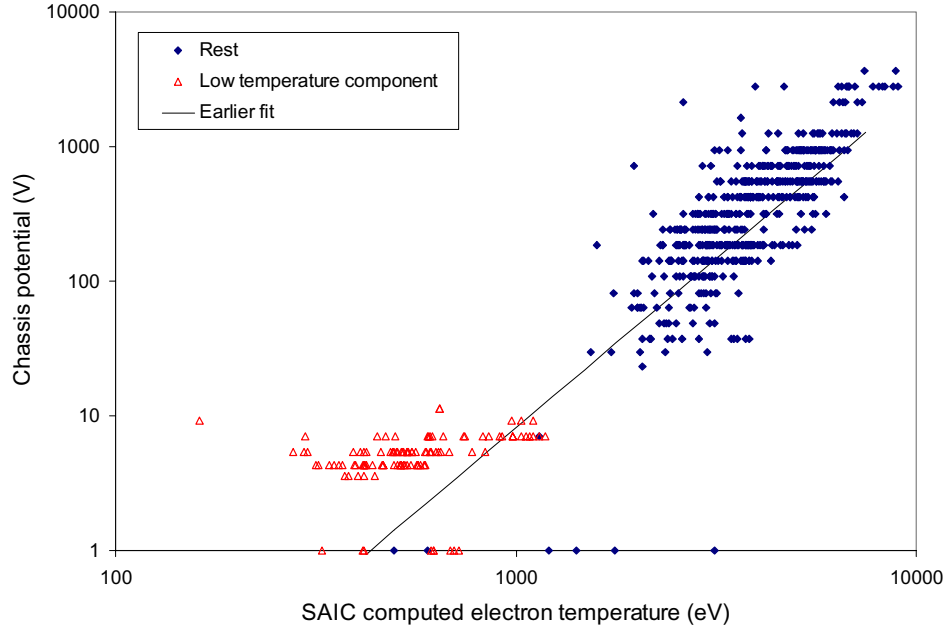


Figure 28. Correlation between chassis potential and electron temperature in sunlight. Points plotted with open triangles have a value of $\theta n^{0.75} < 300 \text{ eVcm}^{-2.25}$ for electrons.

5 Fluxes

Figure 29 and Figure 30 show the net electron flux to the spacecraft and its components, incident electron flux, secondary electron flux, and backscattered electron flux. The net flux is defined as

$$\text{Flux}_{\text{net}}^e = - \int_0^{\infty} F_e(E) [1 - \gamma Y_e(E) - B(E)] dE = \sum_{E > E_{\min}} F_e(E) (-1 + \gamma Y_e(E) + B(E)) \Delta E$$

where the Y s and B are the secondary and backscatter yield functions and γ is the fraction of the low energy electrons that escape from the spacecraft. The secondary and backscatter yield values used are the best available values for carbon graphite and all the low-energy electrons are assumed to escape from the spacecraft ($\gamma=1$).

The flux is plotted along the x-axis and the potential along the y-axis to show how the potential relates to the flux. In order to minimize contamination by secondary and photoelectrons, the minimum potential in the sum is given by the same E_{\min} as used in the calculations of the moments.

At the higher potentials, the incident electron current goes down as the spacecraft potential goes up as a larger fraction of the incident flux is attenuated.

Figure 31 and Figure 32 show the net ion flux to the spacecraft and its components. Different x-axis scales are used for the ion and electron plots. The ion sum is over all energies for which the ion flux exceeds twice the one-count flux.

$$\text{Flux}_{\text{net}}^i = \int_{-\phi}^{\infty} F_i(E) [1 + \gamma Y_i(E)] dE = \sum_E F_i(E) (1 + \gamma Y_i(E)) \Delta E$$

Based on Figure 29 through Figure 32, it would be difficult to make a case that the potential is a function of the incident electron flux, the net electron flux, the incident ion flux, or the net ion flux.

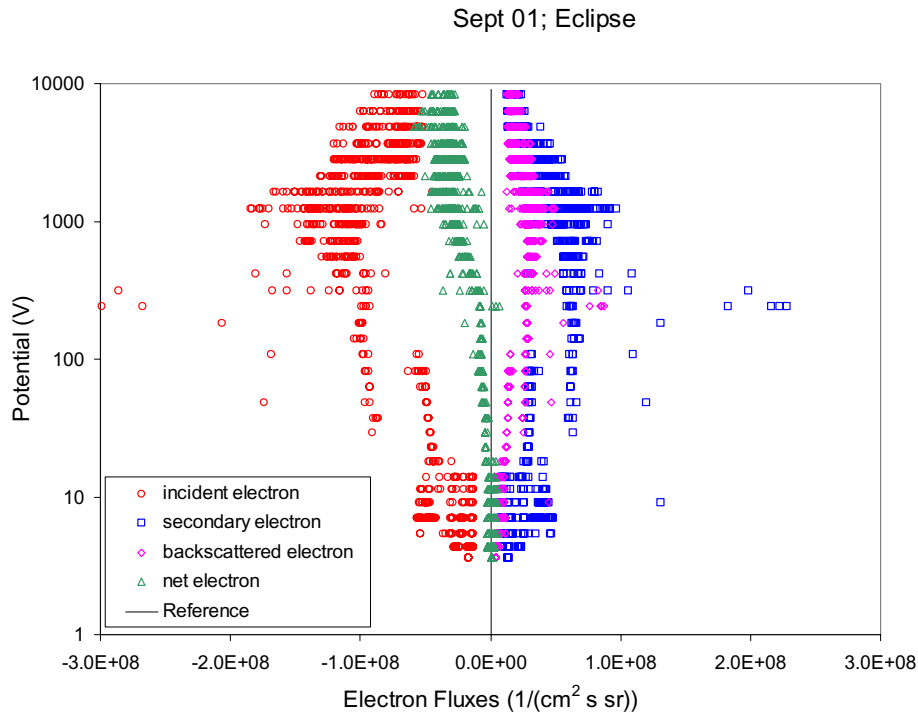


Figure 29. Electron fluxes at all potentials in eclipse.

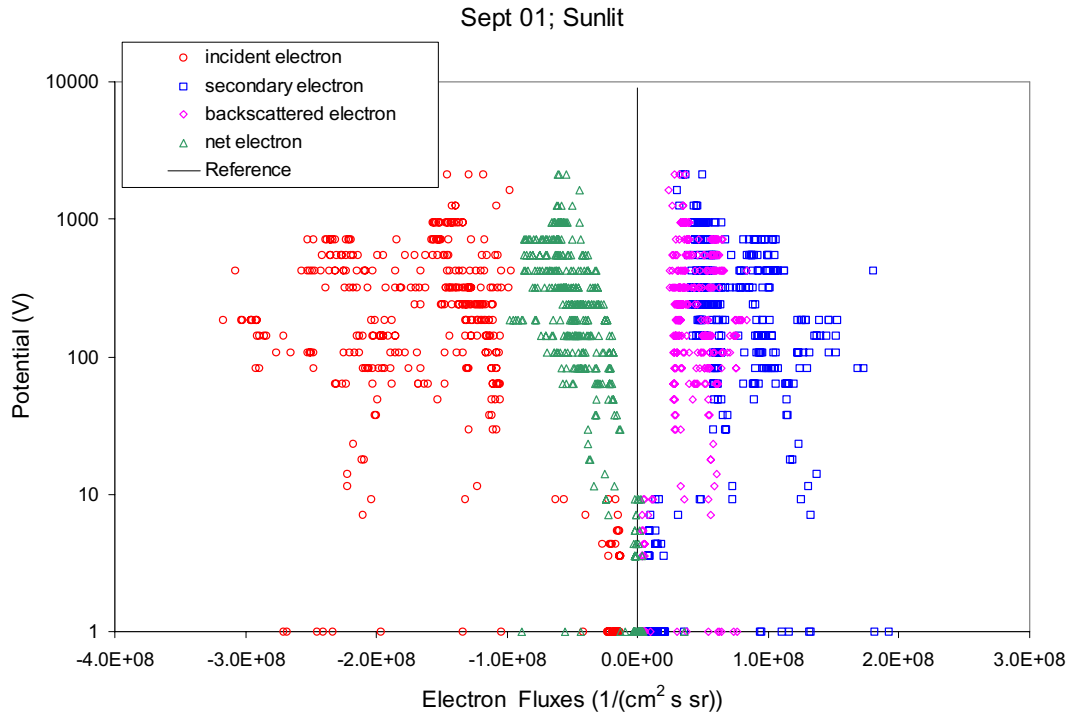


Figure 30. Electron fluxes at all potentials in sunlight.

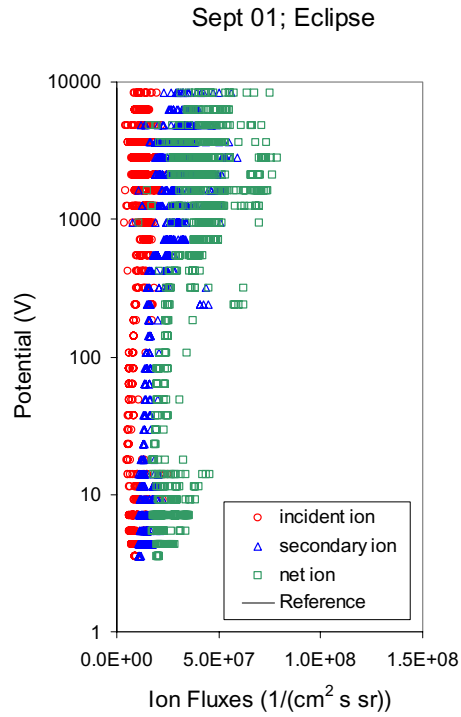


Figure 31. Ion fluxes at all potentials in eclipse.

Sept 01; Sunlit

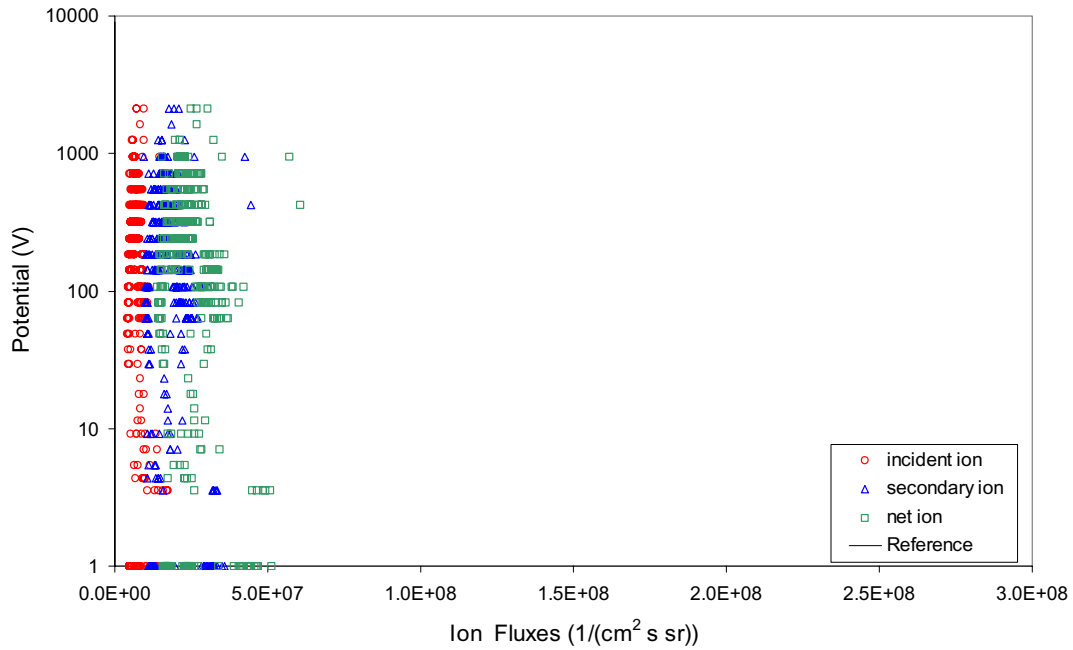


Figure 32. Ion fluxes at all potentials in sunlight.

The net flux to the spacecraft is the sum of the net electron flux and the net ion flux. At equilibrium, the total flux to the spacecraft, which consists of the net flux as defined here plus any photoemission, is zero. If we have a perfect measurement of the spectrum, perfect knowledge of the material properties (secondary and backscatter yields), and there are no geometric effects, the computed net flux in eclipse would be zero at all potentials. Figure 33 shows a small positive net flux with a large amount of scatter for the entire range of potentials. On the average, the net flux is 10% of the incident electron flux and greater than the incident ion flux, so we need to improve the yield functions and the calculational technique.

Figure 34 shows the net flux in sunlight. Ignoring all the other contributions to the error in our computation of the total flux, the net flux shown is equal in magnitude to the photoemission flux. A more energetic environment with higher fluxes charges the spacecraft more. The incident electron flux is not attenuated significantly at the lower potentials seen in sunlight charging. Therefore the photoemitted flux that is able to escape increases with potential.

Figure 35 and Figure 36 show the same results for the September 1996 dataset.

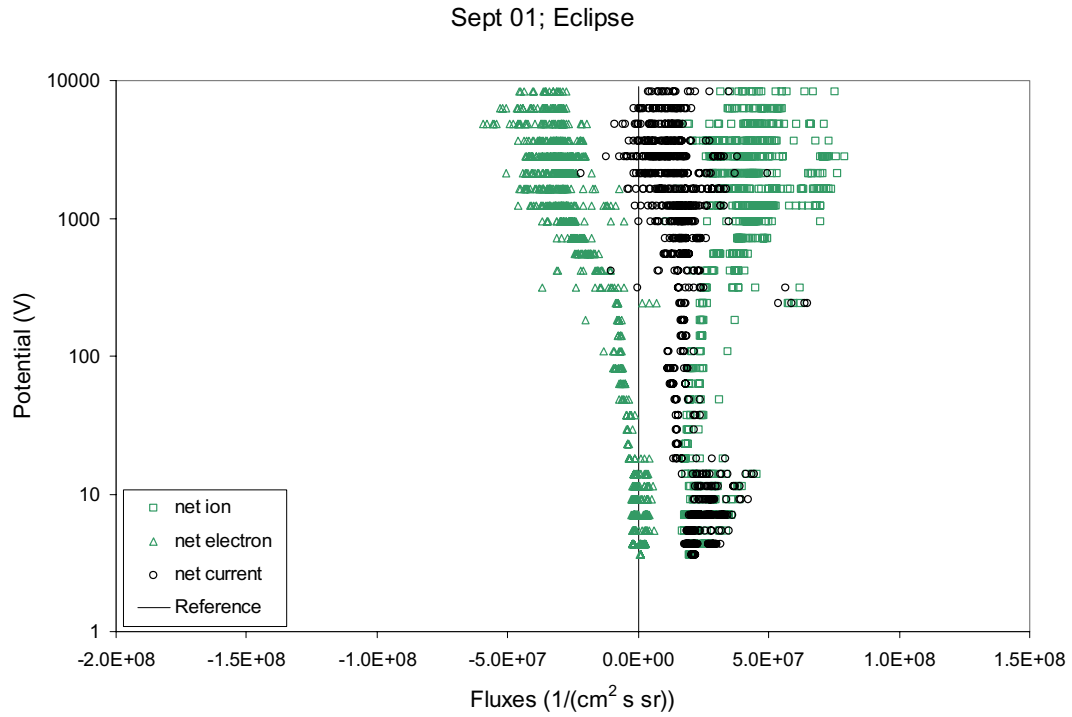


Figure 33. Net flux in eclipse. A complete spectrum, correct yield functions, and proper accounting for suppression of secondaries by barriers would give a value of zero for all potentials.

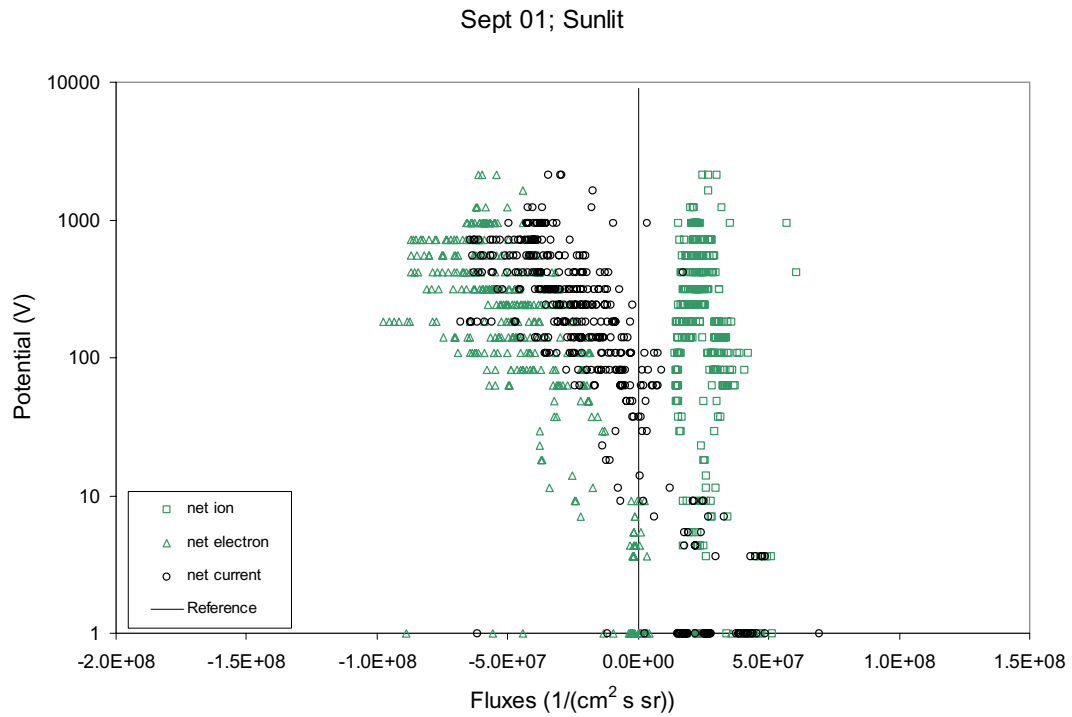


Figure 34. Net flux in sunlight. The net flux, as defined here, does NOT include photoemission. The photoemission needed for current balance is increasing with potential.

Sept 96; Eclipse

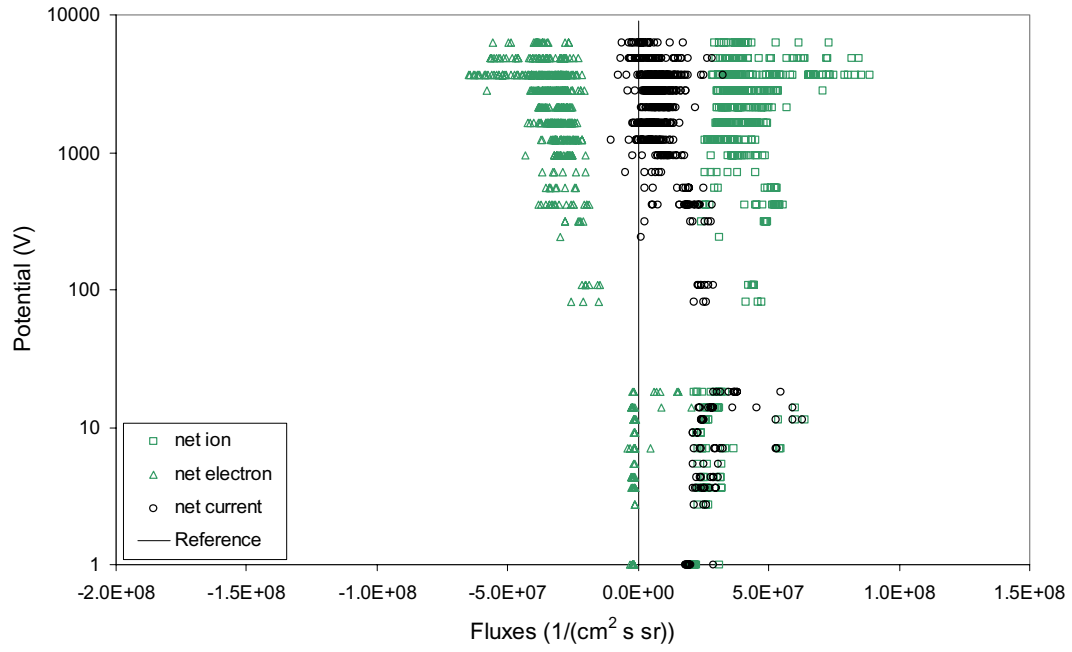


Figure 35. Net flux in eclipse.

Sept 96; Sunlit

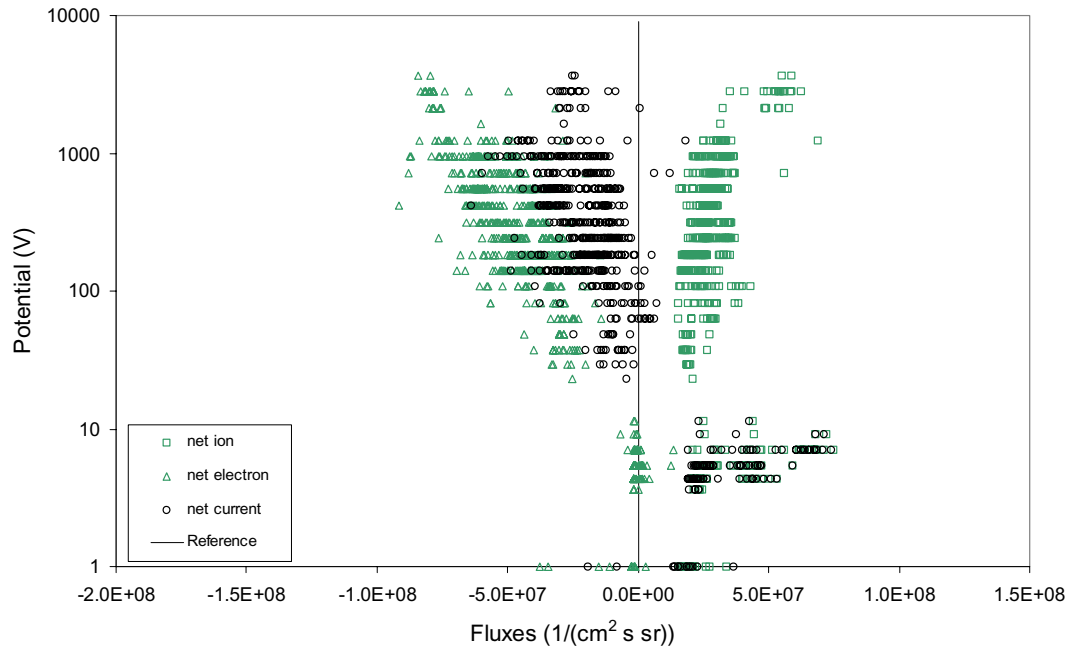


Figure 36. Net flux in sunlit.

6 Chassis Potential Computation

We added to our software the capability to compute the potential that we expect given incident electron and ion spectra. Comparing the measured and computed potentials provides a measure of the quality of the flux computations.

Conceptually, the computation consists of the following three steps:

1. Given the measured potential, compute the ion and electron spectra at infinity.
2. Using the computed ion and electron spectra at infinity, determine the net current (incident, secondaries, backscattered, and photo) to the spacecraft as a function of the spacecraft chassis potential.
3. Search for a unique chassis potential at which the net current is zero. This is the computed chassis potential.

If a computed potential can be found and if the measured and computed potentials are the same within the experimental error bar, we conclude that the flux spectra are adequate to compute the chassis potential.

Three items require addressing:

1. Technique to adjust incident spectra for spacecraft chassis potential. (Required for steps 1 and 2.)
2. Calculation of net current as a function of proposed chassis potential. (Step 2)
3. Technique to search for a unique zero in the net current as function of chassis potential. Alternatives to a unique zero. (Step 3)
4. Size of error bars. (Evaluating results)

The technique used to adjust the spectra to account for the spacecraft potential is addressed in Section 3.2.

6.1 Net Current

The net current to the spacecraft in terms of the proposed potential ϕ' and the measured potential ϕ_m is given by

$$\begin{aligned}
I_{\text{net}} &= -I_e + I_{\text{esc}} + I_{\text{be}} + I_i + I_{\text{isc}} + I_{\text{photo}} \\
F_{\text{net}}(\phi') &= - \int_{\max(0, \phi_m - \phi')}^{\infty} dE_m \left(1 - \frac{\phi_m - \phi'}{E_m} \right) F_e(E_m) [1 - \gamma(\phi') Y_e(E_m - \phi_m + \phi') - B(E_m - \phi_m + \phi')] \\
&\quad + \int_{-\phi_m}^{\infty} dE_m \left(1 + \frac{\phi_m - \phi'}{E_m} \right) F_i(E_m) [1 + \gamma(\phi') Y_i(E_m + \phi_m - \phi')] + \gamma_p(\phi') f_{\text{sunlit}} F_{\text{photo}}(\phi')
\end{aligned}$$

where F_{net} is the signed average net flux to the spacecraft, ϕ_m is the measured potential, ϕ' is the proposed potential, the Y s and B are the secondary and backscatter yield functions, γ is the fraction of the low energy electrons that escape from the spacecraft, f_{sunlit} is the fraction of the spacecraft sunlit (about 1/2), F_e and F_i are the measured fluxes, and F_{photo} is the average photoemitted flux.

The electron integral is only strictly correct if the proposed potential is more negative than the measured potential, $\phi' < \phi_m$. The portion of the electron spectrum that is not measured, as it does not have enough energy to reach the spacecraft at the measured potential, ideally should be included in the integral for the proposed potential. For now, we ignore this discrepancy.

When using measured fluxes, the integral becomes a sum with the value of E_m taken to be the energy at the geometric center of the energy bin. Contributions to the ion integral in which the measured flux is less than twice the one-count flux are ignored. Contributions to the electron integral in which $E_m < E_{\text{min}}$ are discarded as the flux measurement is dominated by secondary and photoelectrons. For both the ion and electron integrals, the lowest energy bin included is the one for which the E_m value exceeds the lower limit of the integral. Half of the time this is an overestimate and half of the time it is an underestimate.

6.2 Zero In Net Current

A zero in the net current as a function of potential is searched for between the limits of -1 and -10000 V. The current-voltage curve is assumed to have a negative slope over the entire range of potential. This is not always true. As a result, the algorithm sometimes fails. There are also cases in which the computed net potential does not have a zero in the range of -1 V to -10000 V. The algorithm also fails for these cases. When the algorithm fails it returns a value of -1 V. At each step, a guess at the potential is made and the net current is computed. A check is made for a net current of nearly zero (absolute value under 10^{-6} A m⁻²) or a change in sign of the net current between successive guesses. When a zero in the curve is found, a linearly interpolated value is returned. The initial guess is the measured potential and each successive guess is the previous guess times or divided by 1.01 depending on the sign of the net current. Presently, the zero is assumed to be unique and the possibility of multiple zeros remains to be explored.

Often the above algorithm fails to provide a solution. We also use another procedure in which we assume that the net current is always positive and look for the potential with the minimum value of net current. This procedure is only applied when the first fails.

6.3 Error Bars

The measured potential has a sizeable error bar, which also leads to error bars in the net current calculations that depend on the measured potential.

Throughout most of the energy range of the MPA instrument, the energy of the upper edge of the energy bin is approximately 1.31 times the energy of the lower edge. Neighboring energy bins can also respond to an incident particle. The measured potential is the geometric center of the lowest energy bin with a significant number of counts. (The actual algorithm is much more complex than this, but for present purposes this simplification is adequate.) Therefore, the actual potential is only measured within a factor of 1.15. $\phi_m/1.15 < \phi_{\text{actual}} < 1.15\phi_m$. Additional errors are introduced in the computation of the net current using the measured potential, rather than the actual potential. And finally, we are treating the spacecraft as a uniform sphere, introducing significant errors. Somewhat arbitrarily, we take agreement within a factor of 1.5 to be good agreement.

6.4 Results

Figure 37 and Figure 38 compare the measured and computed potential for the September 2001 eclipse dataset. In Figure 37, we look for a zero in the net flux. Loosening the criteria to search for a minimum in the flux rather than a zero, increases the number of cases in which a solution can be found as most of the solutions are good solutions. The poor potential estimate shown in these figures tells us that we need to improve our technique of computing the net current.

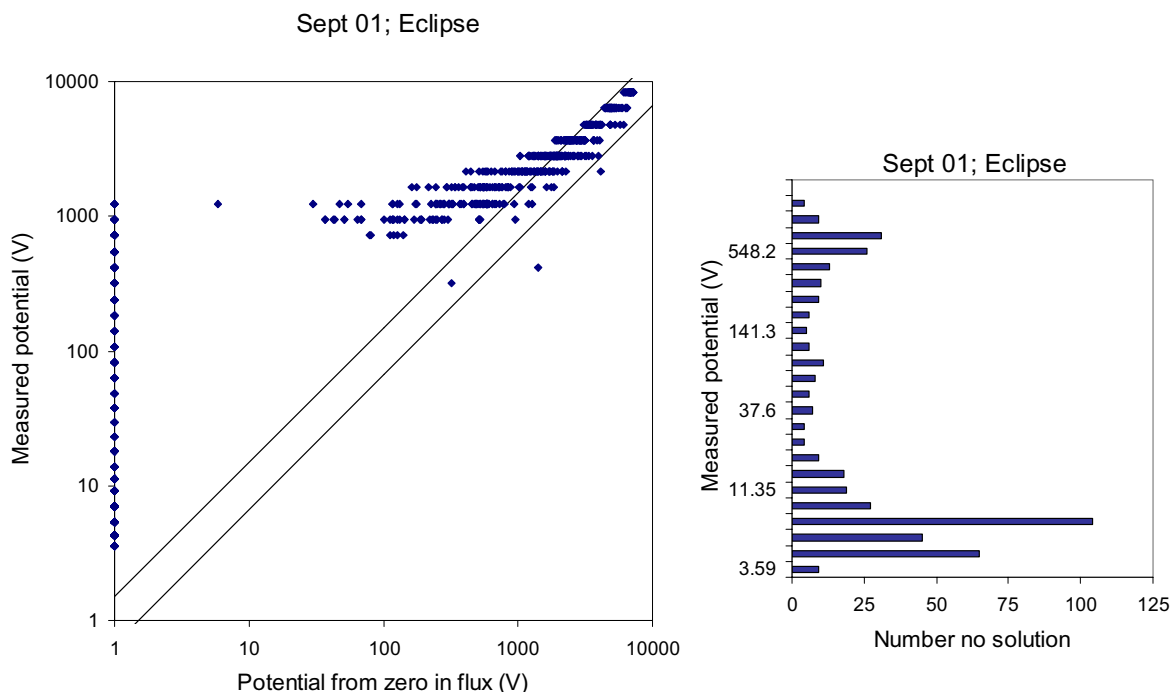


Figure 37. For Sept 01 eclipse data, measured potential as a function of the potential computed from the zero in the net flux. The lines are $y = 1.5x$ and $y = x/1.5$. The bar chart at the right shows the number of spectra for which no solution was found for each value of measured potential. These points are represented in the plot on the left by a single diamond along the left hand axis.

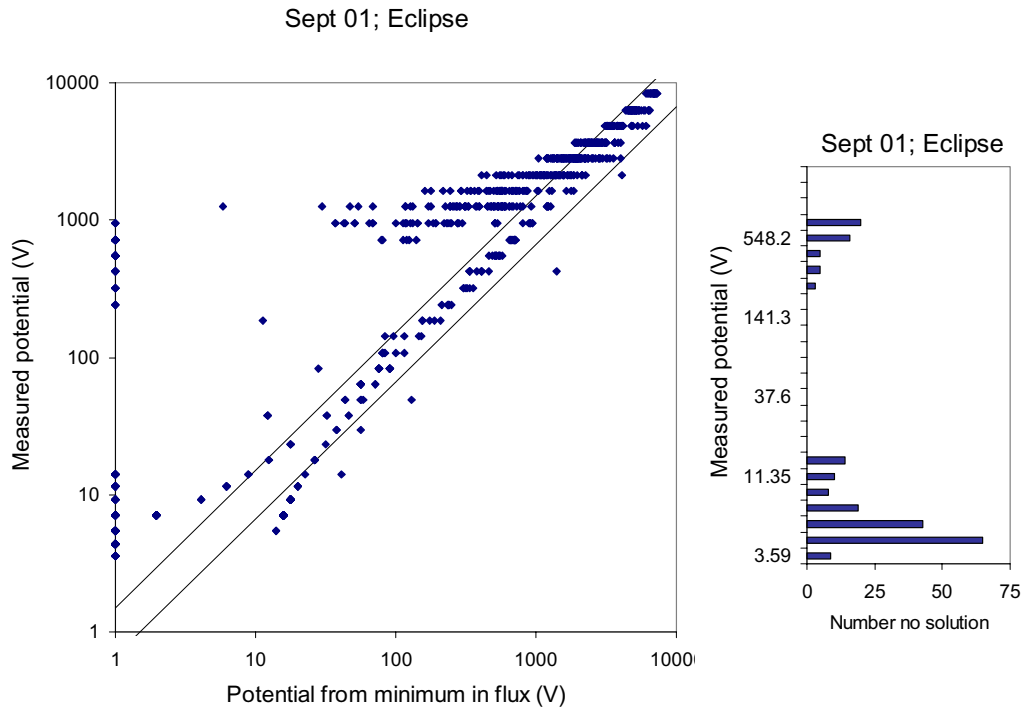


Figure 38. For Sept 01, eclipse data, measured potential as a function of the potential computed from the minimum in the net flux. The lines are $y = 1.5x$ and $y = x/1.5$. The bar chart at the right shows the number of spectra for which no solution was found for each value of measured potential.

7 Calculational Techniques

7.1 Yield Functions

The computations of fluxes shown above require knowledge of the average yield properties of the spacecraft surfaces. We are treating the spacecraft as if it was covered entirely by a single average material. The properties we choose to use for the first set of calculations described here are for graphite and are shown in Table 1. The electron-generated secondary yield properties are chosen to fit the curve in Barnett, et al. [1977], which tabulates data from Holzland and Jacobi, [1969] and Bruining [1938]. The ion-generated secondary yield properties are chosen to be consistent with the curve for incident Hydrogen ions in Barnett, et al. [1977], which tabulates data from Large and Whitlock, [1962]. The effective atomic number, which is used to compute the backscatter, is the default value for graphite in the SEE Spacecraft Charging Handbook. Figures 39-42 show the yield properties of this material, labeled “Carbon,” and a selection of materials from the default materials supplied with the SEE Spacecraft Charging Handbook. We also reviewed preliminary results from measurements of yield properties made at Utah State. The yield curves derived from the default properties of the Gold, Kapton, OSR, and Solar Cell materials included in the SEE Spacecraft Charging Handbook are representative of the range of spacecraft materials. Flux and potential calculations using the properties of these four materials are shown in Figures 43-50. All of the other sets of material properties give much larger positive net current than “Carbon” does in the hundreds through thousands of volts range of spacecraft

potential. The estimated potentials using the OSR and Solar cell material properties are consistently higher than the measured potentials. Using Gold material properties tends to overestimate the potential, and using Kapton material properties sometimes overestimates it and sometimes underestimates it. The low secondary yield peak at low incident electron energy represents the actual average spacecraft material the best. The rest of the calculations shown in this report all use the properties shown in Table 1.

Table 1. Material properties used average material “Carbon”

Property	Value
Backscatter	
Effective atomic no.	4.5
Secondary electron yield due to incident electrons	
Max sec. yield	0.93
Energy of peak	0.28 keV
Range Param 1	180
Range Exp. 1	0.45
Range Param 2	312
Range Exp. 2	1.75
Secondary electron yield due to incident ions	
Sec. Yield of 1 keV proton	0.455
Proton energy	80 keV

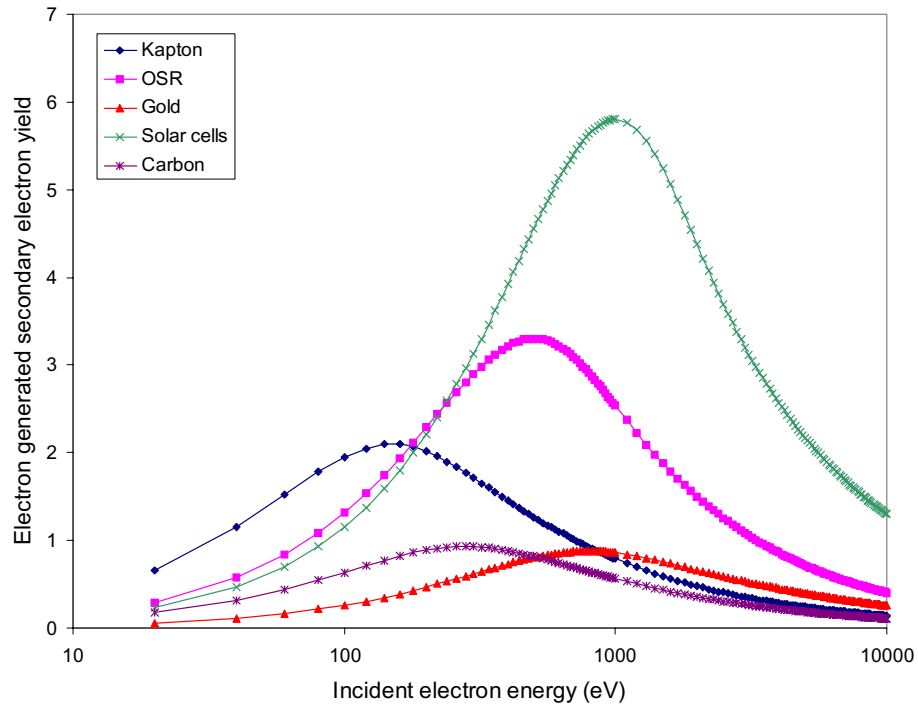


Figure 39 Secondary electron yield from incident electron impact for materials defined in the SEE Spacecraft Charging Handbook and the Carbon material used here.

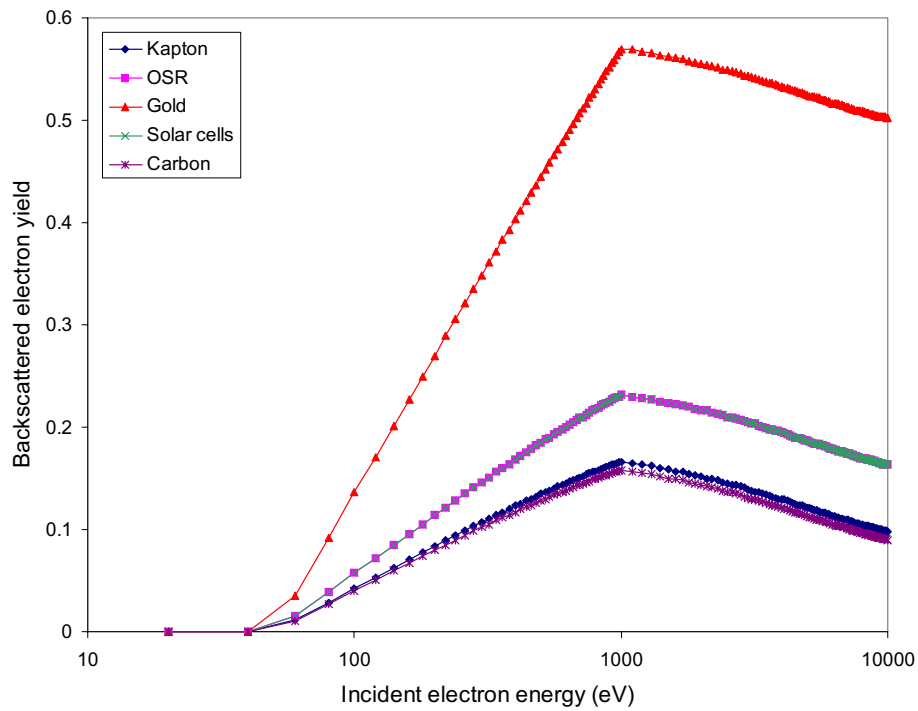


Figure 40. Backscattered electron yield from incident electron impact for materials defined in the SEE Spacecraft Charging Handbook and the Carbon material used here.

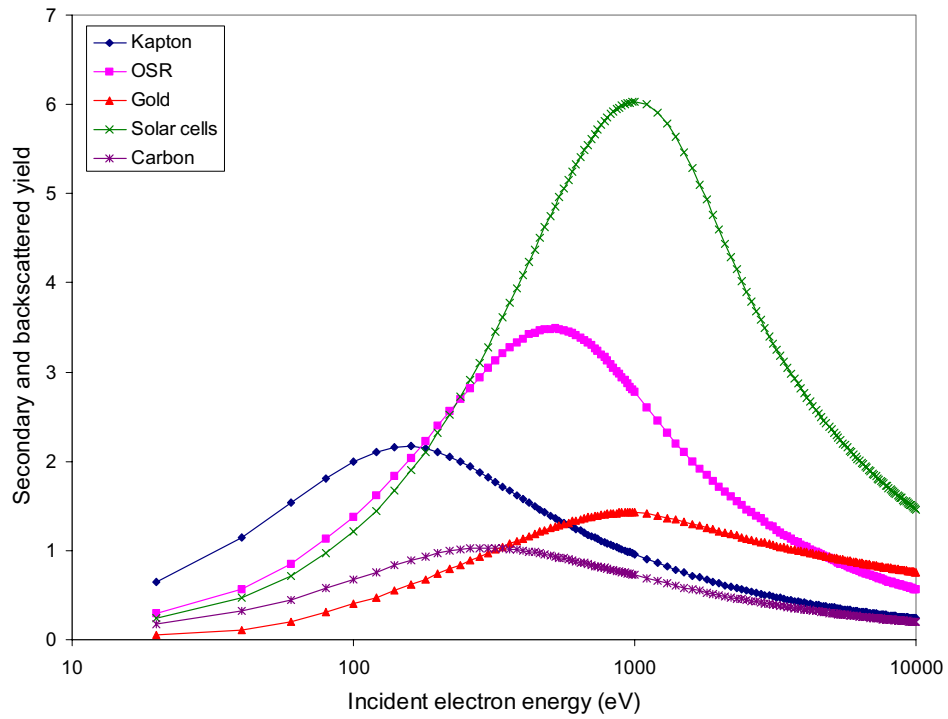


Figure 41 Sum of secondary and backscattered electron yields from incident electron impact for materials defined in the SEE Spacecraft Charging Handbook and the Carbon material used here.

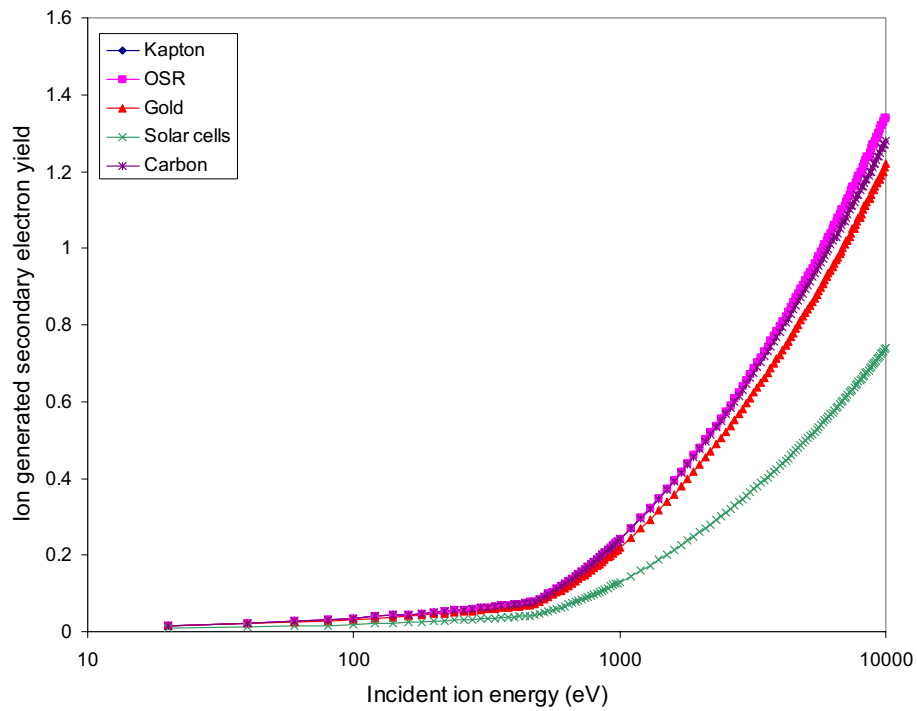


Figure 42 Secondary electron yields from incident ion impact for materials defined in the SEE Spacecraft Charging Handbook and the Carbon material used here.

Sept 01; Eclipse; Gold spacecraft

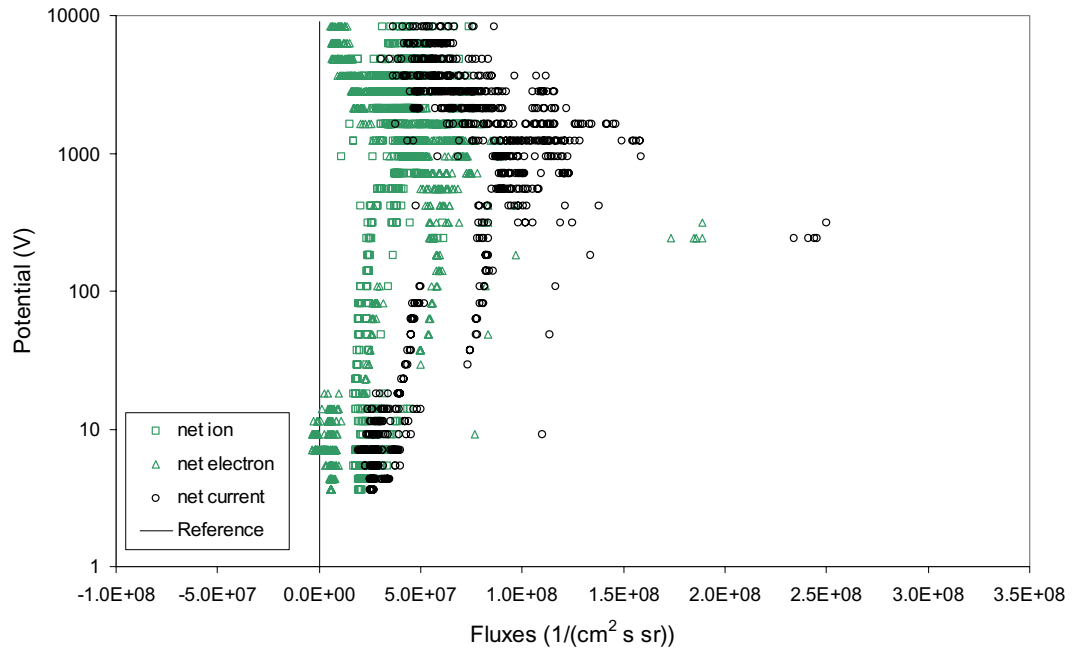


Figure 43. Net flux in eclipse using material properties of Gold as defined in the SEE Spacecraft Charging Handbook.

Sept 01; Eclipse; Gold spacecraft

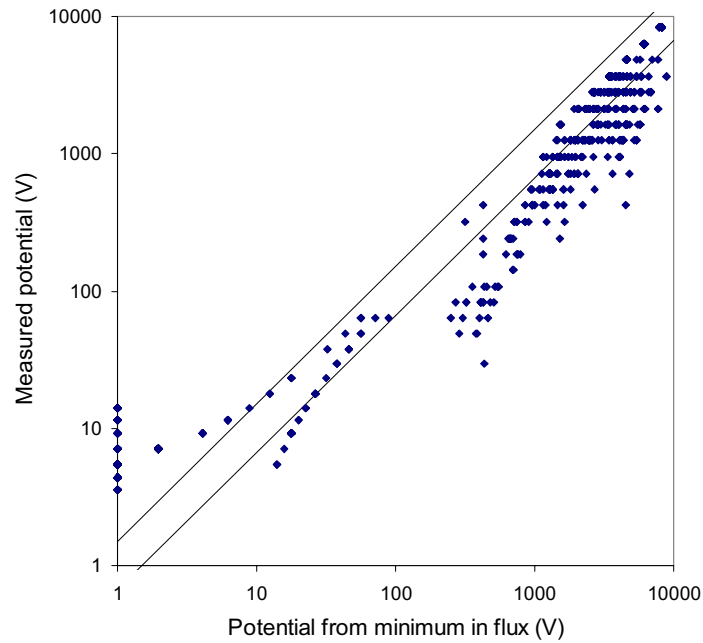


Figure 44. For Sept 01, eclipse data, measured potential as a function of the potential computed from the minimum in the net flux using material properties of Gold as defined in the SEE Spacecraft Charging Handbook.

Sept 01; Eclipse; Kapton spacecraft

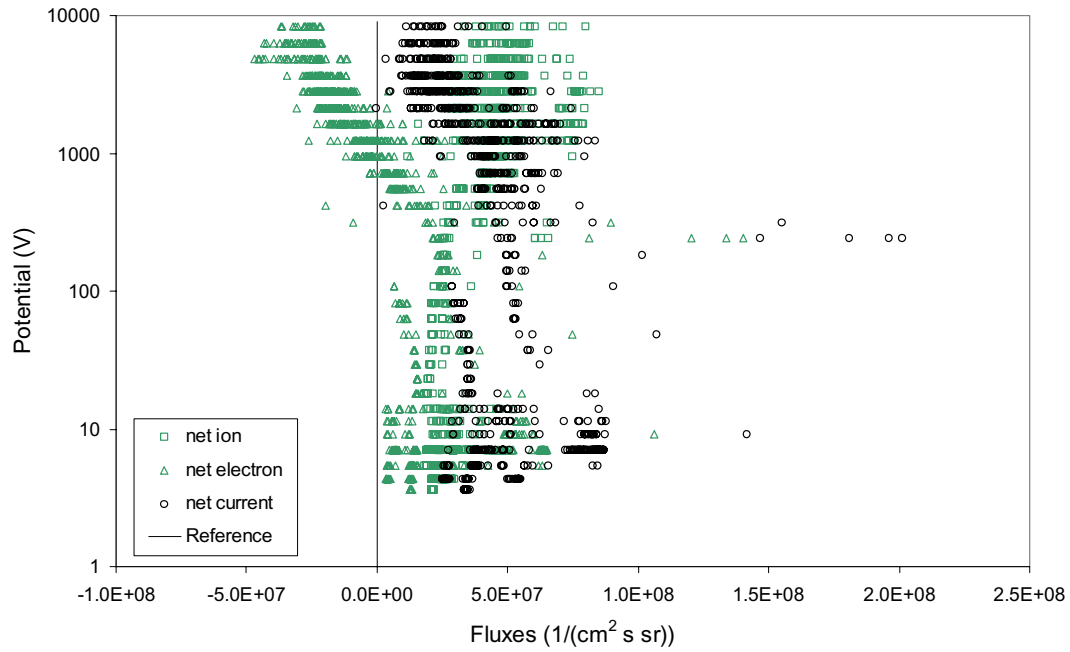


Figure 45. Net flux in eclipse using material properties of Kapton as defined in the SEE Spacecraft Charging Handbook.

Sept 01; Eclipse; Kapton spacecraft

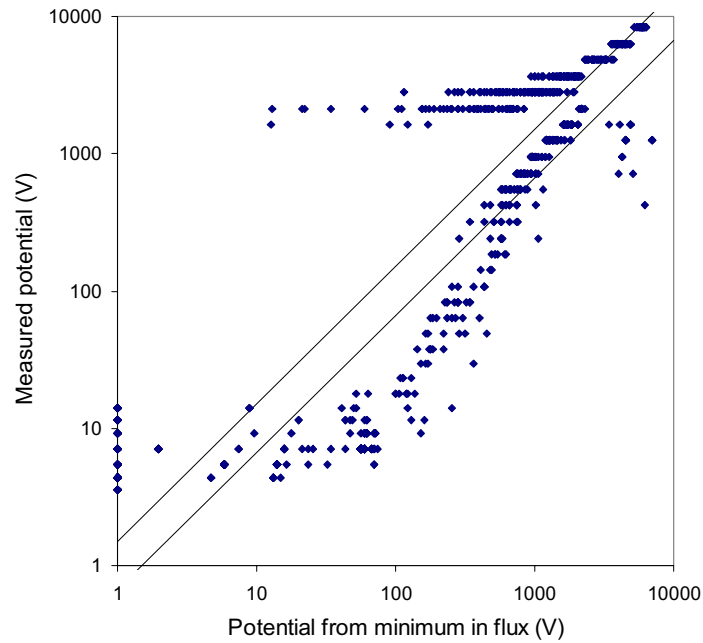


Figure 46. For Sept 01, eclipse data, measured potential as a function of the potential computed from the minimum in the net flux using material properties of Kapton as defined in the SEE Spacecraft Charging Handbook.

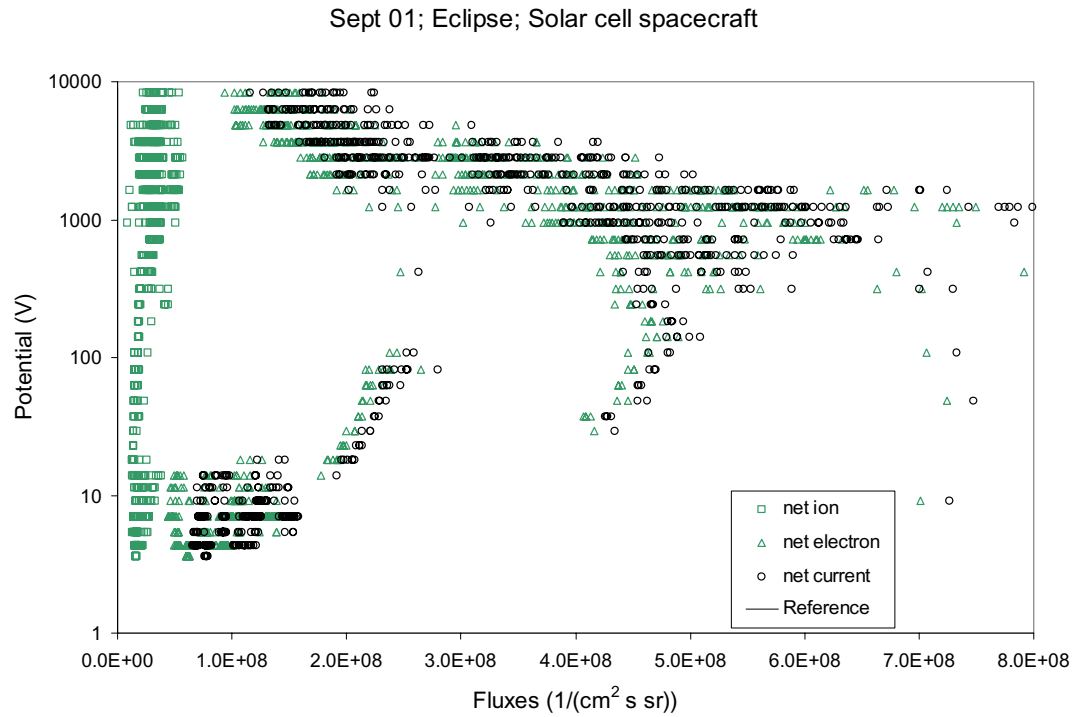


Figure 47. Net flux in eclipse using material properties of Solar cell coverglass material as defined in the SEE Spacecraft Charging Handbook.

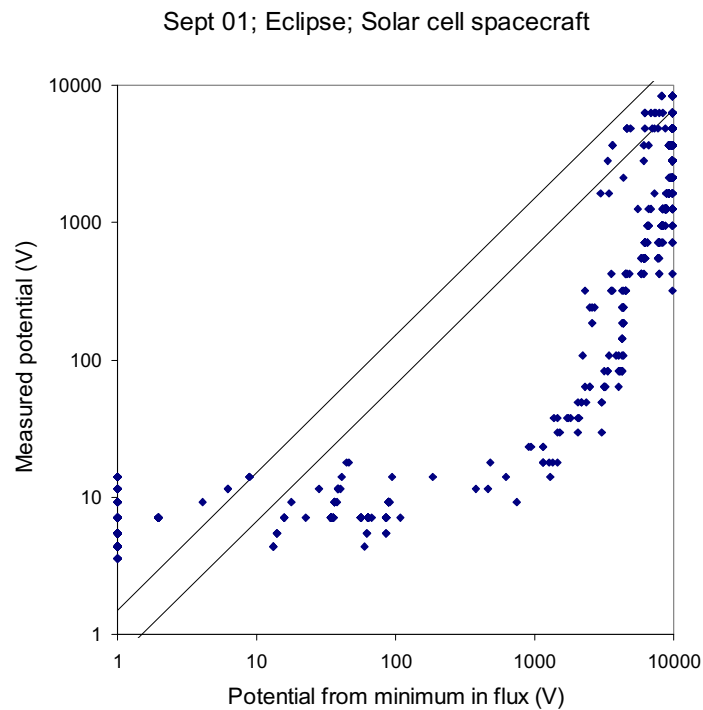


Figure 48. For Sept 01, eclipse data, measured potential as a function of the potential computed from the minimum in the net flux using material properties of Solar cell coverglass material as defined in the SEE Spacecraft Charging Handbook

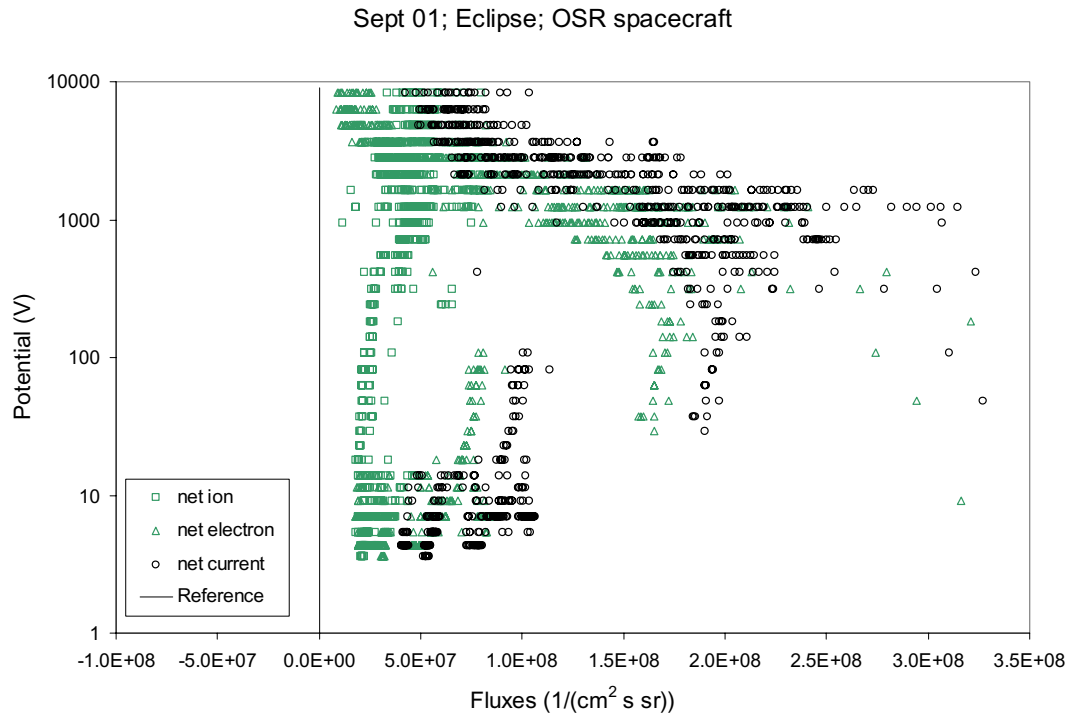


Figure 49. Net flux in eclipse using material properties of OSR as defined in the SEE Spacecraft Charging Handbook.

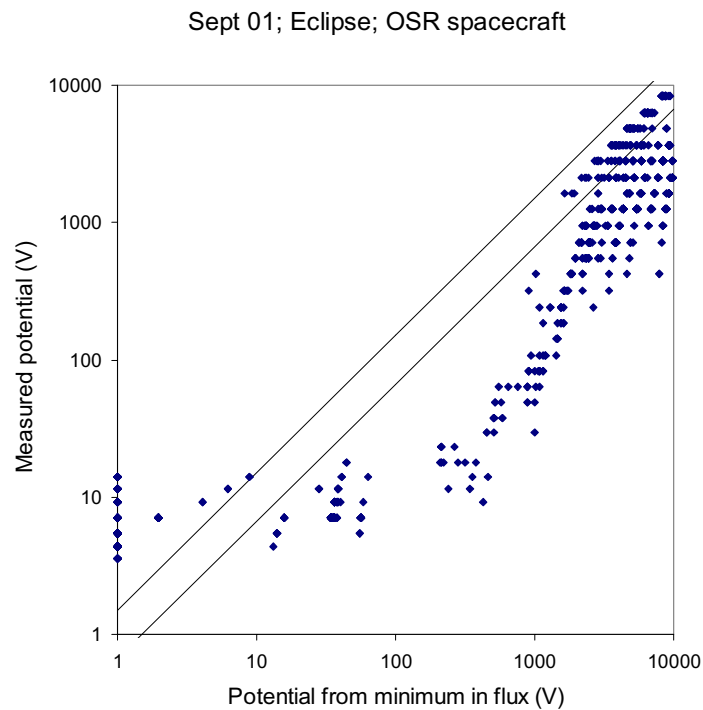


Figure 50. For Sept 01, eclipse data, measured potential as a function of the potential computed from the minimum in the net flux using material properties of OSR as defined in the SEE Spacecraft Charging Handbook.

7.2 High Energy Extrapolation

The MPA measurements only extend up to 47 keV for electrons and 49 keV for ions. We were interested in exploring the possibility that we might be able to obtain better results by extending the integral beyond the measurements. We do this by fitting the last five points of the spectrum to a Kappa distribution function. We then add additional points to the sum up to an energy of $10^5 \text{ eV} \pm \phi$, where the “+” is for the electron spectrum and “-” for the ion spectrum. Each point is for an energy of 1.31 times the previous point. No checking for quality of fit is done. Figure 51 and Figure 52 show the resulting fluxes. This approach does not appear to be useful and has not been pursued further.

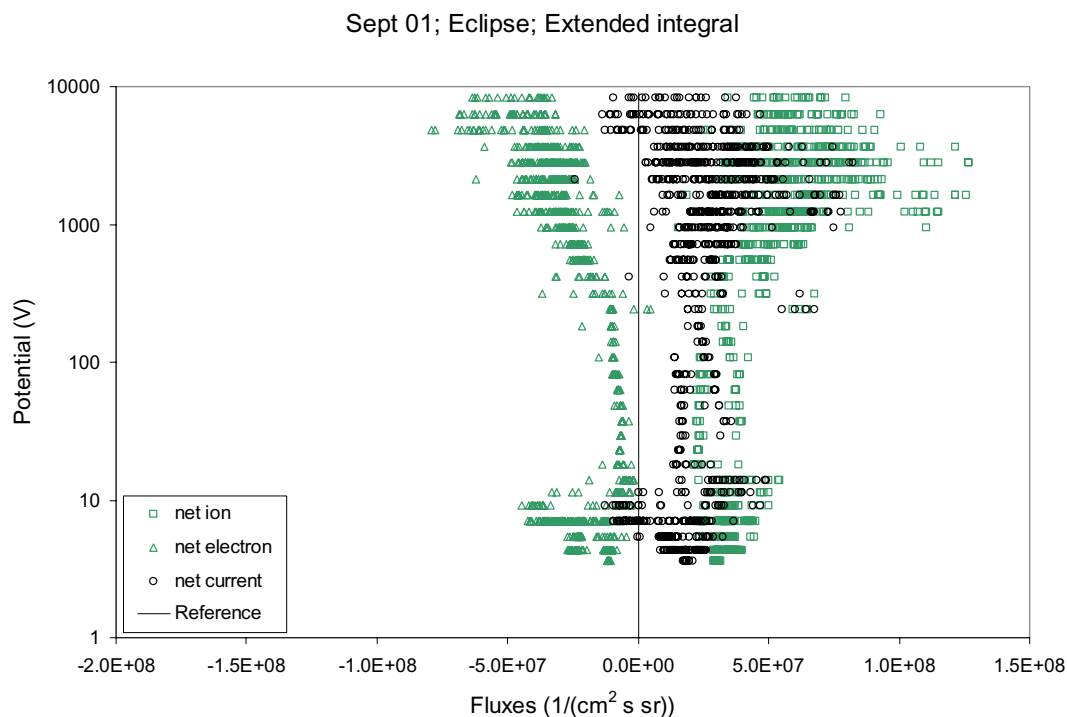


Figure 51. Net flux in eclipse including contribution from extrapolated fluxes.

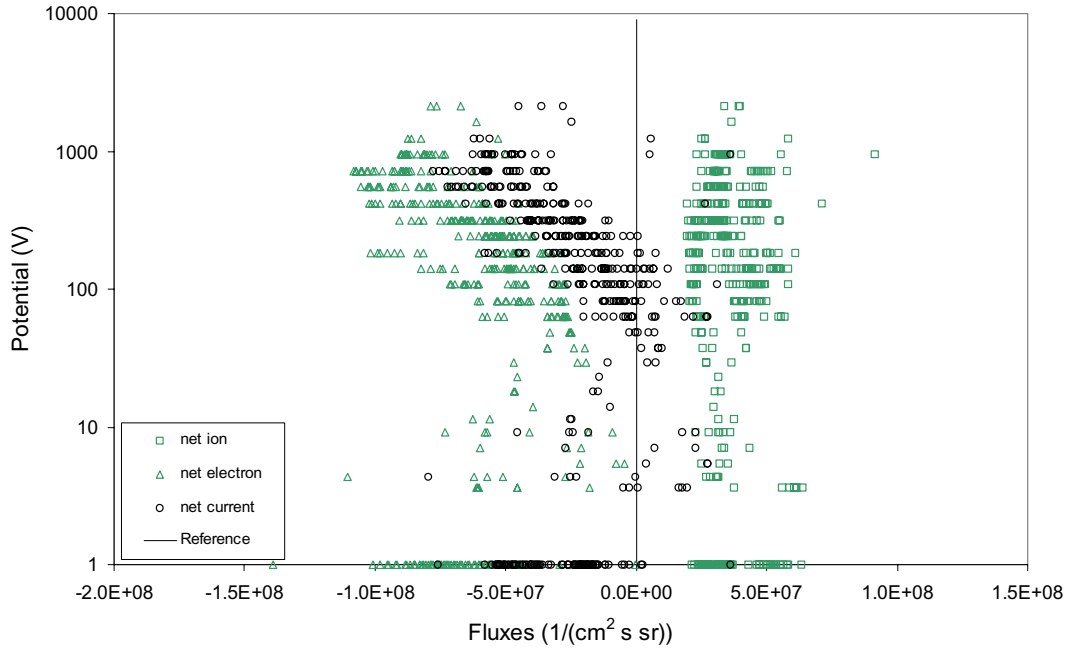


Figure 52. Net flux in sunlight, including contribution from extrapolated fluxes.

7.3 Low Energy Electron Cutoff

Another aspect of the integral that was explored is the lower energy cutoff in the electron spectrum. When the spacecraft is charged, the low energy part of the electron spectrum is usually dominated by low energy secondary and photo electrons trapped by differential potentials near the detector. The lower limit of the electron integrals needs to be as low as possible while high enough to eliminate the trapped electrons. LANL computes this energy by searching for the minimum in the count rate in the energy bins between 30 eV and 400 eV. [Thomsen, *et al*, 1999] The energy at the center of this bin is reported as the barrier. Figure 53 shows this barrier as a function of potential for the September 2001 dataset sunlit points. For eclipse points, the “LANL barrier” is always 34.18 eV. For points with a barrier of 34.18, we propose an alternative barrier of half the potential. These points are shown as triangles in Figure 53. Figure 54 shows the fluxes in eclipse using the alternative barrier rather than the LANL barrier. The only significant differences are in the low potential points. When the potential is computed, Figure 55, many of the low potential points falls on within the 1.5 range of a perfect fit. Figure 56 shows the sunlit fluxes. We also tried some other approaches to determining the appropriate value to use for the cutoff. Nothing we tried works better than these two values. The rest of the calculations in this report use the alternative barrier.

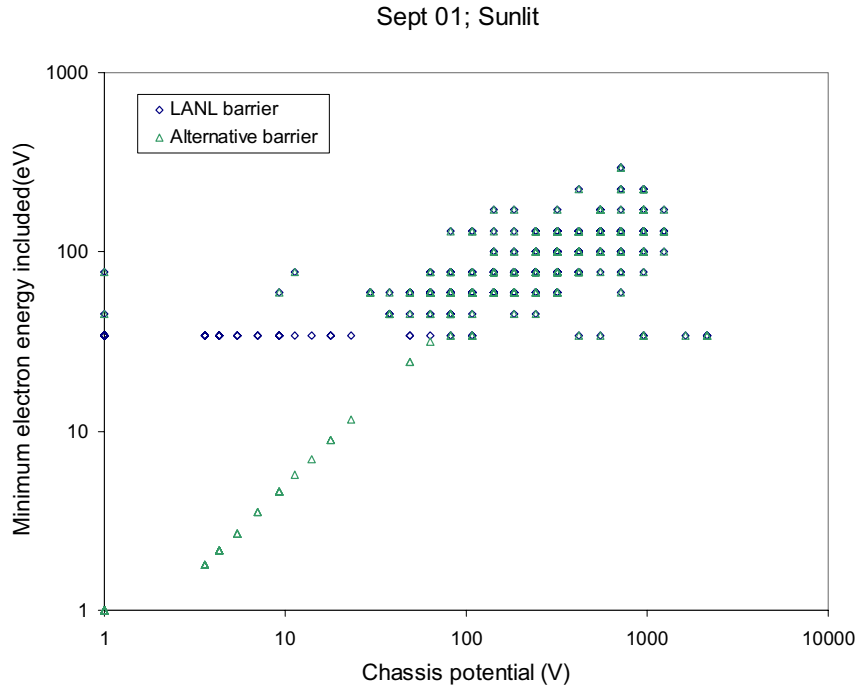


Figure 53. Minimum energy used in the calculations up to this point (LANL barrier) and an alternative as a function of potential for sunlit calculations.

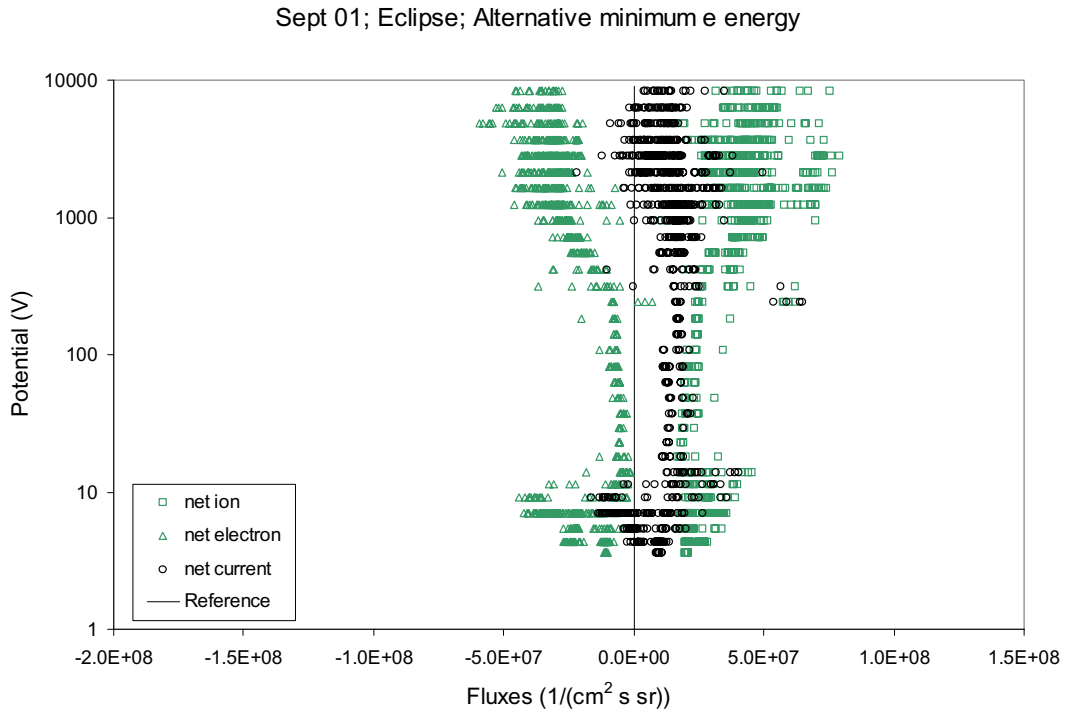


Figure 54. Net flux in eclipse using “alternative barrier” as the minimum electron energy.

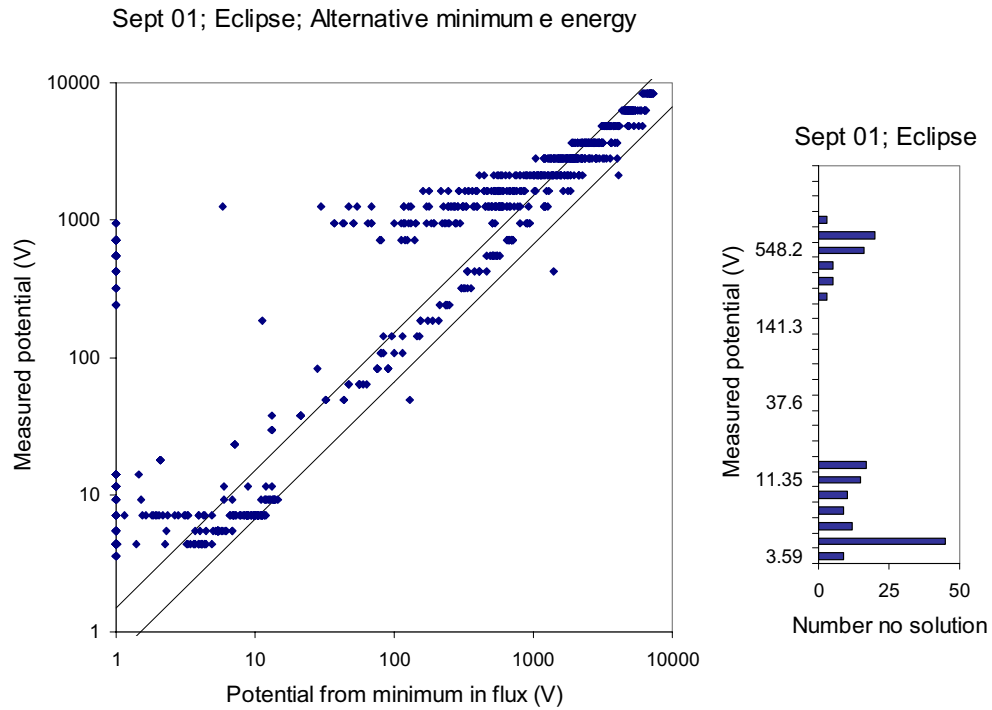


Figure 55. For Sept 01, eclipse data, measured potential as a function of the potential computed from the minimum in the net flux using “alternative barrier” as the minimum electron energy.

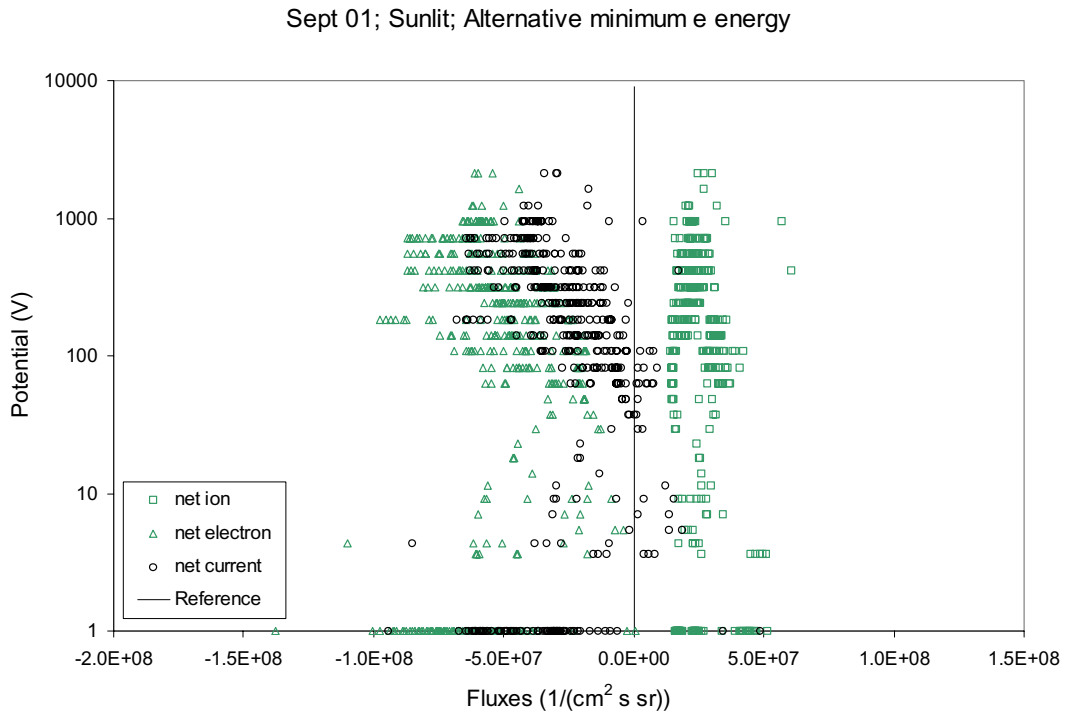


Figure 56. Net flux in sunlight using “alternative barrier” as the minimum electron energy.

7.4 Fraction Of Low Energy Electrons Escaping

Another factor that is not included in the above flux calculations is that not all secondary and photo electrons escape the spacecraft. (Backscattered electrons have higher energies and are unlikely to be trapped.) Let γ be the fraction that escape to infinity. Then we have that the total current, which on the timescale of MPA measurements is always equal to zero, is given by

$$\text{Total flux} = 0 = -F_e + F_i + F_{\text{back}} + \gamma F_{\text{sec}} + \gamma F_{\text{photo}}.$$

For each energy, we then have an expression for γ in terms of quantities that we have been calculating.

$$\gamma = \frac{F_e - F_i - F_{\text{back}}}{F_{\text{sec}} + F_{\text{photo}}}$$

The low energy flux to the MPA, which we have been carefully keeping out of our flux integrals, consists of low energy electrons that do not escape. The fraction of the created low energy flux that is measured by the MPA is given by

$$\beta = \frac{\text{measured low energy flux}}{F_{\text{sec}} + F_{\text{photo}}}$$

If the MPA is located at an “average” point on the spacecraft, $\gamma + \beta \sim 1$. These quantities are shown for eclipse periods and sunlit periods in Figure 57 and Figure 58 respectively. In eclipse, the average value of $\gamma + \beta$ computed in this way is 0.92, slightly under 1.0. In eclipse, the measured low energy flux is a useful representation of the average low-energy return flux. The value of γ is about 0.8. As expected, this approach does not work as well in sunlight. There is a great deal of scatter in the points. A photoemission flux of $2.9 \times 10^8 \text{ (cm}^2 \text{ s sr)}^{-1}$ ($2.9 \times 10^{-6} \text{ A m}^{-2}$) is needed to make the average value of $\gamma + \beta$ equal 1.0. This is approximately half of the value given in Feuerbacher and Fitton [1972] for photoemission flux from graphite in sunlight. With this value for photoemission, the average value of γ is 0.28 and the average value of β is 0.72. If we assume that only 81% of the secondary electrons escape, the net fluxes look as shown in Figure 59. The net flux is essentially zero over the entire range. The estimated potential is shown in Figure 60. 65% of the points have a solution within a factor of 1.5, 87% of the points have a solution within a factor of 3, and 8% cannot find a solution. Almost all of the points for which no solution can be found have a potential below 30 V.

Sept 01; Eclipse; Alternative minimum e energy

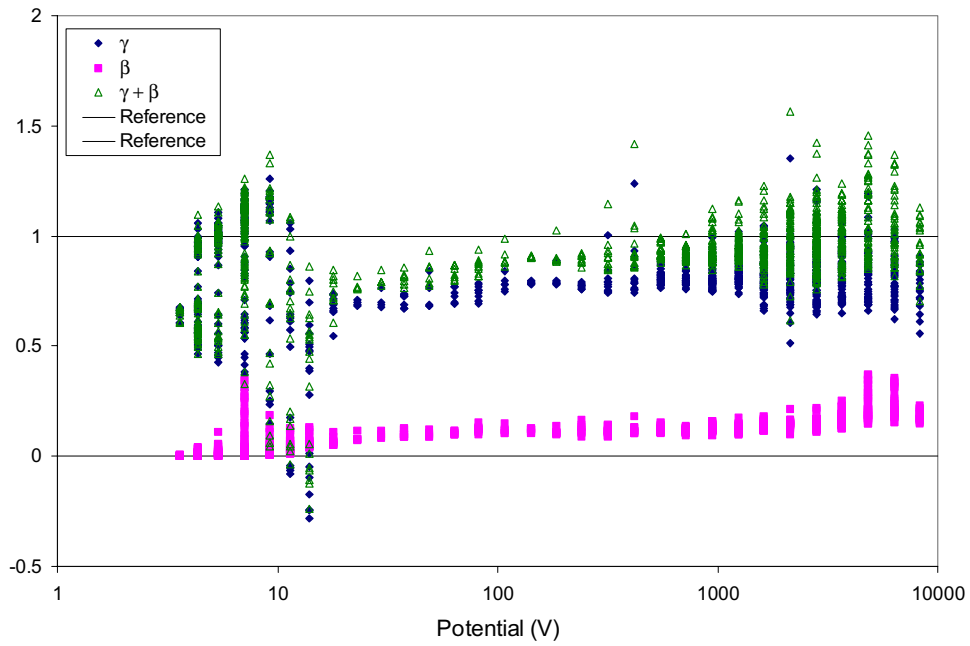


Figure 57. Measures of escaping and returning low energy fluxes in eclipse.

Sept 01; Sunlit; Alternative minimum e energy

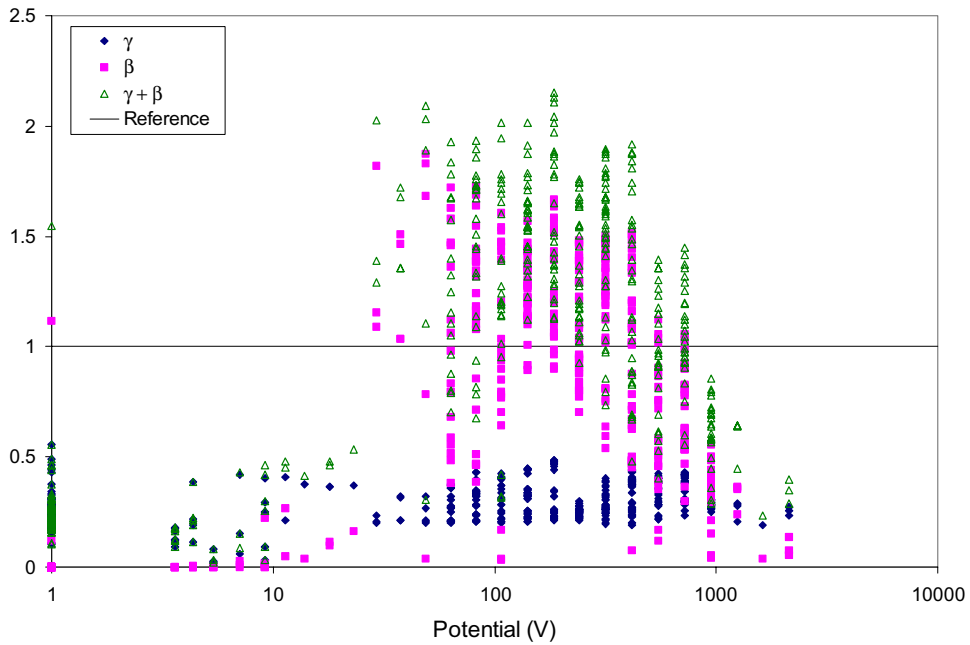


Figure 58. Measures of escaping and returning low energy fluxes in sunlight.

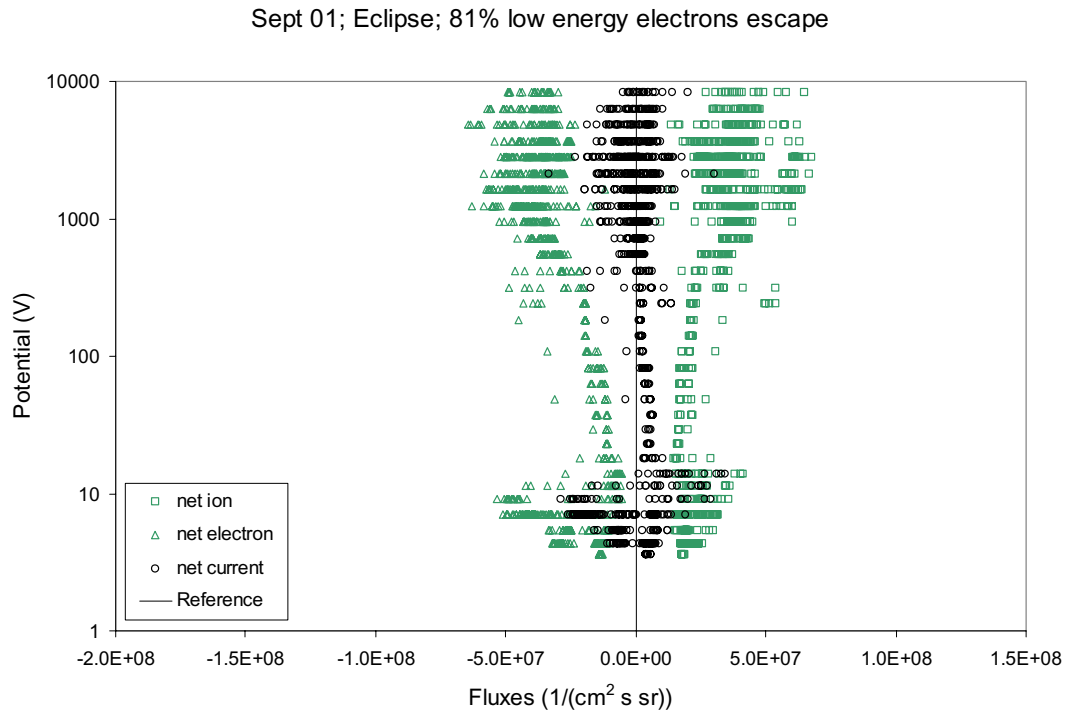


Figure 59. Net flux in eclipse with alternative minimum electron energy and 81% escape fraction.

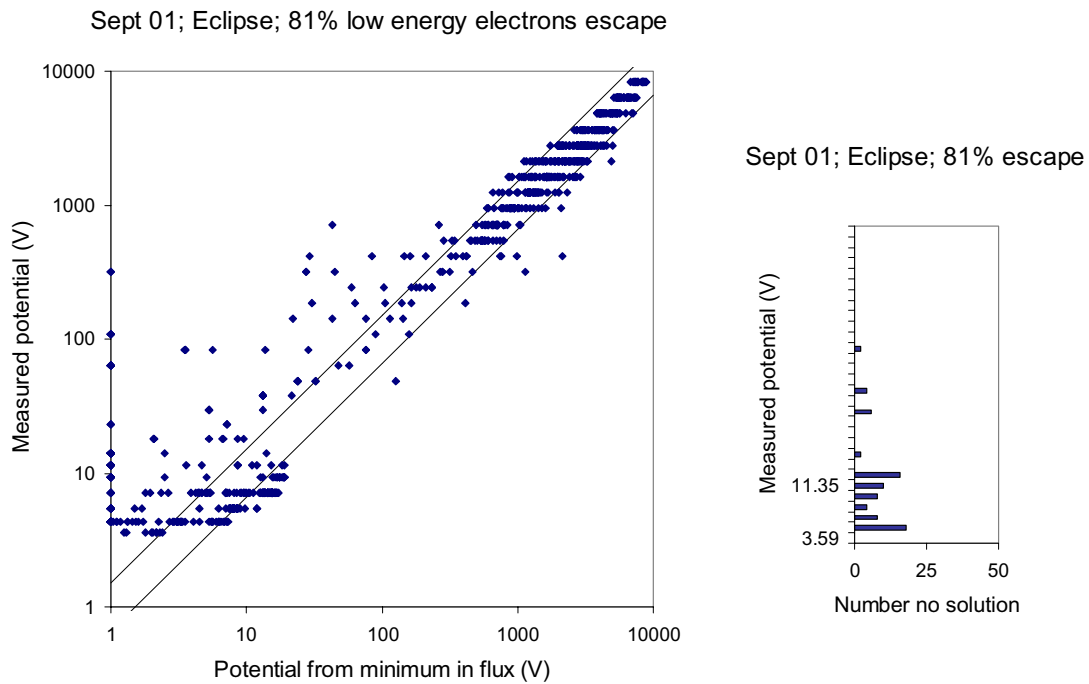


Figure 60. For Sept 01, eclipse data, measured potential as a function of the potential computed from the minimum in the net flux with alternative minimum electron energy and 81% escape fraction.

7.5 Modeling Sunlit Charging

In sunlight, photoemission that escapes from the spacecraft contributes to the net current. Above, we wrote the photoemission contribution to the net flux as $\gamma_p(\phi') f_{\text{sunlit}} F_{\text{photo}}(\phi')$. In order to estimate this term, we first look at the net flux, Figure 61, and estimated potential, Figure 62, without this term. The net flux is generally negative and is increasing negative as the potential increases. The way to understand this dependence is as follows. The amount of photoemission created is independent of the potential, but the barrier that develops with time depends on the differential potential. A more energetic environment with higher fluxes charges the spacecraft more. The incident electron flux is not attenuated significantly at the under kilovolt potentials seen in the sunlight charging. Therefore the photoemitted flux that is able to escape increases with potential.

The estimated potential ignoring photoemission is an overestimate as the computed net flux is negative, rather than near zero as it would be if we accounted for photoemission.

In order to estimate the photoemission term, we plot the average net flux as a function of potential, Figure 63. We fit a straight line to the portion of the semi-log plot that looks linear. The fit gives $J_{\text{photo}}(\phi) = 8 \times 10^7 (0.17 \ln(|\phi|) - 0.38)$ in units of $1/(\text{cm}^2 \text{ s sr})$. $8 \times 10^7/(\text{cm}^2 \text{ s sr})$ is equivalent to $8 \times 10^{-7} \text{ Amps/m}^2$. Feuerbacher and Fitton [1972] give a value of $7.2 \times 10^{-6} \text{ Amps/m}^2$ for the average photoemission rate of graphite in sunlight. Assuming a fraction sunlit of about 1/2, the coefficient is about 5 times smaller than the photoemission flux from graphite. We estimate the photoemission term to be given by

$$\gamma_p(\phi) f_{\text{sunlit}} F_{\text{photo}}(\phi) = 8 \times 10^7 \times \min\left(1, \max\left(0, (0.17 \ln(|\phi|) - 0.38)\right)\right)$$

At potentials less negative than -9.4 V, the escaping photoemitted current is zero. At potentials more negative than -3.35 kV, the escaping photoemitted current is $8 \times 10^7/(\text{cm}^2 \text{ s sr})$, about 20% of the available photoemitted current.

Figure 65 shows the resulting potentials as a function of the estimated potential. 48% of the points are within 1.5 of the measured potential and 81% of the points are within a factor of 3 of the measured potential. This includes 21% for which the algorithm correctly identified potentials near or below 1 V. Overall, this procedure provides a moderately quantitative prediction of chassis potential in sunlight.

That the results are less well behaved than the eclipse data is not surprising. The development of potential barriers and the resulting amount of photocurrent that escapes is, in general, strongly dependent on the spacecraft shape and orientation with respect to the sun and the time in which the spacecraft has been charging along with the incident electron and ion spectra.

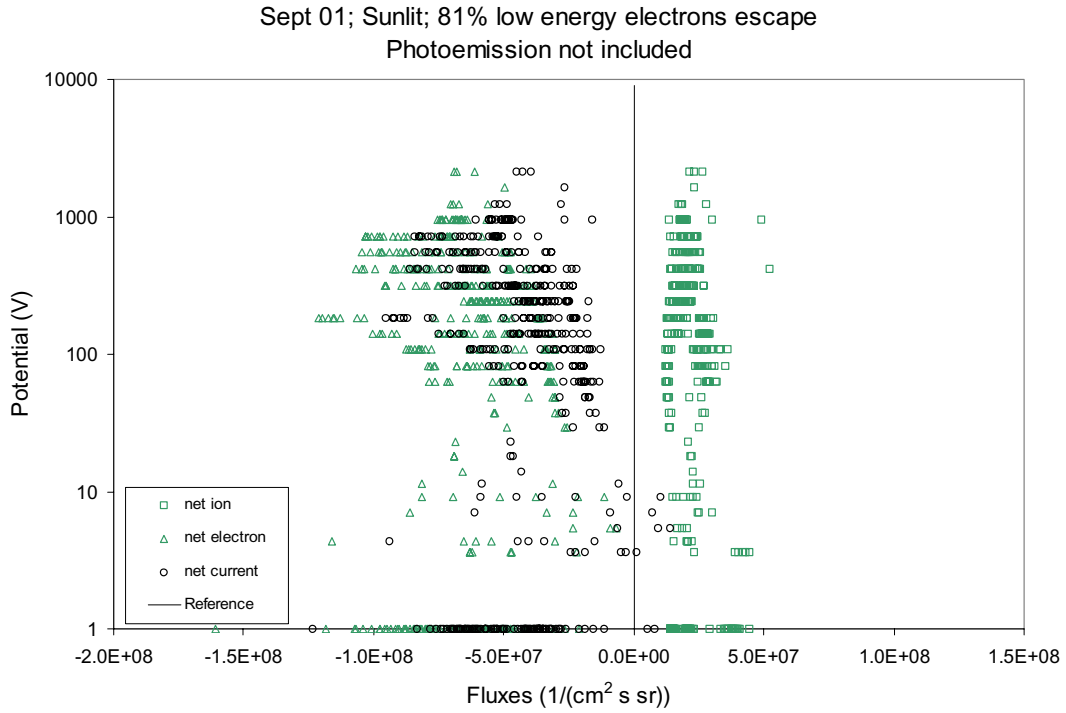


Figure 61. Net flux in sunlight with alternative minimum electron energy, 81% escape fraction, and ignoring photoemission.

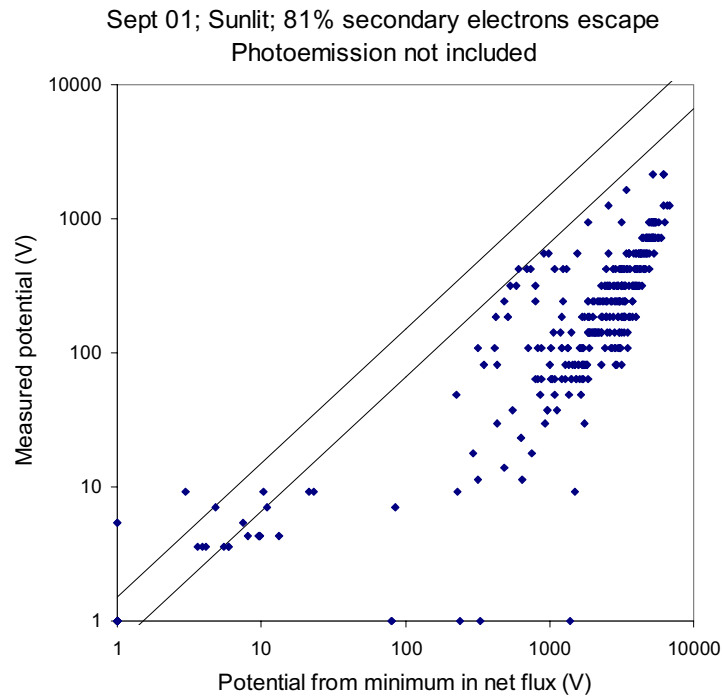


Figure 62. For Sept 01, sunlit data, assuming 81% of the secondary electrons escape, and ignoring photoemission, measured potential as a function of potential computed from the minimum in the net flux. The lines are $y = 1.5x$ and $y = x/1.5$.

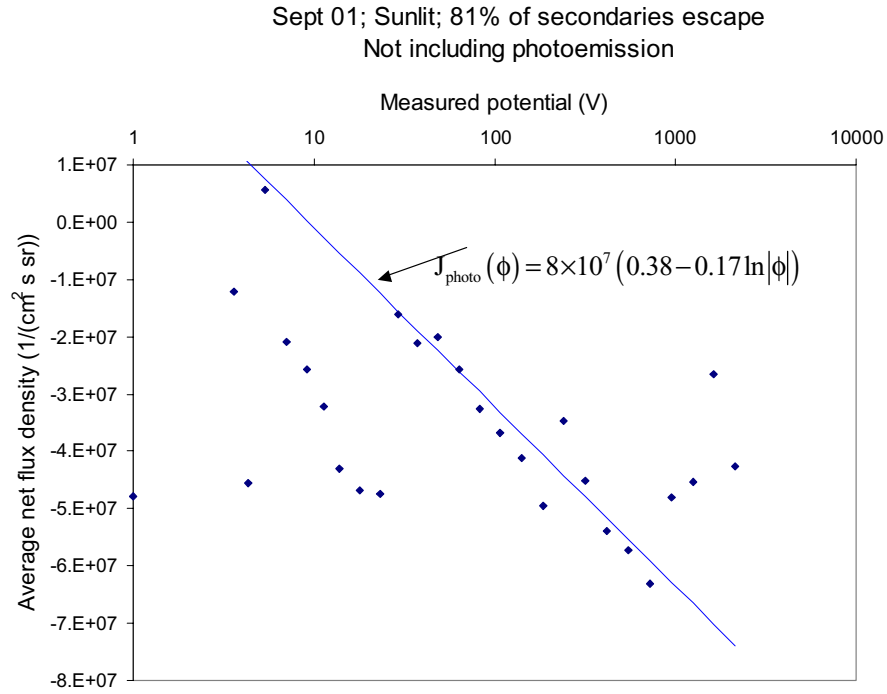


Figure 63. Average net flux (ignoring photoemission) as a function of potential for the Sept 01, sunlit dataset. The line is a fit to the average net flux for potentials between -30 and -948 V.

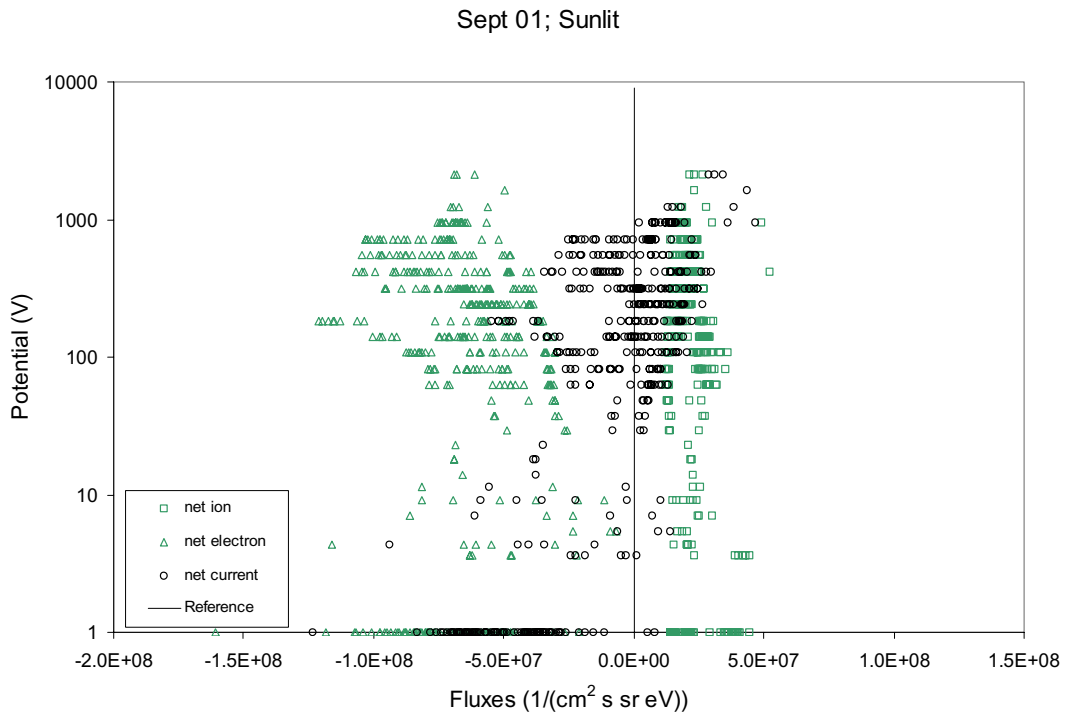


Figure 64. Net flux in sunlight with alternative minimum electron energy, 81% escape fraction, and including photoemission.

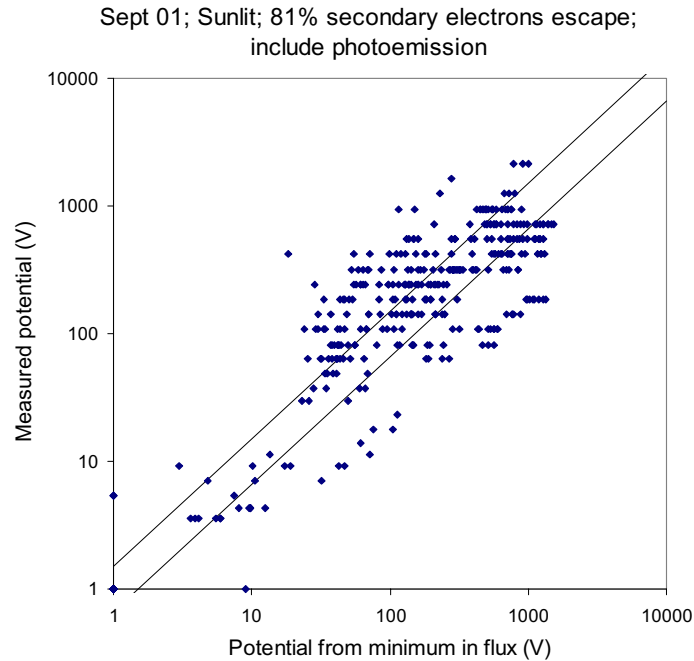


Figure 65. For Sept 01, sunlit data, assuming 81% of the secondary electrons escape, and including photoemission, measured potential as a function of potential computed from the minimum in the net flux. The lines are $y = 1.5x$ and $y = x/1.5$. The bar chart at the right shows the number of spectra for which no solution was found for each value of measured potential. These points are represented in the plot on the left by a single diamond along the left hand axis.

7.6 Alternative Predictors

In evaluating our ability to predict potential from the measured spectra, we need to compare our approach with other approaches.

LANL has previously reported that there is a relationship between the electron temperature calculated as described in Section 0 and the spacecraft chassis potential. Separate power law fits were developed for eclipse and sunlit conditions. For eclipse

$$\phi = 1.74 \times 10^{-5} \theta^{2.26}$$

and for sunlight

$$\phi = 2.4 \times 10^{-7} \theta^{2.51}.$$

The relationship only applies if the flux is above a threshold value. In eclipse, this relationship, shown in Figure 55, is as good a predictor as ours above a kilovolt, but gives consistently too high a potential below that. It does not work when the measured potential is below about 30 V. It may predict potentials of the order of 100 V.

In sunlight, this relationship, shown in Figure 67, doesn't work quite as well as the one we developed, shown in Figure 65. 30% of the points are within a factor of 1.5 and 85% are within a factor of 3. It underestimates the potential by more than a factor of 1.5 for more than half of the spectra. It also often predicts a significant potential when the measured potential is under 1 V (a large peak in the lowest energy ion channel).

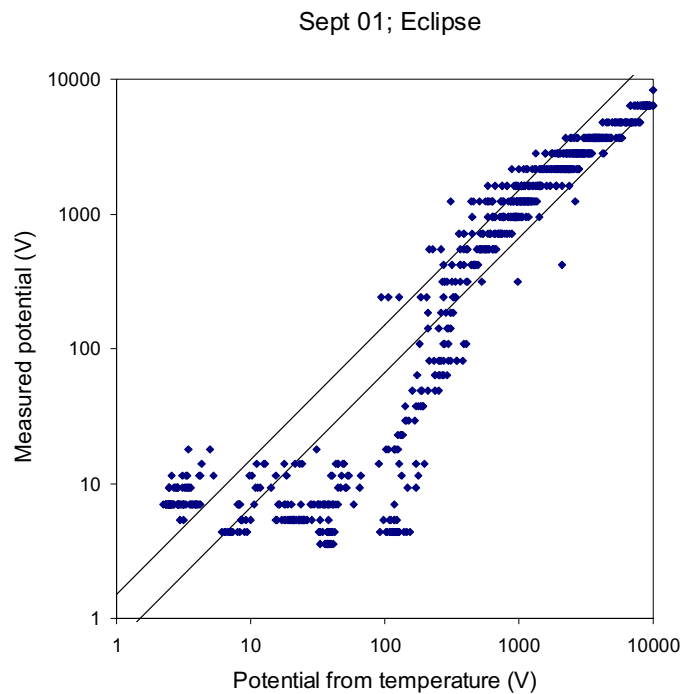


Figure 66. For Sept 01, eclipse data, measured potential as a function of $\phi = 1.74 \times 10^{-5} \theta^{2.26}$ for eclipse Sept 01 dataset.

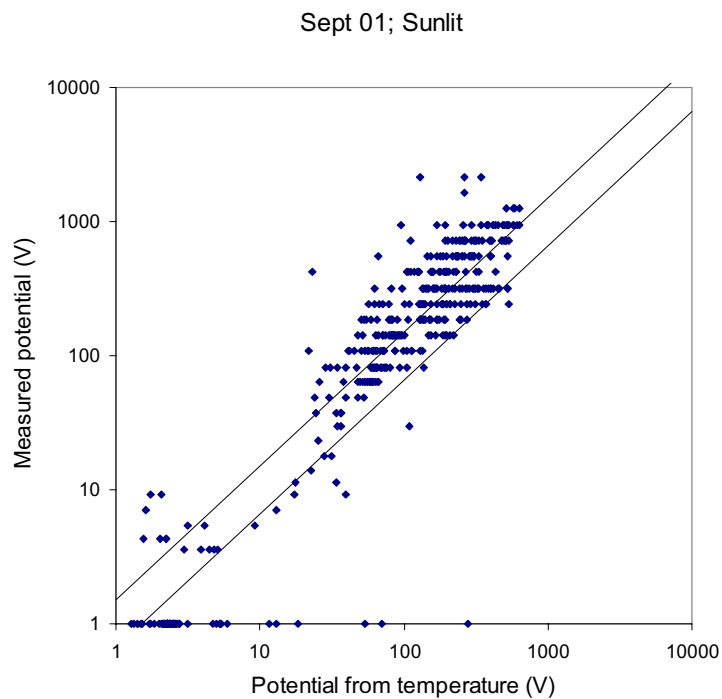


Figure 67. For Sept 01, sunlit data, measured potential as a function of $\phi = 2.4 \times 10^{-7} \theta^{2.51}$ for sunlit Sept 01 dataset.

We also examined the incident electron flux in the higher energy channels as possible predictors of the potential. We examined single channels and all channels above a specific energy. The best predictor for the September 2001, eclipse dataset is the sum of the bins from 9123 V and above. The best fit to this dataset is

$$\phi_{\text{estimated}} = 1.359 \times 10^{-12} \sum_{E > 9123} (\text{measured flux} \times \text{bin width})^{2.03}.$$

This approach always provides a potential estimate. It works best at the highest potentials. It is not as good a predictor as the temperature.

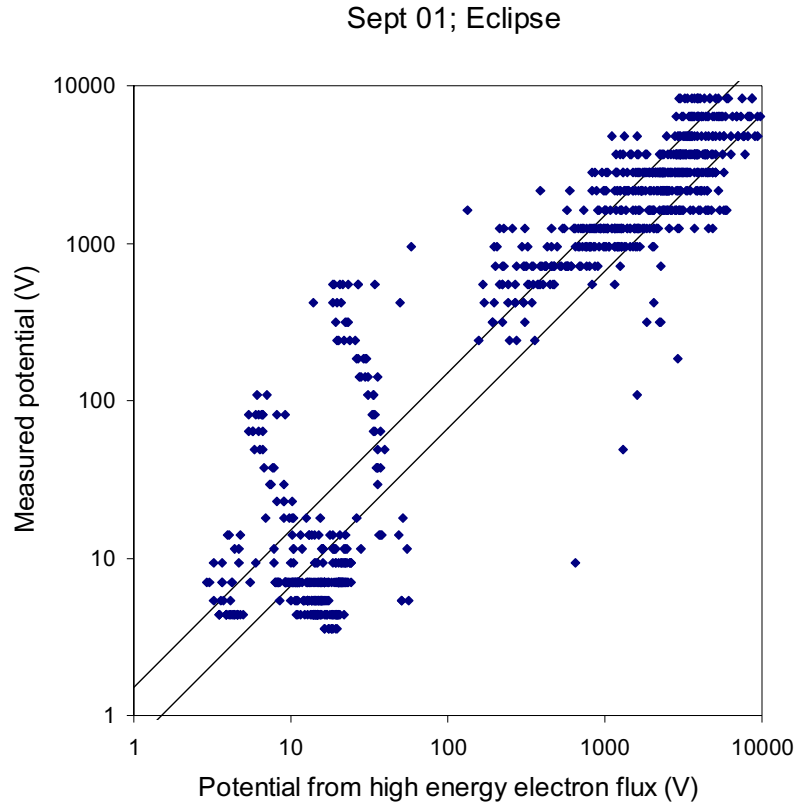


Figure 68. For Sept 01, eclipse data, measured potential as a function of $1.359 \times 10^{-12} \sum_{E > 9123} (\text{measured flux} \times \text{bin width})^{2.03}$ for sunlit Sept 01 dataset.

8 Comparison Of Solar Maximum And Solar Minimum

As shown in Figures 69-72, the fluxes and resulting charging during charging periods are the same at solar minimum as at solar maximum. What varies is the frequency of high charging environments, with less frequent charging events at solar minimum.

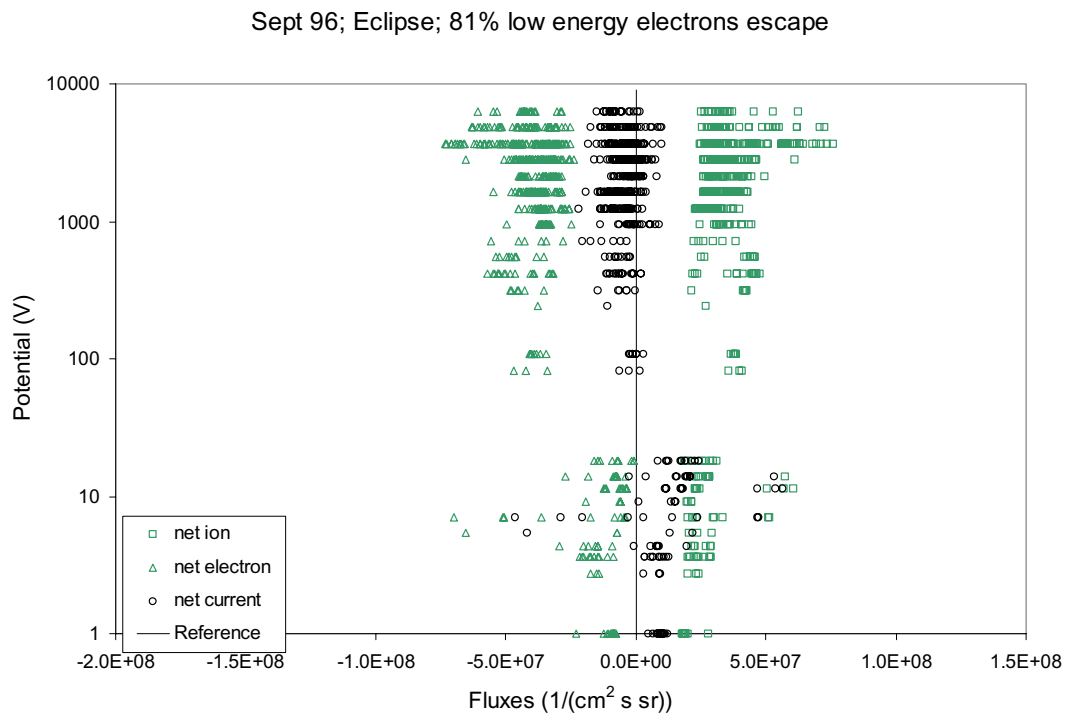


Figure 69. For Sept 96, net flux in eclipse with alternative minimum electron energy and 81% escape fraction. (Compare with Figure 59.)

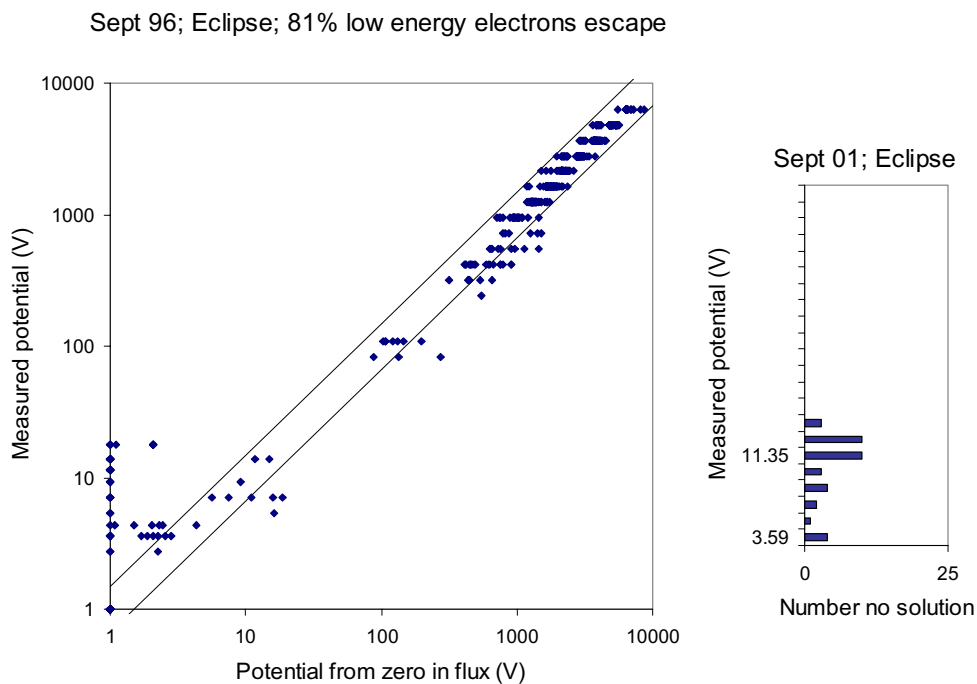


Figure 70. For Sept 96, eclipse data, assuming 81% of the secondary electrons escape, measured potential as a function of potential computed from the minimum in the net flux. (Compare with Figure 60.)

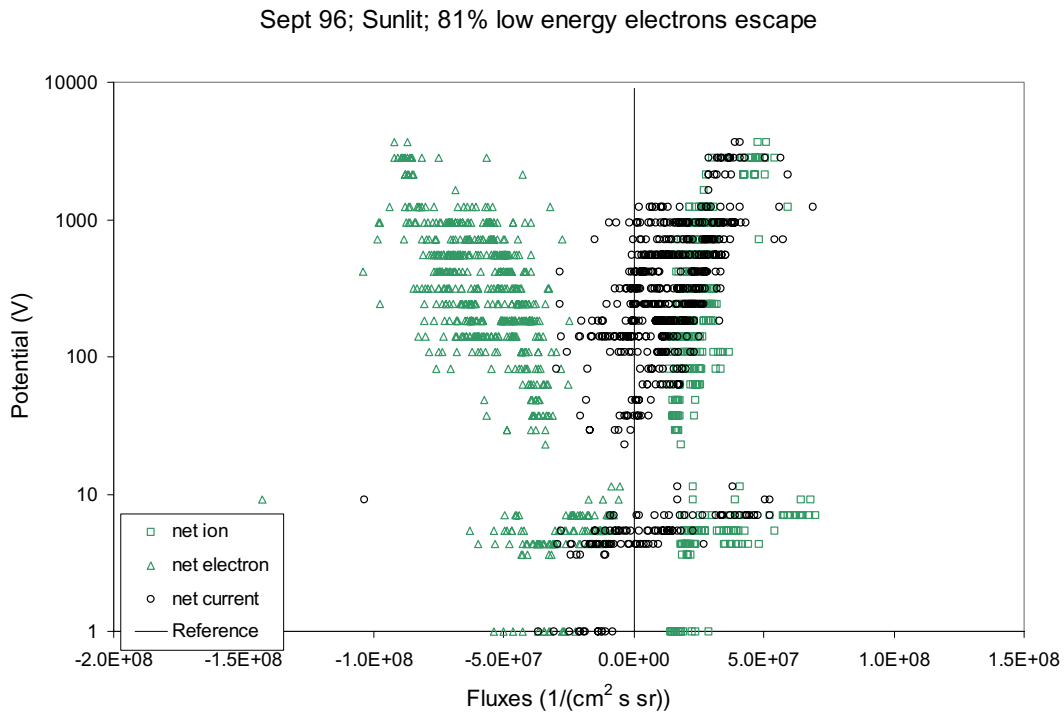


Figure 71. For Sept 96, net flux in sunlight with alternative minimum electron energy, 81% escape fraction, and including photoemission. (Compare with Figure 64.)

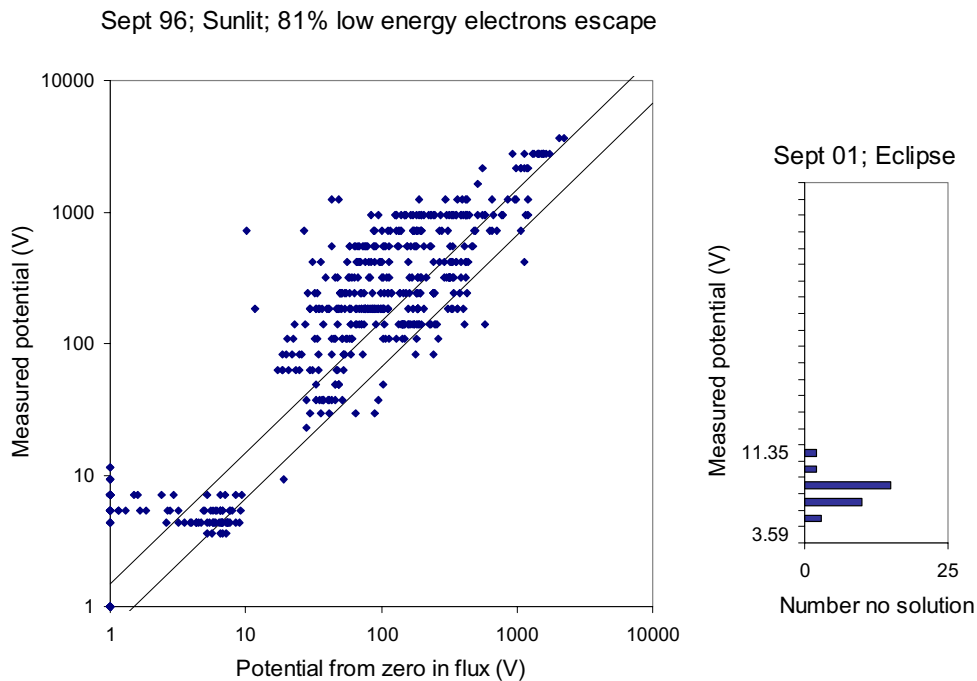


Figure 72. For Sept 96, sunlit data, assuming 81% of the secondary electrons escape, and including photoemission, measured potential as a function of potential computed from the minimum in the net flux. (Compare with Figure 65.)

9 Comparison With Data From Another LANL Spacecraft

To further check the validity of our calculations, we did a single calculation using a dataset from another of the LANL spacecraft. The results are shown in Figure 73 and Figure 74.

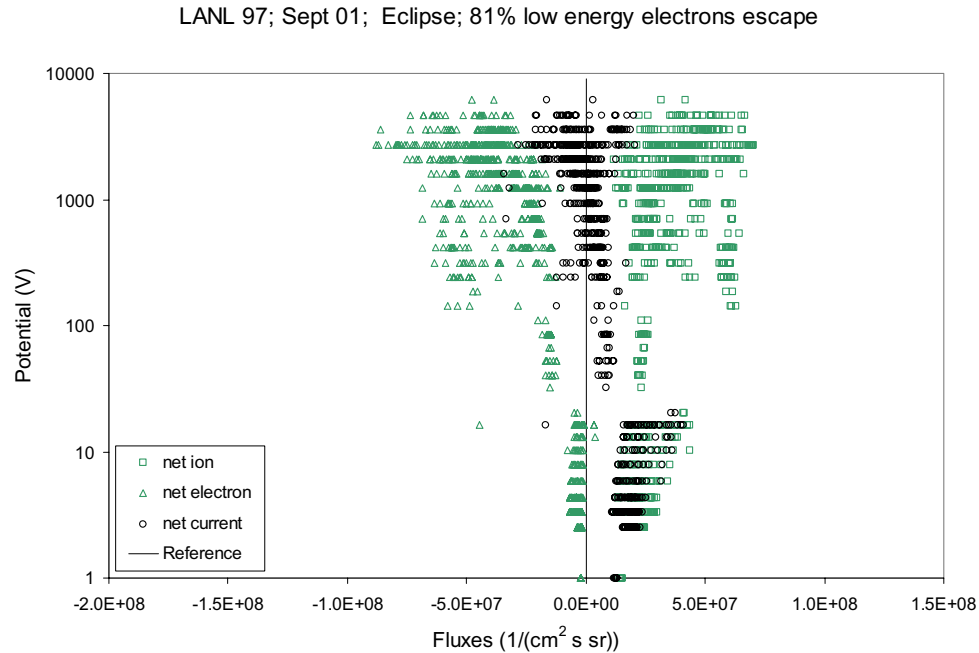


Figure 73. For LANL 97 spacecraft, net flux in eclipse with alternative minimum electron energy and 81% escape fraction. (Compare with Figure 59.)

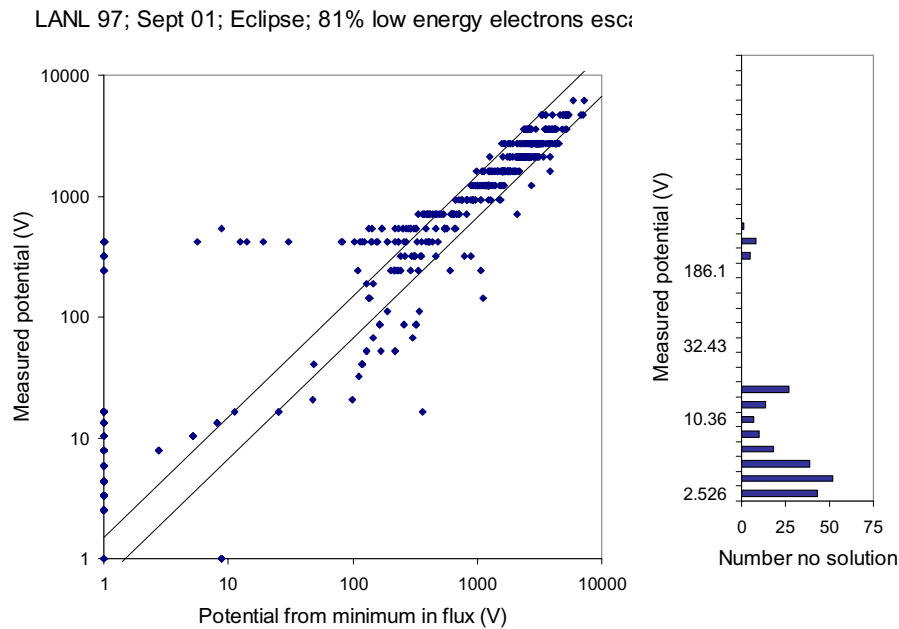


Figure 74. For Sept 01, eclipse data from LANL 97 spacecraft, assuming 81% of the secondary electrons escape, measured potential as a function of potential computed from the minimum in the net flux. (Compare with Figure 60.)

10 Fitting Techniques And Results

The goal of this research is to better understand the plasma environment that causes spacecraft charging and determine a relatively simple characterization of the full particle distributions that yields an accurate prediction of the observed charging under a wide variety of conditions. The computer codes that compute spacecraft charging in a tenuous plasma environment (NASCAP/GEO [Katz, *et al*, 1979], SEE Spacecraft Charging Handbook [Katz, *et al*, 2000], and NASCAP-2K [Davis, *et al*, 2002]) use a Maxwellian distribution function. Originally the Maxwellian distribution function was chosen for its simplicity and no one has ever established its adequacy or inadequacy. In the late 70s and early 80s, when NASCAP/GEO was written, some calculations were attempted with measured spectra. The high noise level and low resolution of the measured spectra made the solutions unreliable, so Maxwellian fits are used today instead. We added to our flux computation code the ability to compute some analytic functional fits to the spectra. We can then use fit spectra in our calculations of moments of the distribution, the fluxes, and the computed potential.

The proposed functional forms are appropriate for the flux at infinity. Before fitting the measured fluxes to a functional form, the flux is multiplied by the orbit limited $1-\phi/E$ factor and the energy is shifted by the potential.

$$F^{\infty}(E_{\infty}) = F^{\infty}(E_m \pm \phi) = F_m(E_m) \left(1 \pm \frac{\phi}{E_m}\right)$$

Six different functional forms have been implemented.

$$\text{Flux}^{\text{Maxwellian}}(E) = en \sqrt{\frac{1}{2\pi me\theta}} \frac{E}{\theta} \exp\left(-\frac{E}{\theta}\right)$$

$$\text{Flux}^{\text{DoubleMaxwellian}}(E) = en_1 \sqrt{\frac{1}{2\pi me\theta_1}} \frac{E}{\theta_1} \exp\left(-\frac{E}{\theta_1}\right) + en_2 \sqrt{\frac{1}{2\pi me\theta_2}} \frac{E}{\theta_2} \exp\left(-\frac{E}{\theta_2}\right)$$

$$\text{Flux}^{\text{Kappa}}(E) = A E \left(1 + \frac{E}{\kappa E_0}\right)^{-\kappa-1}$$

$$\text{Flux}^{\text{Quadratic}}(E) = AE^2 + BE + C$$

$$\text{Flux}^{\text{Exponential}}(E) = A \exp(BE)$$

$$\text{Flux}^{\text{PowerLaw}}(E) = AE^N$$

The Kappa distribution was selected as Christon, *et al* [1989] have shown that it provides a good fit to the quiescent plasma sheet environment at greater than 12 R_E (Geosynchronous is at 6.6 R_E). The Kappa function has the shape of a Maxwellian at low energies and a power law at high energies, providing a high-energy tail to the distribution. The active magnetosphere is more complex [Christon, *et al*, 1991]. We are looking for a simple model of the environment so we use a single Kappa distribution.

The Maxwellian, Double Maxwellian, and Kappa distribution functions were written for the purpose of fitting the flux. The exponential and power law fitting procedures were written to

assist in the extrapolation of the measured data to higher energies. The quadratic fitting procedure was developed for finding the minimum in one of the procedures we tried (and discarded) to determine the best value to use as the low energy cutoff in the electron integrals.

Two least-square fitting procedures were developed. The power law, exponential, and Maxwellian functions are fit by taking logarithms of the flux and the energy, as appropriate, and computing the best-fit straight line. Each point is weighted by the bin width. The fitting procedure (lfit from *Numerical Recipes* [Press, *et al.* 1992]) finds values for a and b that minimize the expression

$$\sum_i (\Delta_i (y_i - a - bx_i))^2$$

where

Δ_i	bin width,
y_i	logarithm of the flux at infinity (power law and exponential) or the difference between the logarithm of the flux at infinity and the logarithm of the energy (Maxwellian),
x_i	energy (exponential and Maxwellian) or the logarithm of the energy (power law).

The Double Maxwellian, Kappa, and Quadratic functions are fit using the Levenberg-Marquardt method for nonlinear least-squares fitting. The algorithm and an implementation in C are described in *Numerical Recipes* [Press, *et al.* 1992]. Again the points are weighted by the bin width. The fitting procedure finds the vector **a** that minimizes the expression

$$\sum_i (\Delta_i (y_i - f(\mathbf{a}, x_i)))^2$$

where

Δ_i	bin width,
y_i	flux at infinity,
x_i	energy
f	functional form
a	vector of the constants in the functional form. For a quadratic, a = (A, B, C). For a Kappa distribution, a = (A, E _o , κ). For a double Maxwellian distribution, a = (n ₁ , θ ₁ , n ₁ *n ₂ , θ ₁ *θ ₂).

Both approaches are used to compute a single Maxwellian fit. The double Maxwellian fitting procedure can ignore the third and fourth parameters. We refer to a fit to a single Maxwellian using the first approach as a Maxwellian fit and a fit to a single Maxwellian using the second approach as a Single Maxwellian fit.

An alternative fitting procedure in which moments of the distribution are strictly preserved was proposed but not implemented.

In fitting ion spectra, the portion of the spectrum fit is from the highest energy bin through the energy bin just above the potential excluding energy bins in which the flux is below twice the one-count equivalent flux. This avoids all energy bins with possibly misleading count rates.

In fitting electron spectra, the portion of the spectrum fit is the range over which the flux integrals are done. This avoids all energy bins with possibly misleading count rates.

Figures 75 and 76 show fits of a charging spectrum and non-charging spectrum to various functional forms.

Moments and fluxes can be computed from fit distributions in exactly the same way as they are computed from the measured distributions. Results are shown in Figures 77-108. With fit distributions, it is possible to include energy bins that are not included in the integrals over the measured distribution, such as ion fluxes below twice the one-count flux equivalent, electron energy bins below the estimated potential barrier, and energy bins above the maximum of the instrument, 47 keV. We have the ability to use either approach. Figures 77-92 use the entire energy range and Figures 93-108 use only those energy bins used in the integrals over the measured distributions. The maximum energy chosen can affect the results a great deal, particularly when fitting the ions with a Kappa distribution, as the knee of the ion spectrum is often above 47 keV. Presently, the upper limit of the net flux integrals is about 100 keV.

Figures 109-124 show electron and ion component fluxes, net fluxes, and computed potentials with the fluxes computed from fits. These figures should be compared with Figures 29, 31, 59 and 60 computed using the measured fluxes directly. In these figures, the electrons and ions use the same analytic form for the fit distribution function. The figures using the Maxwellian, Single Maxwellian, and Double Maxwellian fits are similar with no improvement in predictive ability using the additional two parameters of the Double Maxwellian. The Kappa distribution provides a very poor estimate of the ion fluxes.

Figures 125-136 show the measured and computed potentials using the various combinations of distribution function analytic forms. The accuracy is summarized in Table 2. Using Maxwellian fits is never as accurate as using the measured fluxes directly. However, using a Kappa distribution for the electrons and either single Maxwellian for the ions gives results similar to those obtained from the measured fluxes directly.

In a number of the measured potential versus computed potential figures, there are a handful of points in the lower right hand corner. These points have measured potentials on the order of 10 V and computed potentials on the order of a few hundred volts. For several of these cases, the temperature for the Maxwellian fit to the ion spectrum is of the order of a thousand and there is a peak in the measured spectrum around 10 V. Upon careful examination it appears that the fitting procedure is missing the low energy peak as there are far more points in the higher energy portion of the spectrum. The fits would provide more accurate potential calculations if additional intelligence to look for this feature were added to the fitting procedure.

Table 3 compares the results including all energy bins in the flux integrals with results using only those bins used in the sums computed using the measured fluxes directly. Neither approach provides more consistently accurate potential computations.

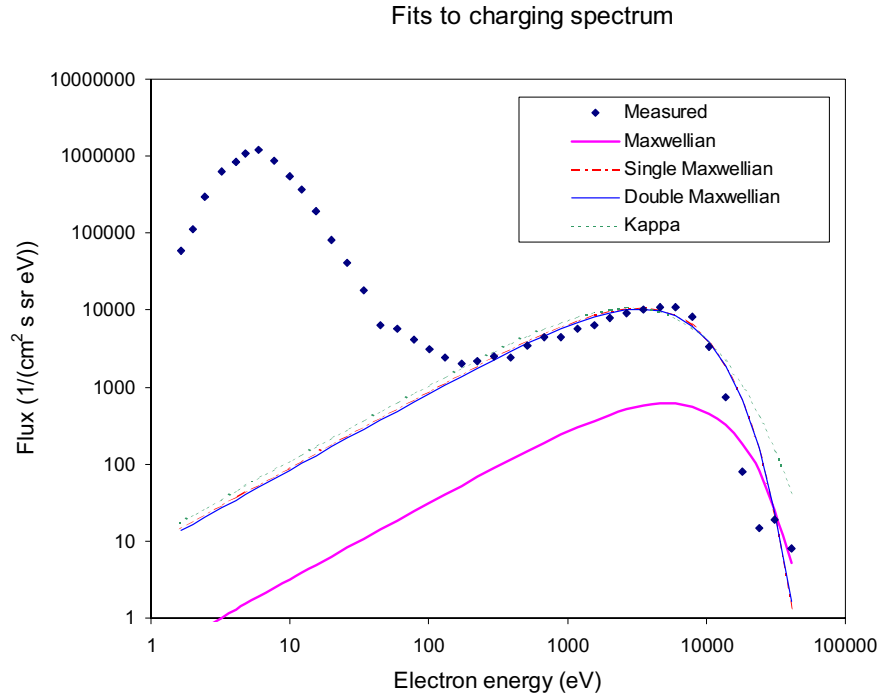


Figure 75. A sample charging flux spectrum and various fits to it using different functional forms.

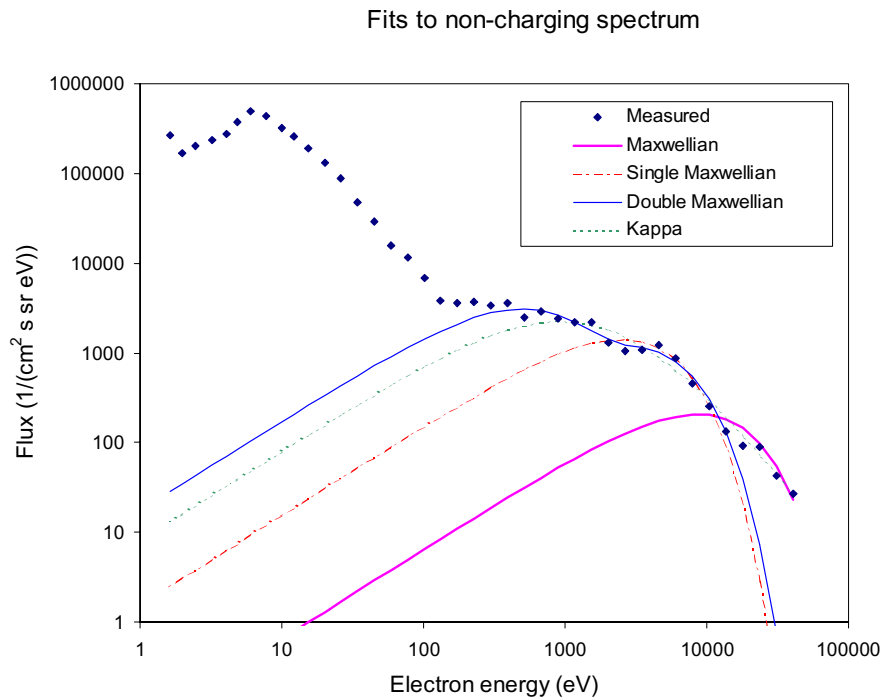


Figure 76. A sample non-charging flux spectrum and various fits to it using different functional forms.

Sept 01; Eclipse; Maxwellian fits

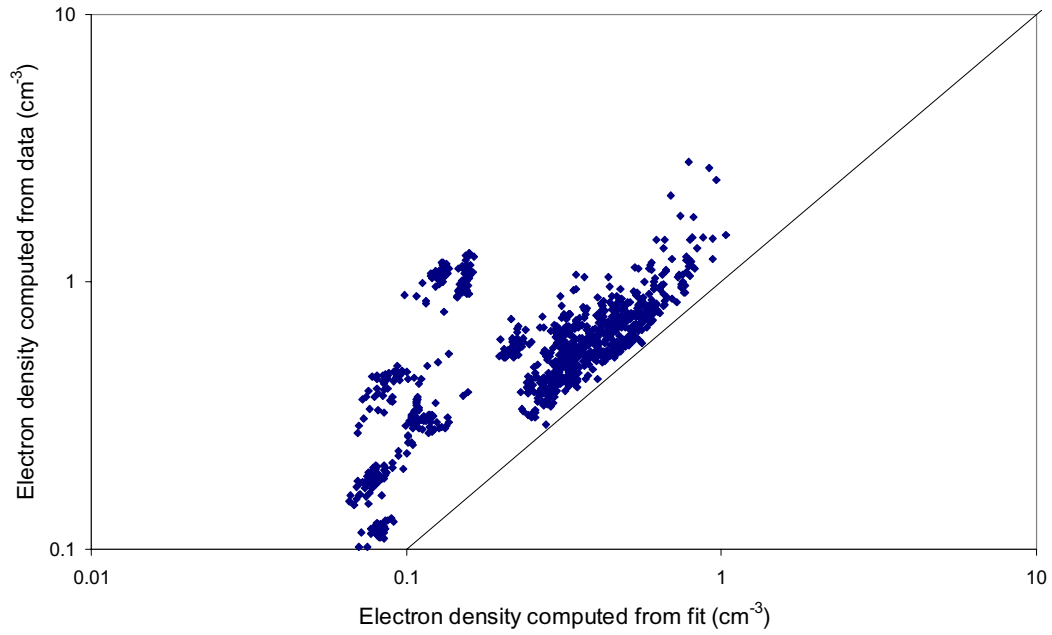


Figure 77. Electron density computed from data compared with electron density computed from fit to Maxwellian. Integral over fit extends from 1 eV to 100 keV.

Sept 01; Eclipse; Maxwellian fits

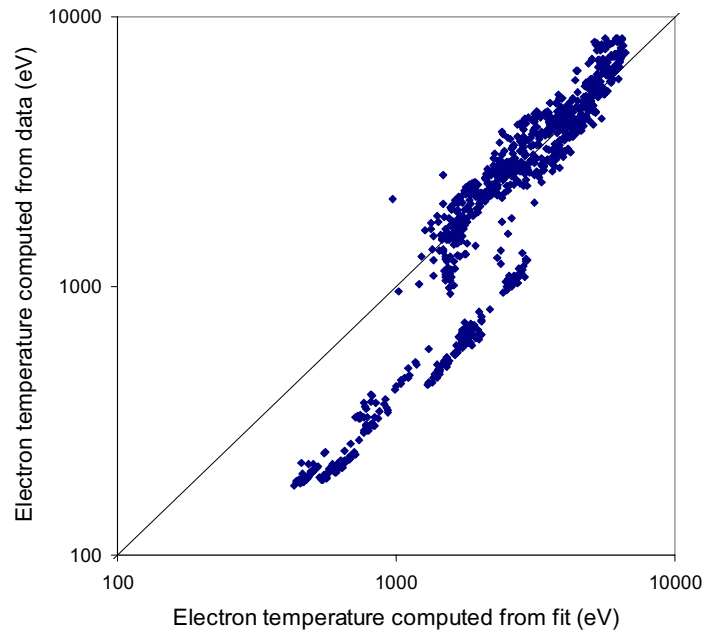


Figure 78. Electron temperature computed from data compared with electron temperature computed from fit to Maxwellian. Integral over fit extends from 1 eV to 100 keV.

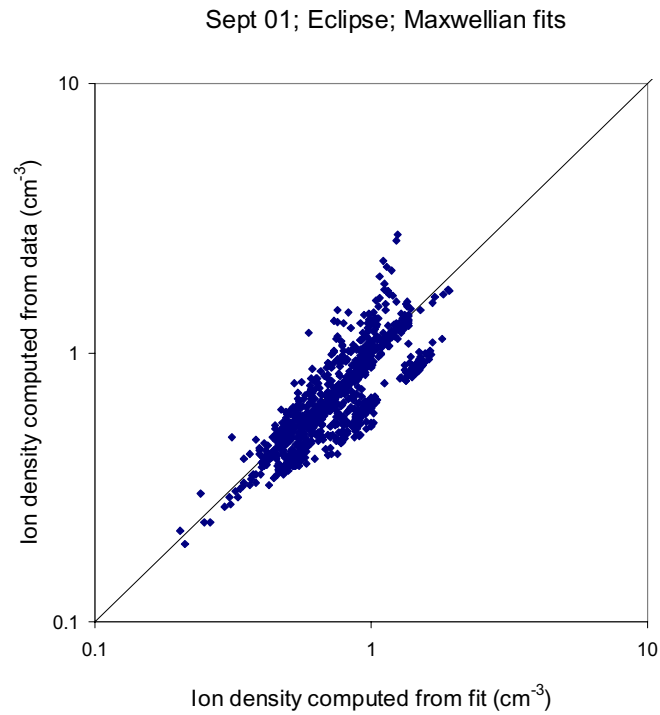


Figure 79. Ion density computed from data compared with ion density computed from fit to Maxwellian. Integral over fit extends from 1 eV to 100 keV.

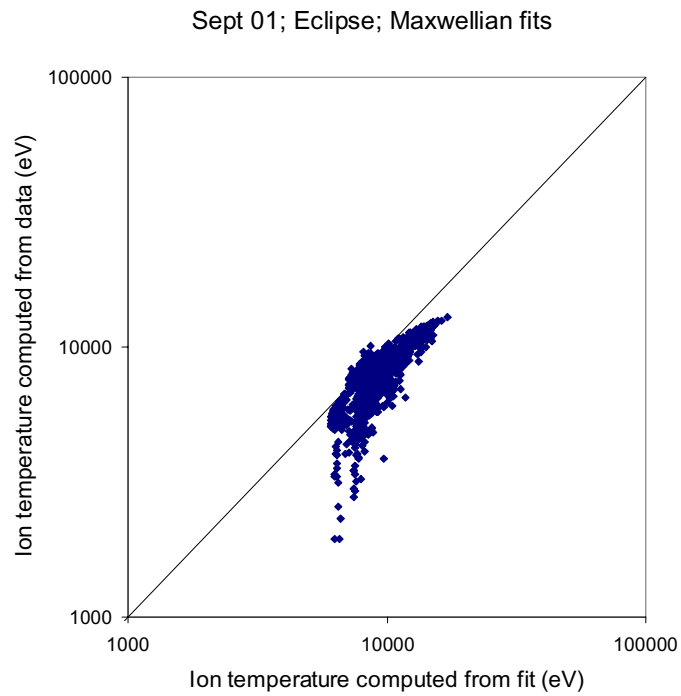


Figure 80. Ion temperature computed from data compared with ion temperature computed from fit to Maxwellian. Integral over fit extends from 1 eV to 100 keV.

Sept 01; Eclipse; Single Maxwellian fits

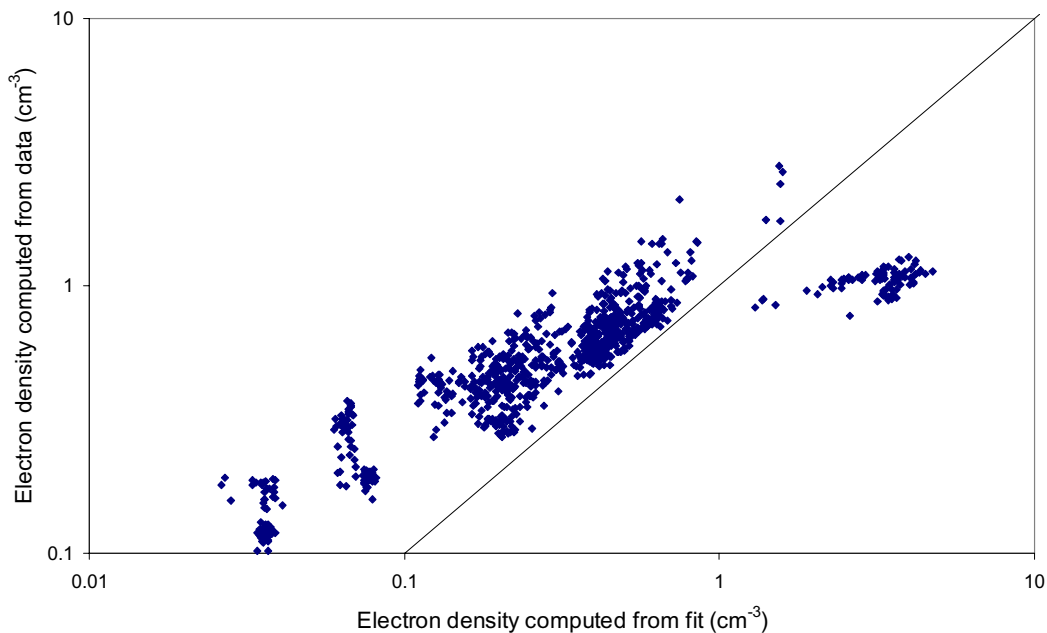


Figure 81. Electron density computed from data compared with electron density computed from fit to Single Maxwellian. Integral over fit extends from 1 eV to 100 keV.

Sept 01; Eclipse; Single Maxwellian fits

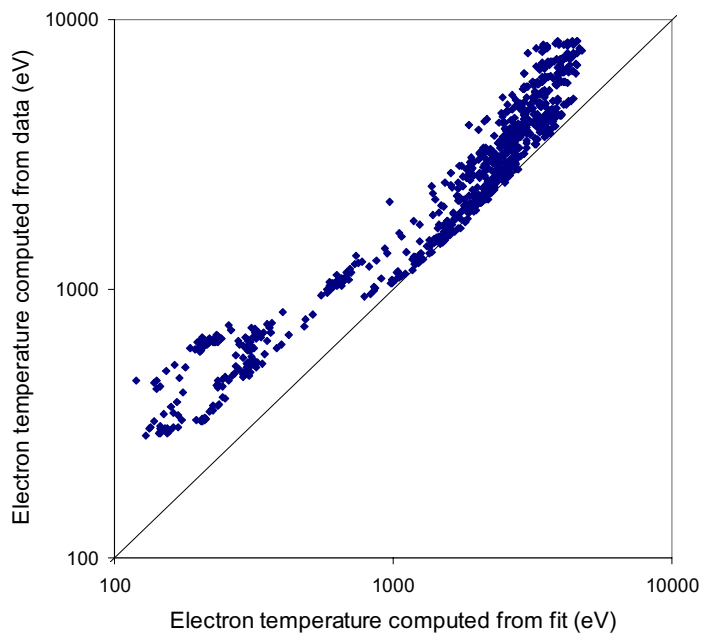


Figure 82. Electron temperature computed from data compared with electron temperature computed from fit to Single Maxwellian. Integral over fit extends from 1 eV to 100 keV.

Sept 01; Eclipse; Single Maxwellian fits

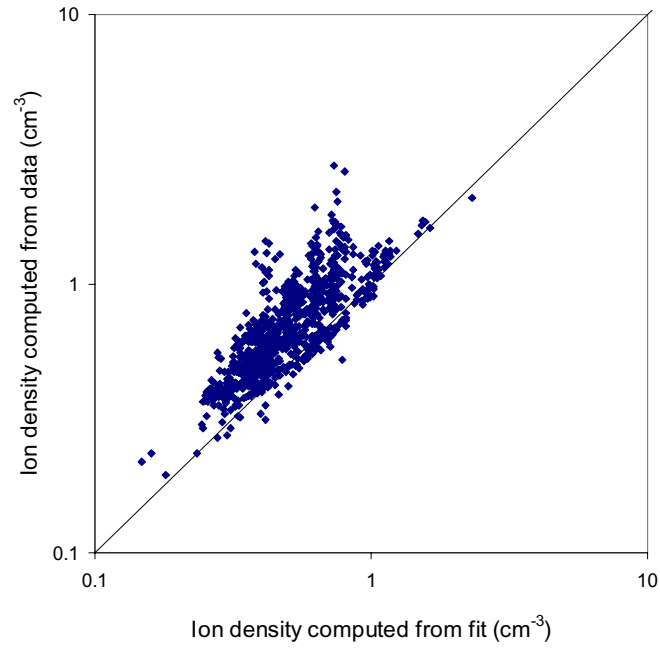


Figure 83. Ion density computed from data compared with ion density computed from fit to Single Maxwellian. Integral over fit extends from 1 eV to 100 keV.

Sept 01; Eclipse; Single Maxwellian fits

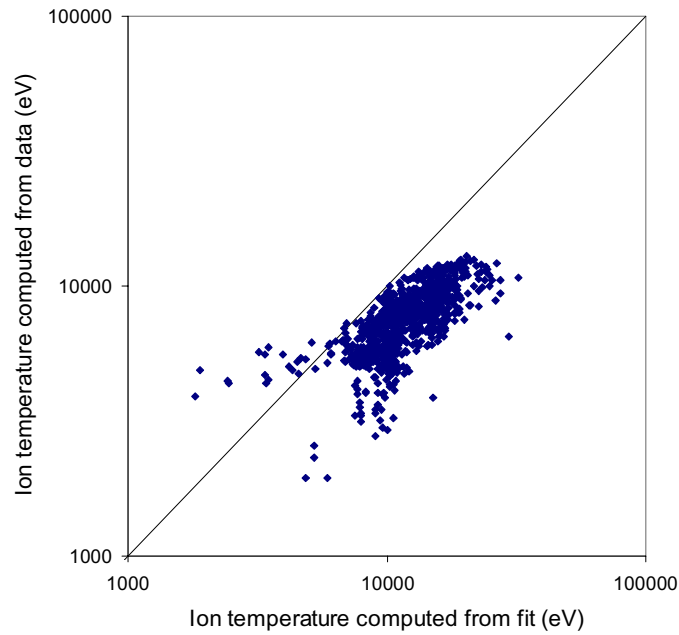


Figure 84. Ion temperature computed from data compared with ion temperature computed from fit to Single Maxwellian. Integral over fit extends from 1 eV to 100 keV.

Sept 01; Eclipse; Double Maxwellian fits

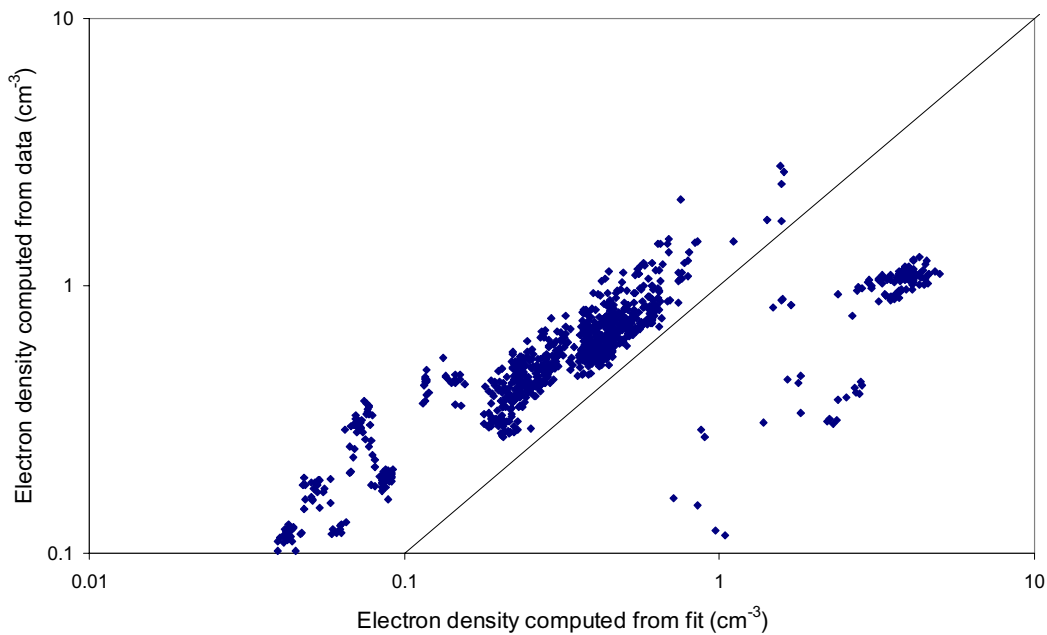


Figure 85. Electron density computed from data compared with electron density computed from fit to Double Maxwellian. Integral over fit extends from 1 eV to 100 keV.

Sept 01; Eclipse; Double Maxwellian fits

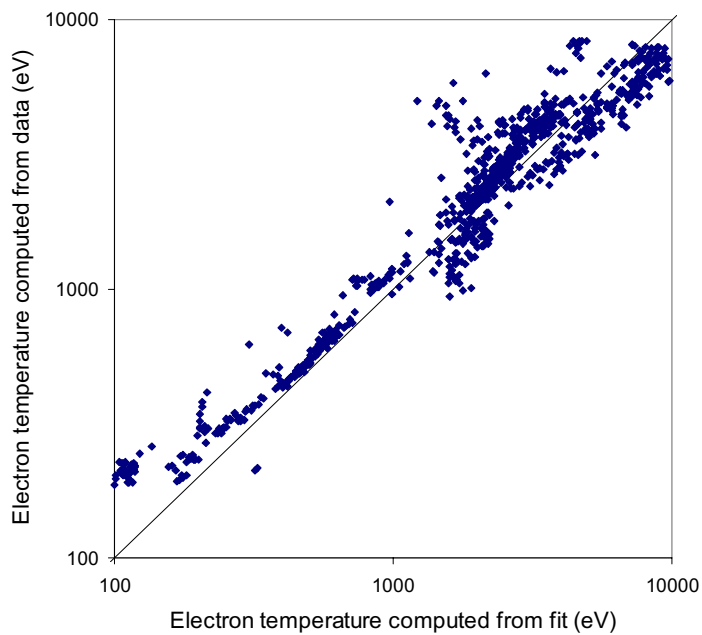


Figure 86. Electron temperature computed from data compared with electron temperature computed from fit to Double Maxwellian. Integral over fit extends from 1 eV to 100 keV.

Sept 01; Eclipse; Double Maxwellian fits

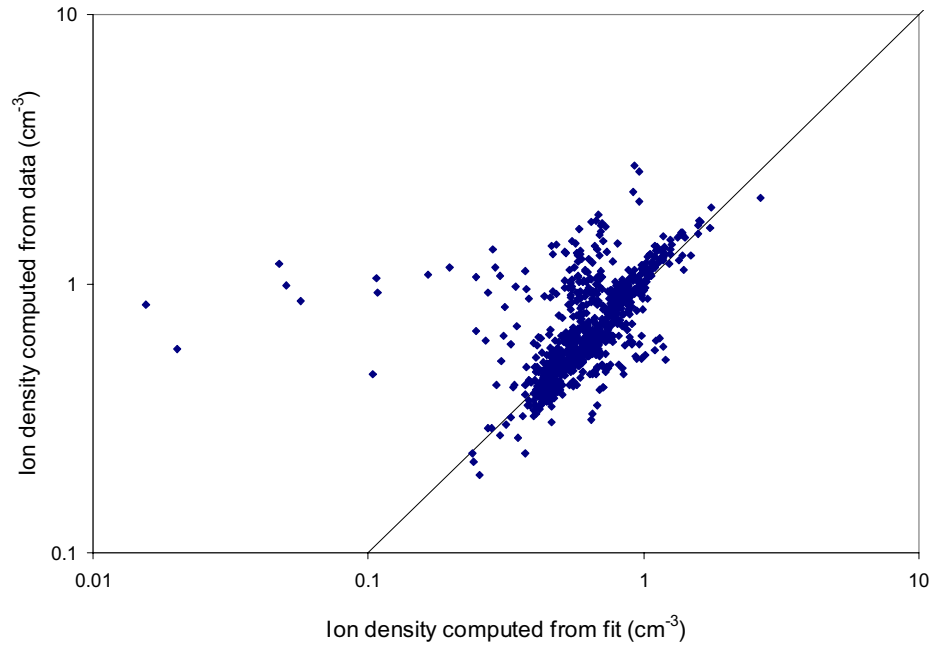


Figure 87. Ion density computed from data compared with ion density computed from fit to Double Maxwellian. Integral over fit extends from 1 eV to 100 keV.

Sept 01; Eclipse; Double Maxwellian fits

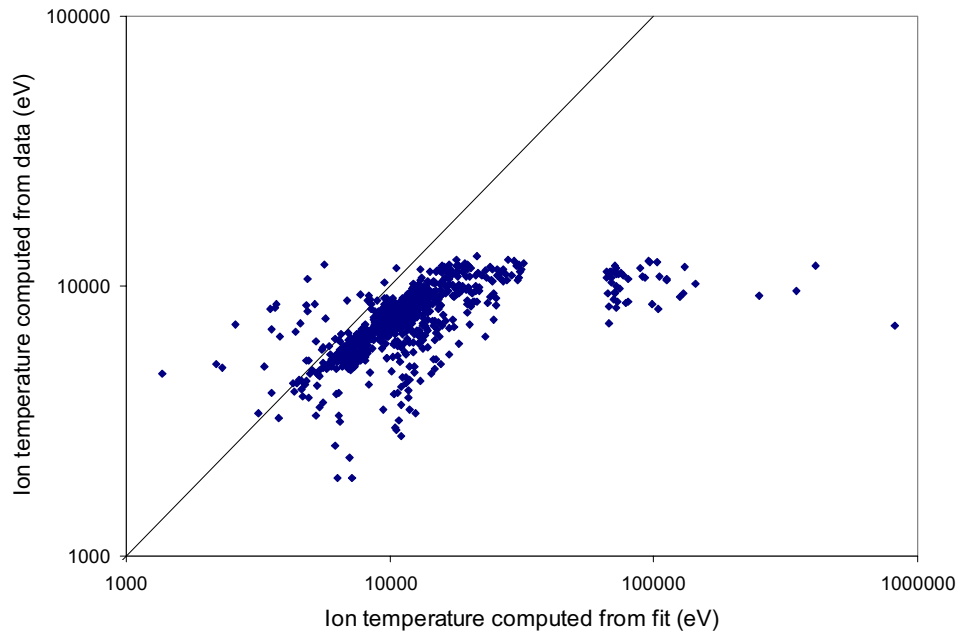


Figure 88. Ion temperature computed from data compared with ion temperature computed from fit to Double Maxwellian. Integral over fit extends from 1 eV to 100 keV.

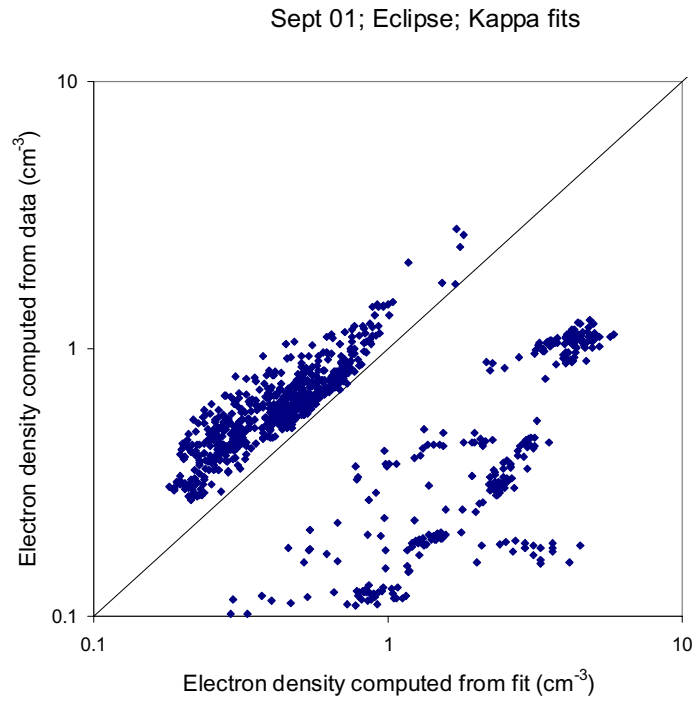


Figure 89. Electron density computed from data compared with electron density computed from fit to Kappa. Integral over fit extends from 1 eV to 100 keV.

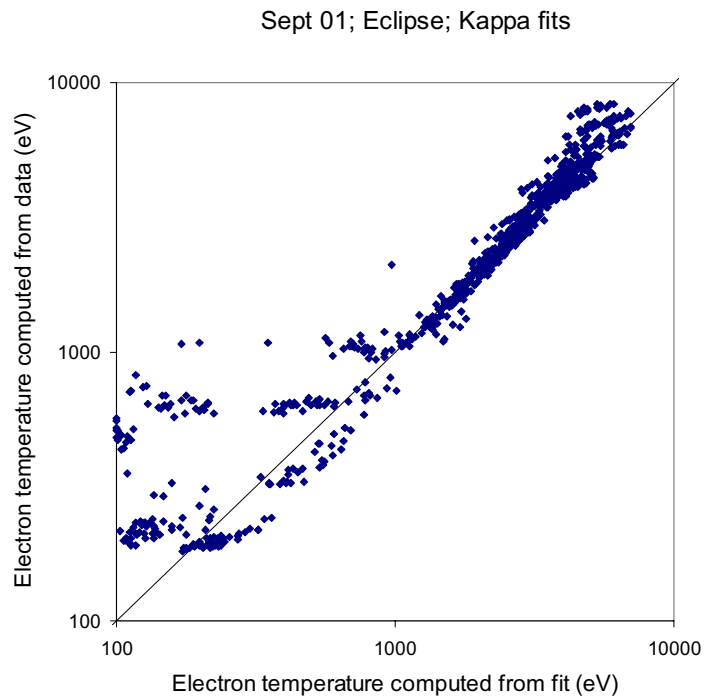


Figure 90. Electron temperature computed from data compared with electron temperature computed from fit to Kappa. Integral over fit extends from 1 eV to 100 keV.

Sept 01; Eclipse; Kappa fits

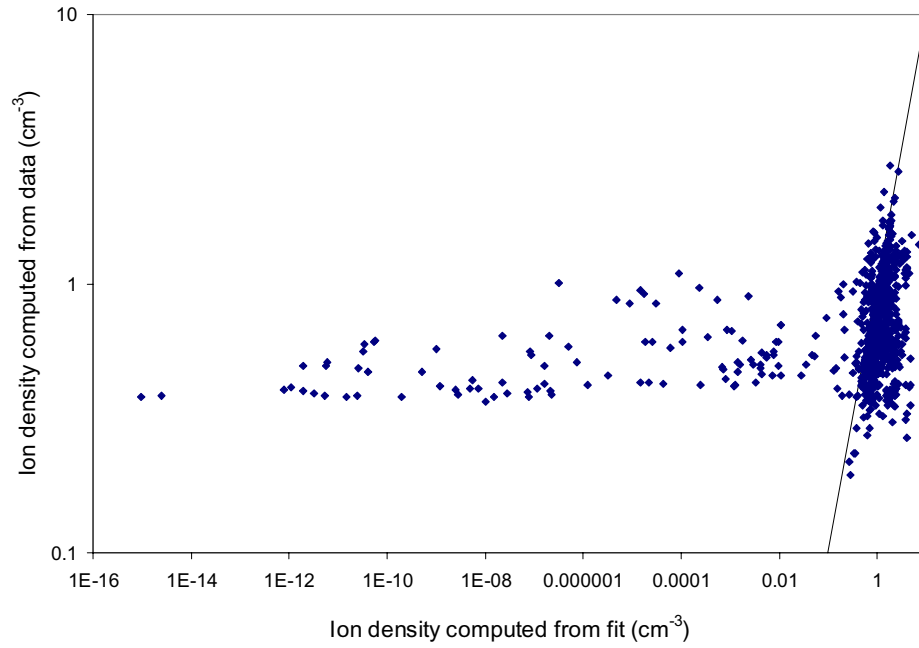


Figure 91. Ion density computed from data compared with ion density computed from fit to Kappa. Integral over fit extends from 1 eV to 100 keV.

Sept 01; Eclipse; Kappa fits

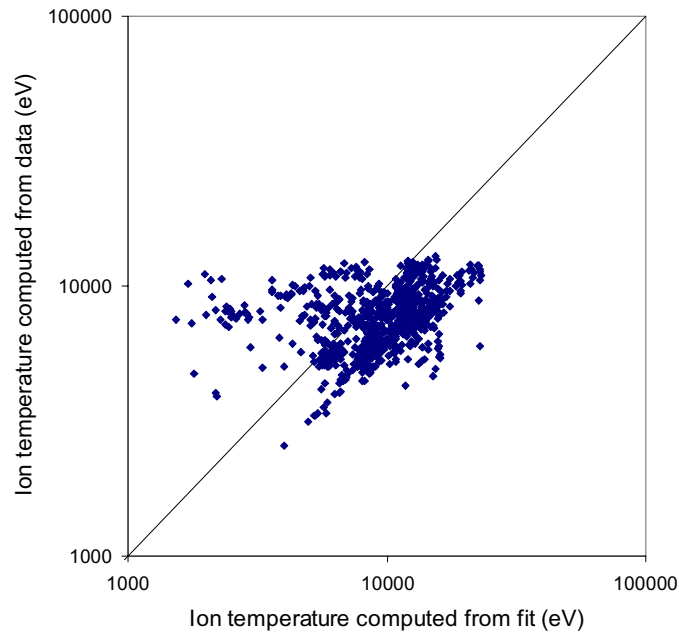


Figure 92. Ion temperature computed from data compared with ion temperature computed from fit to Kappa. Integral over fit extends from 1 eV to 100 keV.

Sept 01; Eclipse; Maxwellian fits

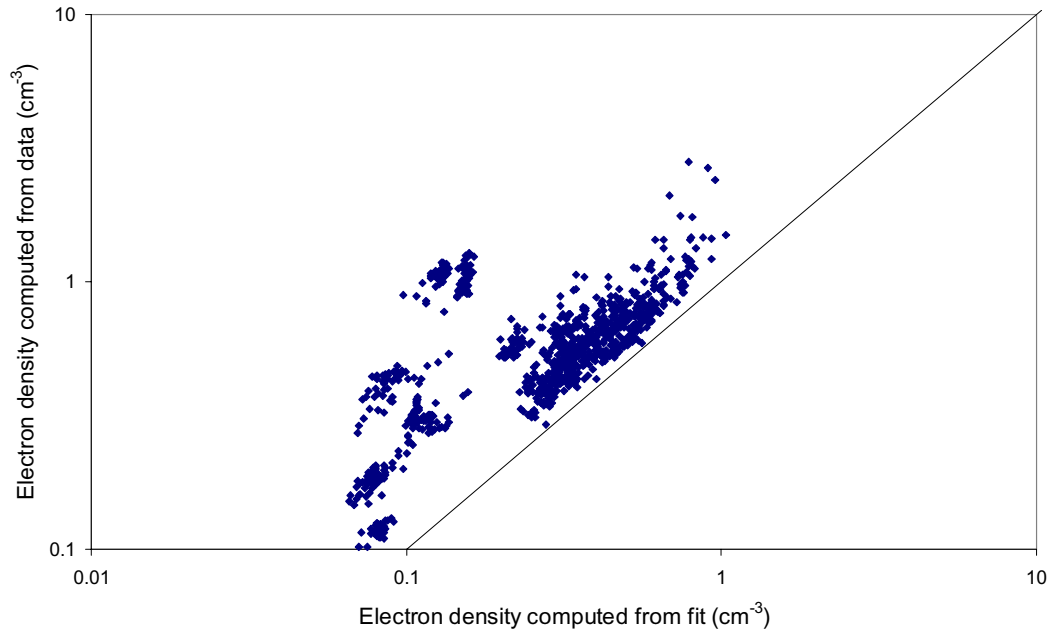


Figure 93. Electron density computed from data compared with electron density computed from fit to Maxwellian. Integral over fit only includes energy bins used to create fit.

Sept 01; Eclipse; Maxwellian fits

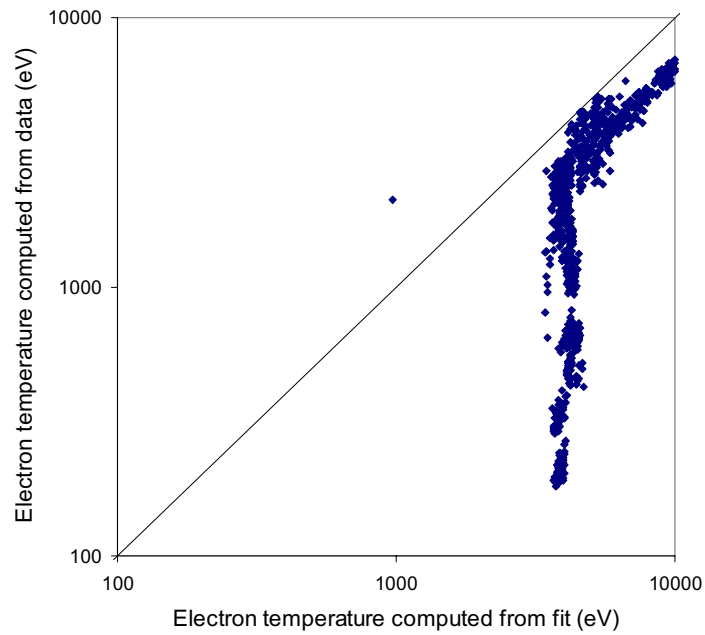


Figure 94. Electron temperature computed from data compared with electron temperature computed from fit to Maxwellian. Integral over fit only includes energy bins used to create fit.

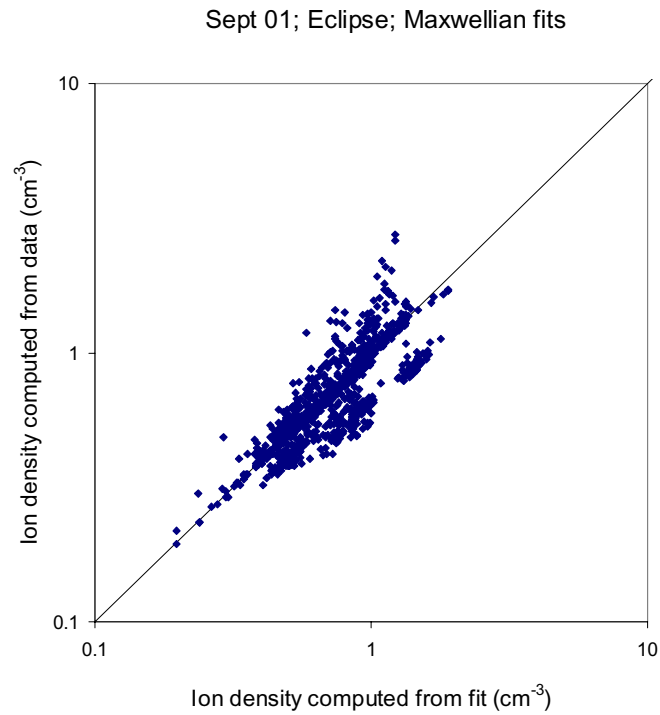


Figure 95. Ion density computed from data compared with ion density computed from fit to Maxwellian. Integral over fit only includes energy bins used to create fit.

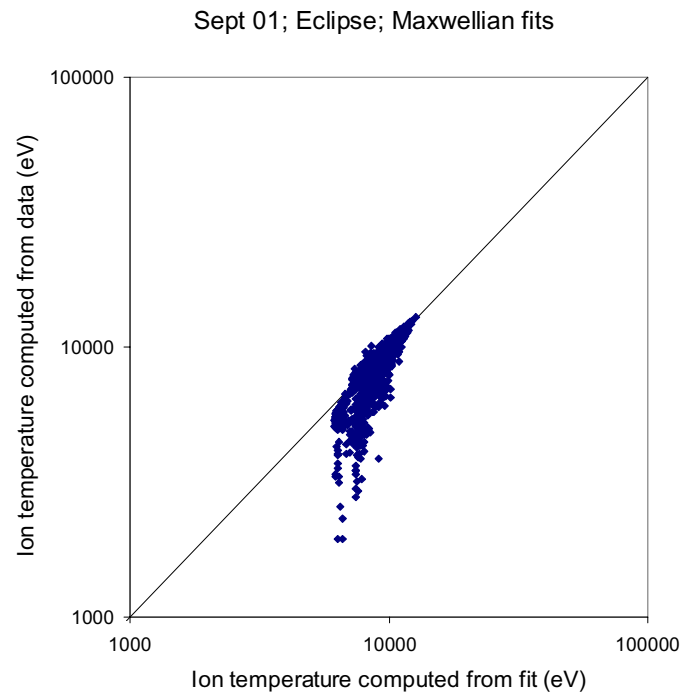


Figure 96. Ion temperature computed from data compared with ion temperature computed from fit to Maxwellian. Integral over fit only includes energy bins used to create fit.

Sept 01; Eclipse; Single Maxwellian fits

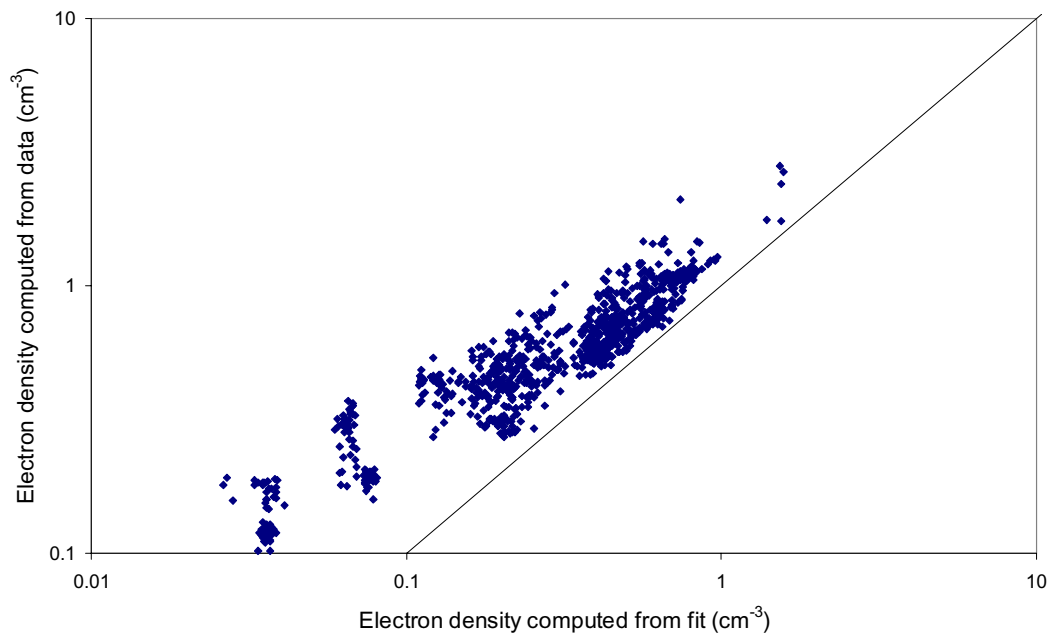


Figure 97. Electron density computed from data compared with electron density computed from fit to Single Maxwellian. Integral over fit only includes energy bins used to create fit.

Sept 01; Eclipse; Single Maxwellian fits

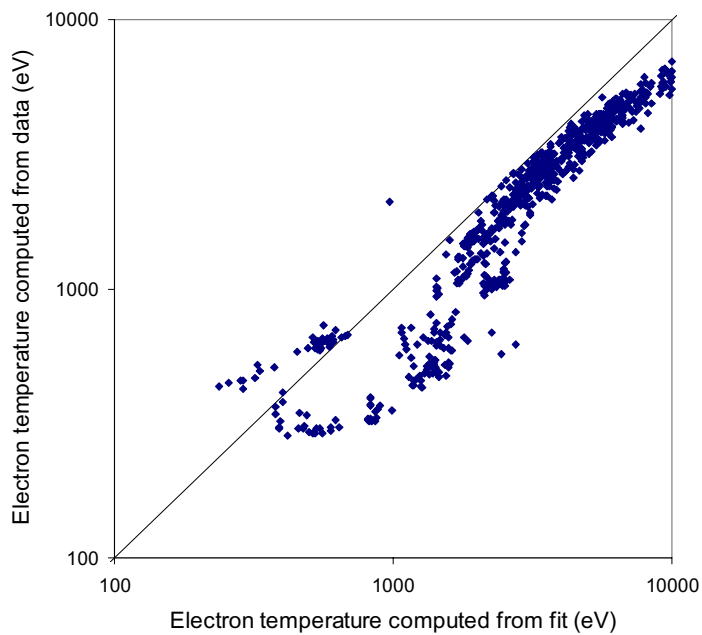


Figure 98. Electron temperature computed from data compared with electron temperature computed from fit to Single Maxwellian. Integral over fit only includes energy bins used to create fit.

Sept 01; Eclipse; Single Maxwellian fits

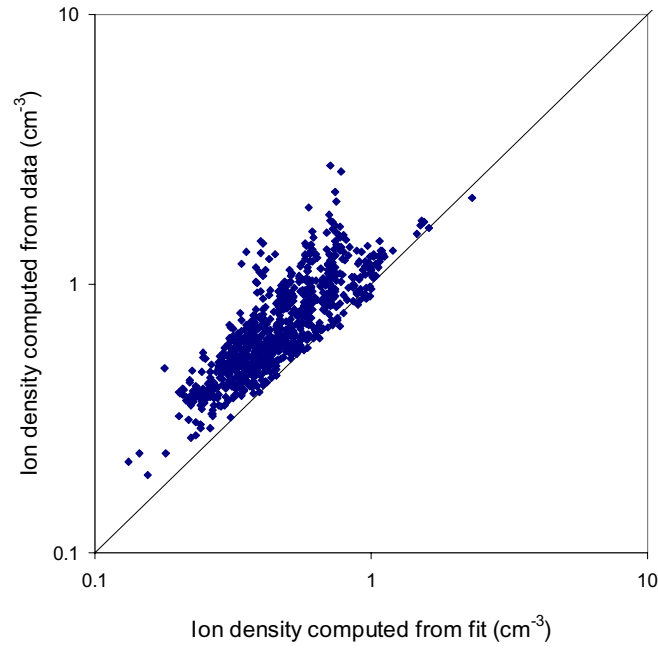


Figure 99. Ion density computed from data compared with ion density computed from fit to Single Maxwellian. Integral over fit only includes energy bins used to create fit.

Sept 01; Eclipse; Single Maxwellian fits

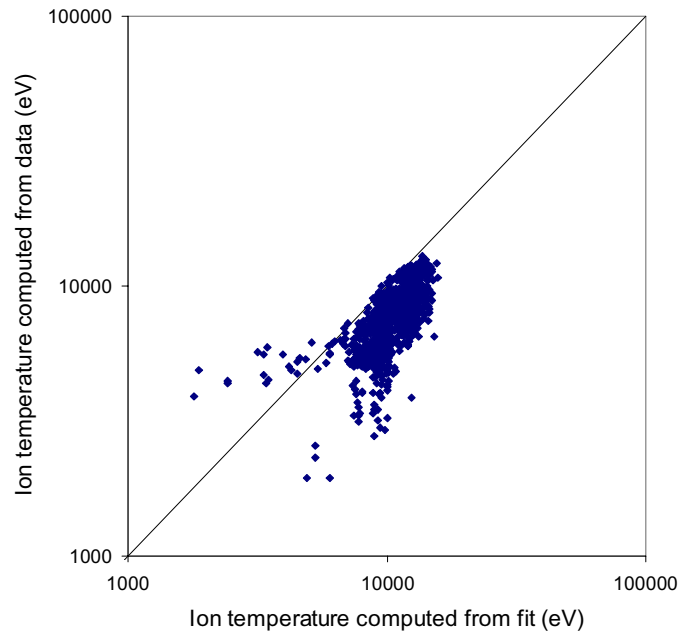


Figure 100. Ion temperature computed from data compared with ion temperature computed from fit to Single Maxwellian. Integral over fit only includes energy bins used to create fit.

Sept 01; Eclipse; Double Maxwellian fits

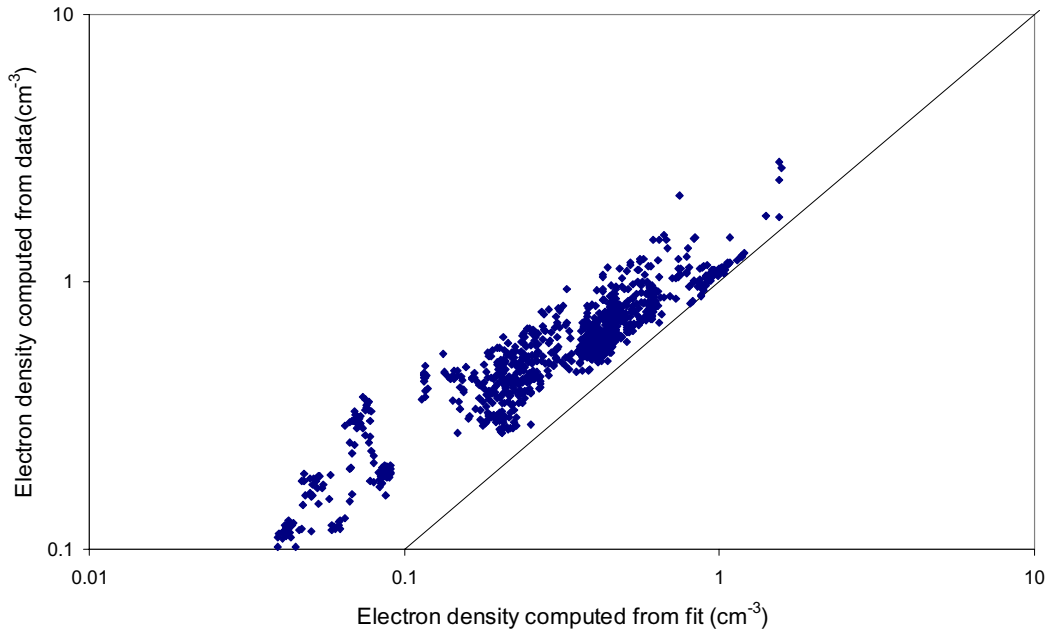


Figure 101. Electron density computed from data compared with electron density computed from fit to Double Maxwellian. Integral over fit only includes energy bins used to create fit.

Sept 01; Eclipse; Double Maxwellian fits

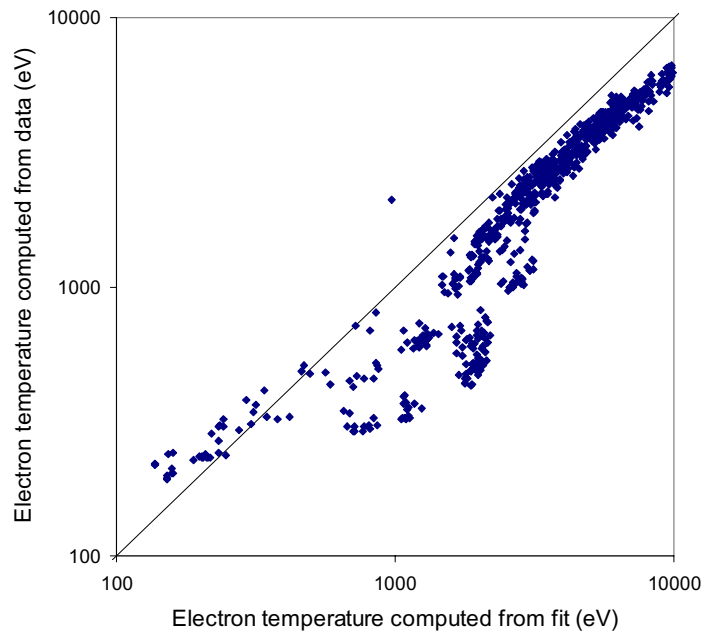


Figure 102. Electron temperature computed from data compared with electron temperature computed from fit to Double Maxwellian. Integral over fit only includes energy bins used to create fit.

Sept 01; Eclipse; Double Maxwellian fits

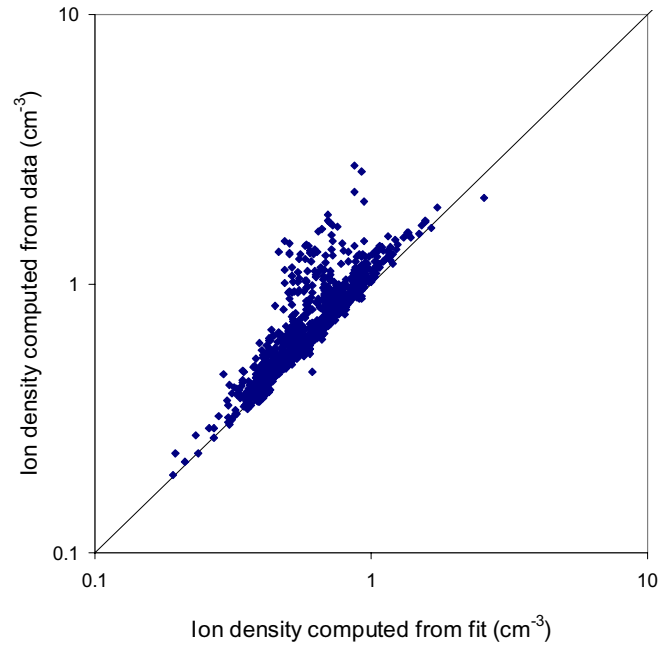


Figure 103. Ion density computed from data compared with ion density computed from fit to Double Maxwellian. Integral over fit only includes energy bins used to create fit.

Sept 01; Eclipse; Double Maxwellian fits

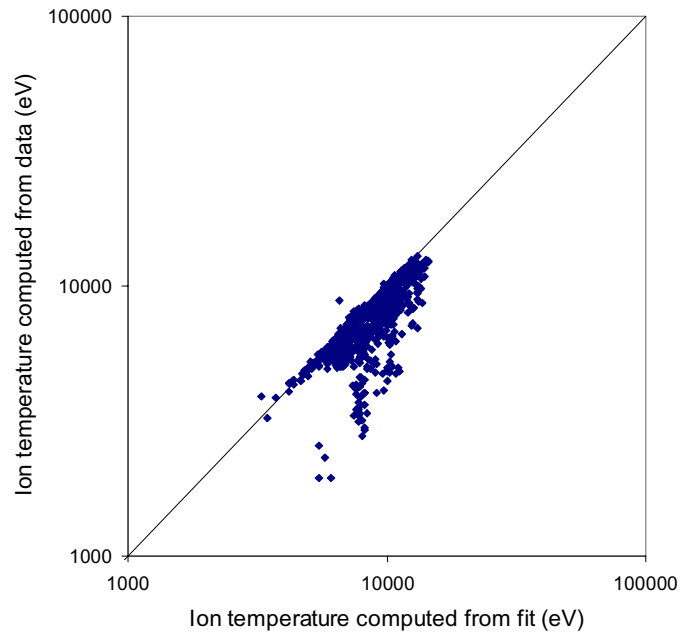


Figure 104. Ion temperature computed from data compared with ion temperature computed from fit to Double Maxwellian. Integral over fit only includes energy bins used to create fit.

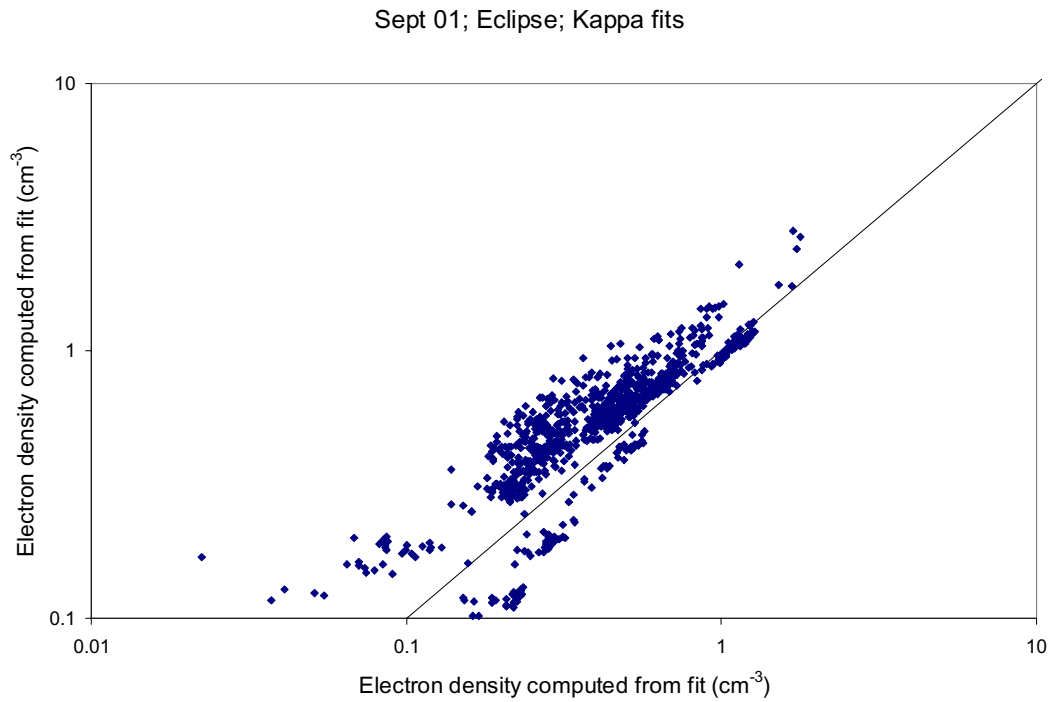


Figure 105. Electron density computed from data compared with electron density computed from fit to Kappa. Integral over fit only includes energy bins used to create fit.

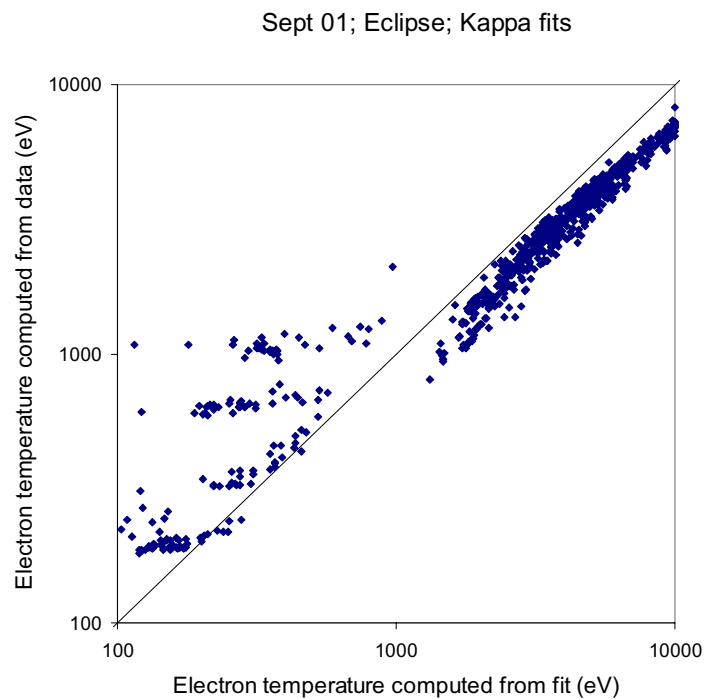


Figure 106. Electron temperature computed from data compared with electron temperature computed from fit to Kappa. Integral over fit only includes energy bins used to create fit.

Sept 01; Eclipse; Kappa fits

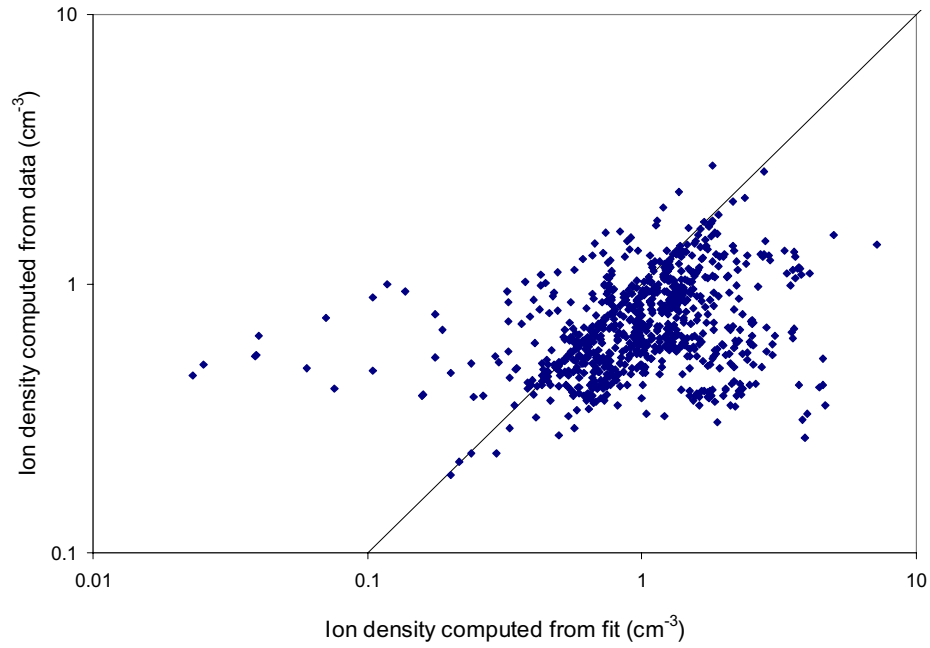


Figure 107. Ion density computed from data compared with ion density computed from fit to Kappa. Integral over fit only includes energy bins used to create fit.

Sept 01; Eclipse; Kappa fits

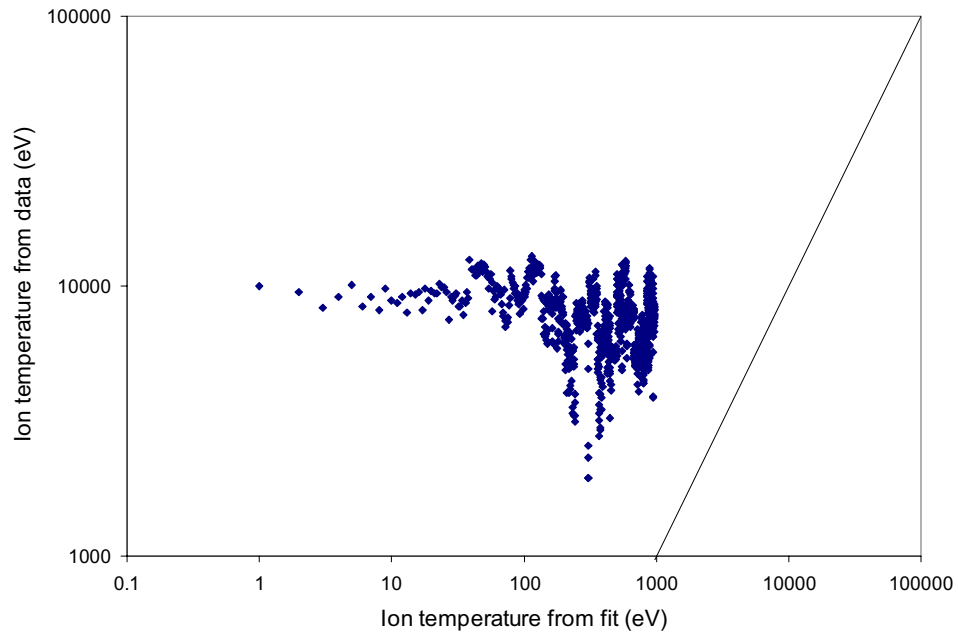


Figure 108. Ion temperature computed from data compared with ion temperature computed from fit to Kappa. Integral over fit only includes energy bins used to create fit.

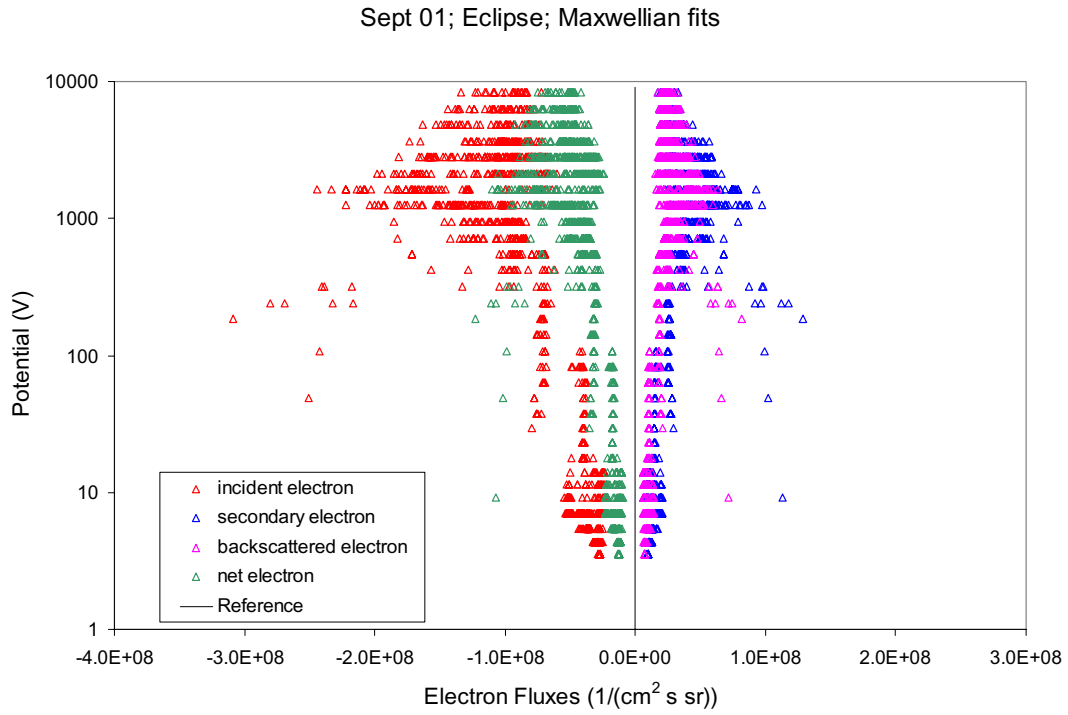


Figure 109. Electron fluxes in eclipse computed from Maxwellian fit at all potentials. Integral extends from 1 eV to 100 keV.

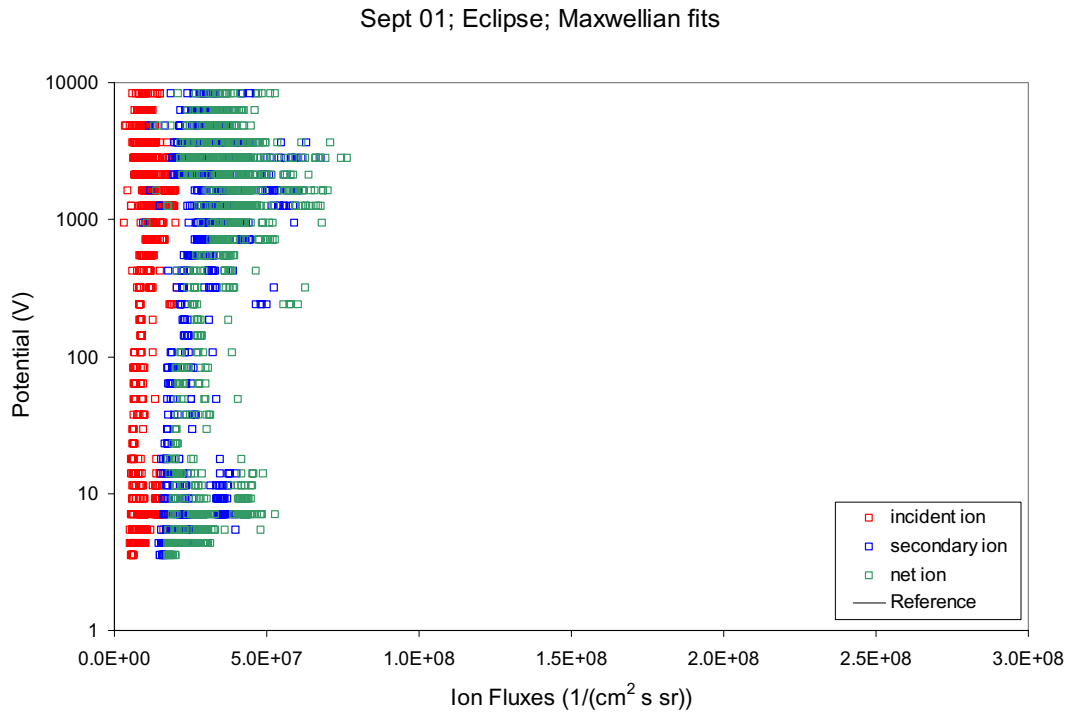


Figure 110. Ion fluxes in eclipse computed from Maxwellian fit at all potentials. Integral extends from 1 eV to 100 keV.

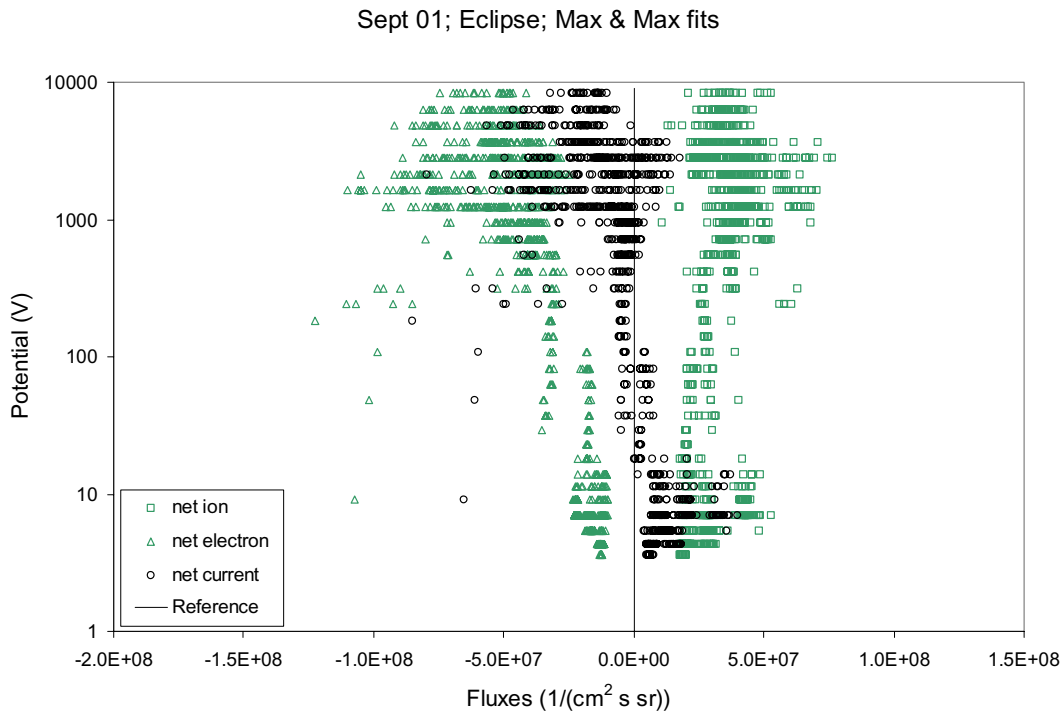


Figure 111. Net flux in eclipse computed from Maxwellian fit at all potentials. Integral extends from 1 eV to 100 keV.

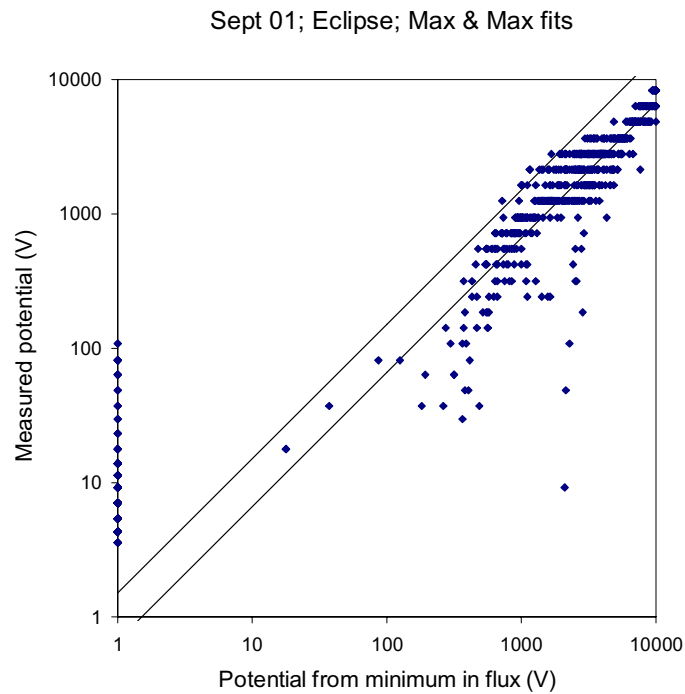


Figure 112. Measured potential as a function of the potential computed from the minimum in the net flux, where the fluxes are computed from Maxwellian fits to the electron and ion fluxes.

Sept 01; Eclipse; Single Maxwellian fits

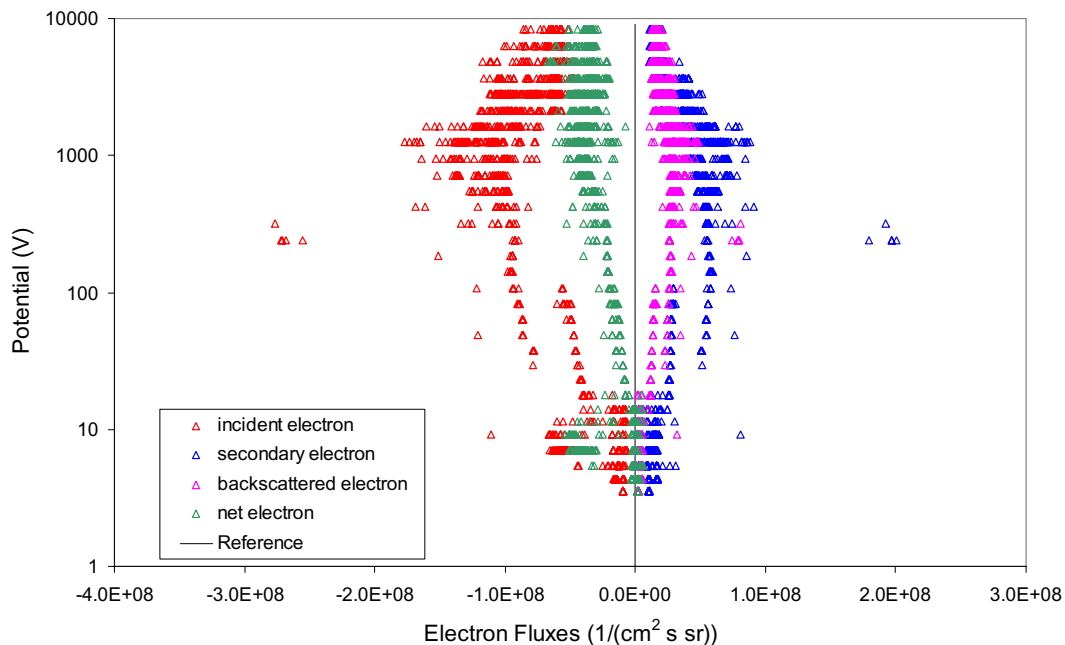


Figure 113. Electron fluxes in eclipse computed from Single Maxwellian fit at all potentials. Integral extends from 1 eV to 100 keV.

Sept 01; Eclipse; Single Maxwellian fits

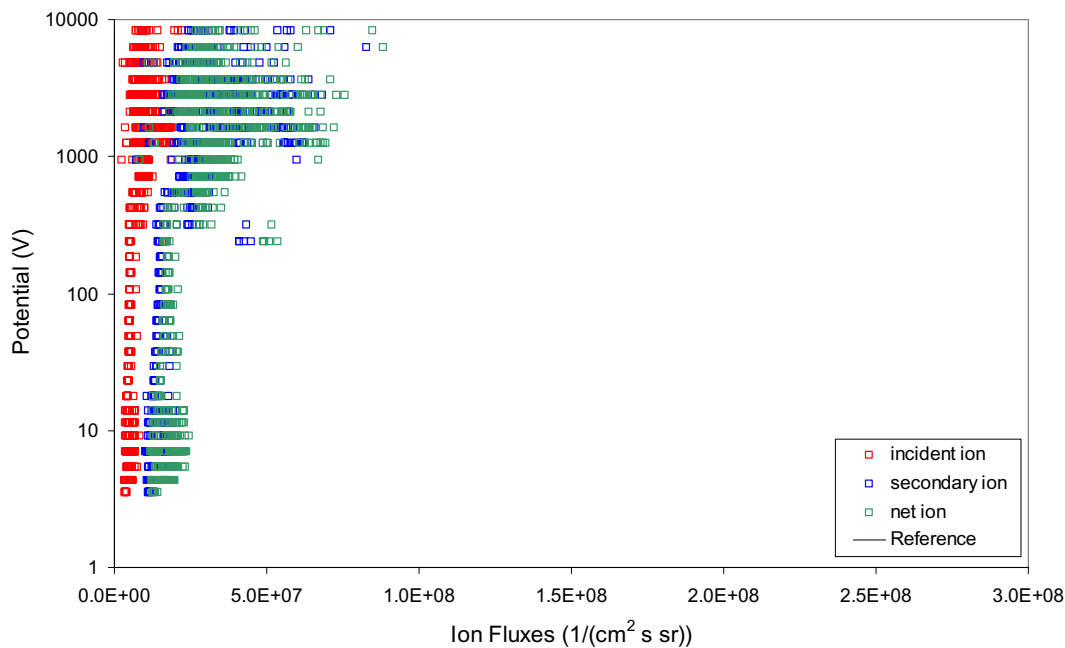


Figure 114. Ion fluxes in eclipse computed from Single Maxwellian fit at all potentials. Integral extends from 1 eV to 100 keV.

Sept 01; Eclipse; Single Max & Single Max fits

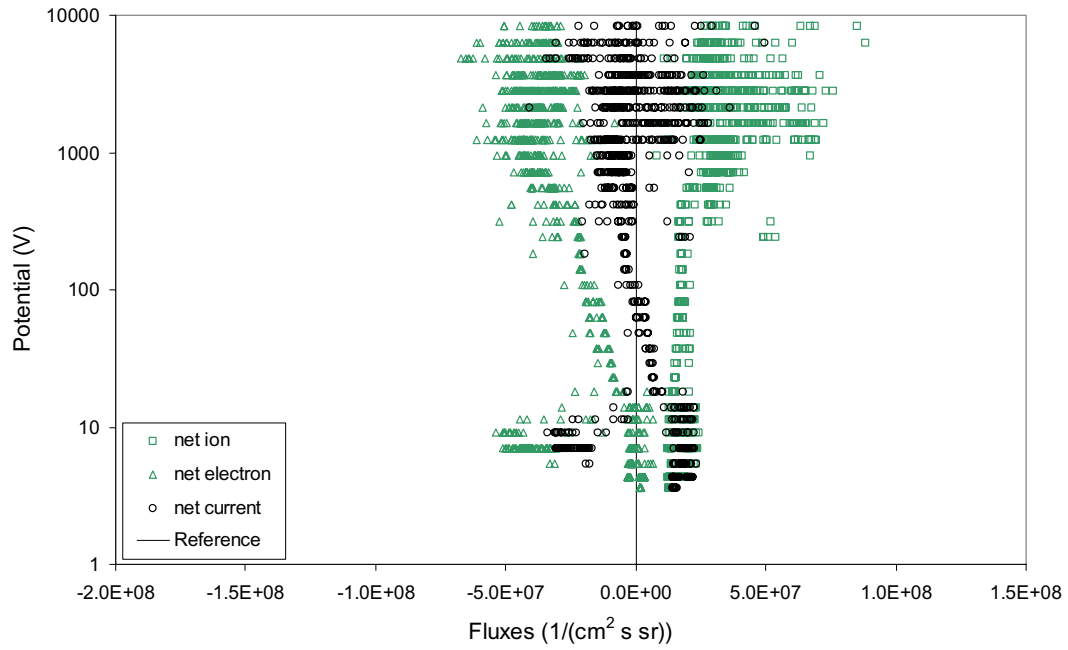
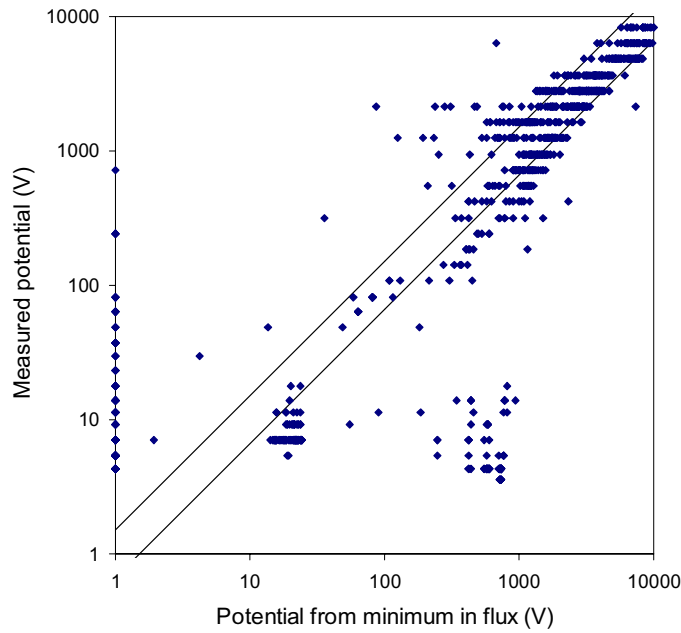


Figure 115. Net fluxes in eclipse computed from Single Maxwellian fit at all potentials. Integral extends from 1 eV to 100 keV.

Sept 01; Eclipse; Single Max & Single Max fits



Sept 01; Eclipse; Single Max & Sin

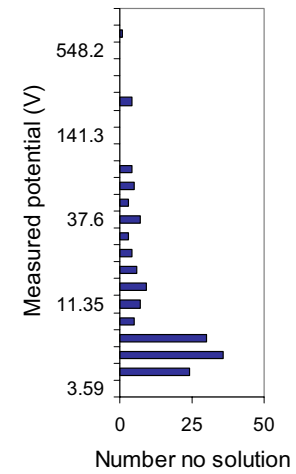


Figure 116. Measured potential as a function of the potential computed from the minimum in the net flux, where the fluxes are computed from Single Maxwellian fits to the electron and ion fluxes.

Sept 01; Eclipse; Double Maxwellian fits

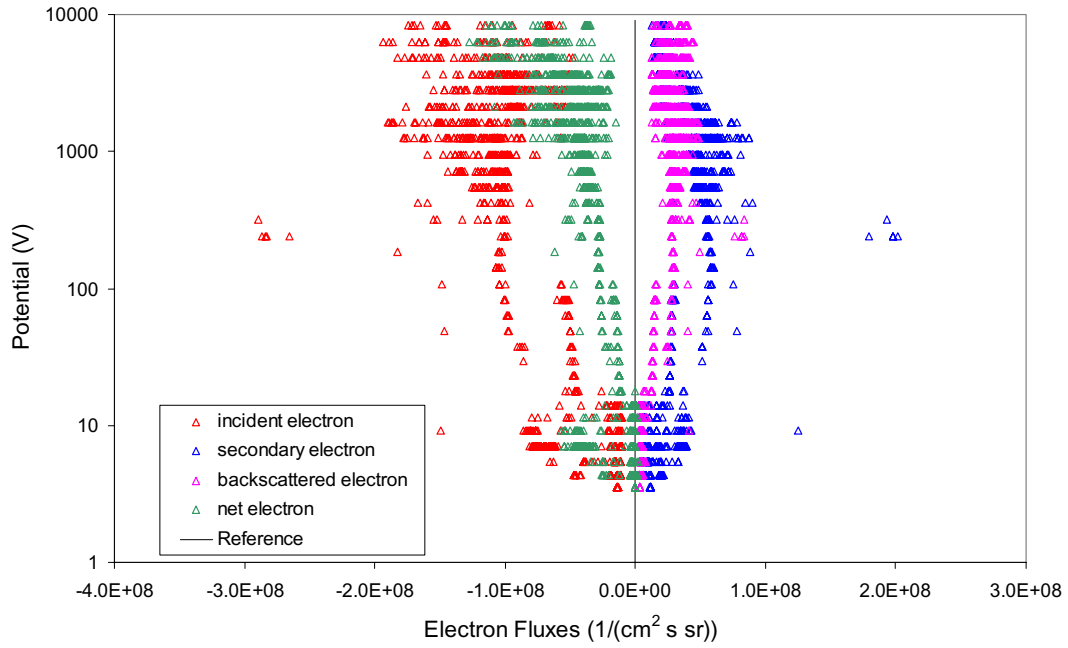


Figure 117. Electron fluxes in eclipse computed from Double Maxwellian fit at all potentials. Integral extends from 1 eV to 100 keV.

Sept 01; Eclipse; Double Maxwellian fits

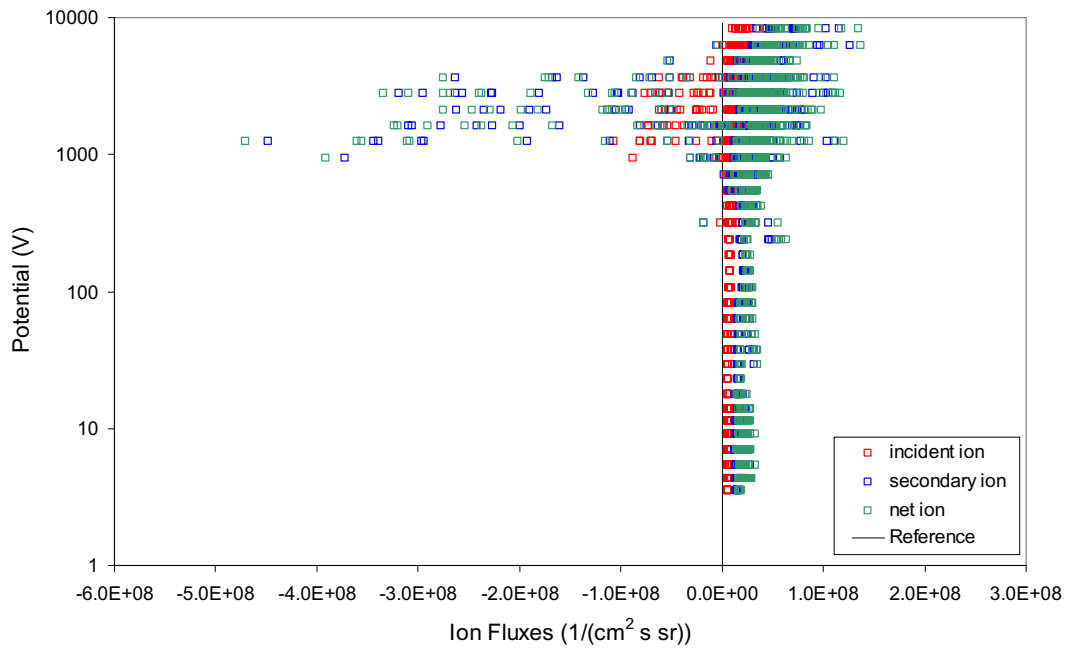


Figure 118. Ion fluxes in eclipse computed from Double Maxwellian fit at all potentials. Integral extends from 1 eV to 100 keV.

Sept 01; Eclipse; Double Max & Double Max fits

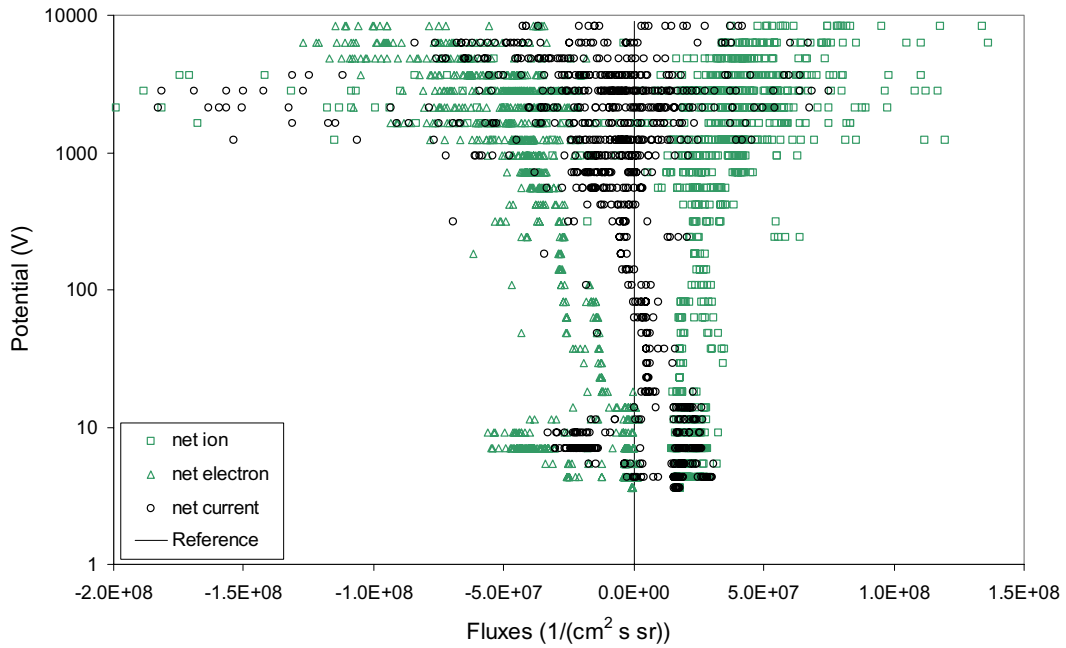
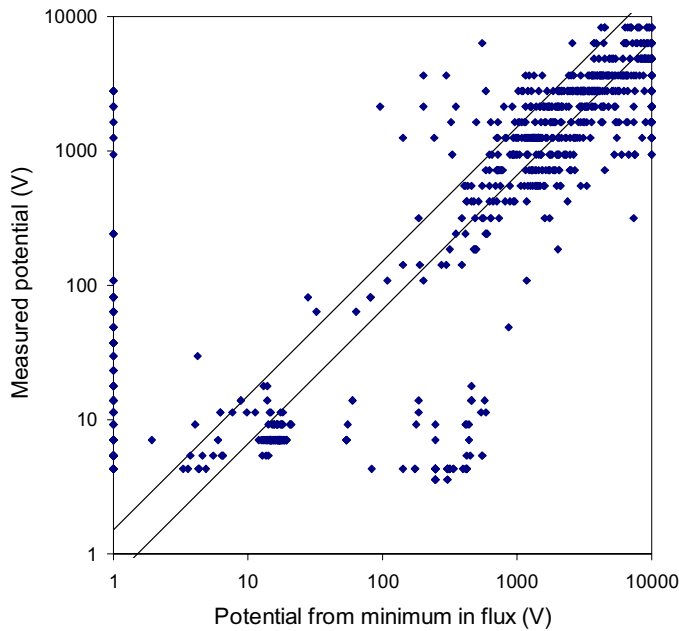


Figure 119. Net fluxes in eclipse computed from Double Maxwellian fit at all potentials. Integral extends from 1 eV to 100 keV.

Sept 01; Eclipse; Double Max & Double Max fits



Sept 01; Eclipse; Double Max & Double Max fits

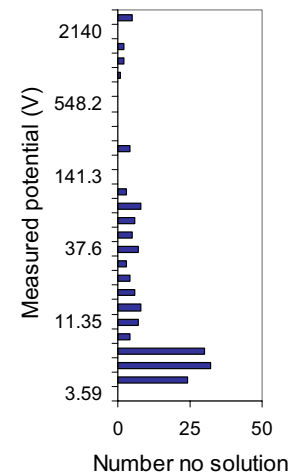


Figure 120. Measured potential as a function of the potential computed from the minimum in the net flux, where the fluxes are computed from Double Maxwellian fits to the electron and ion fluxes.

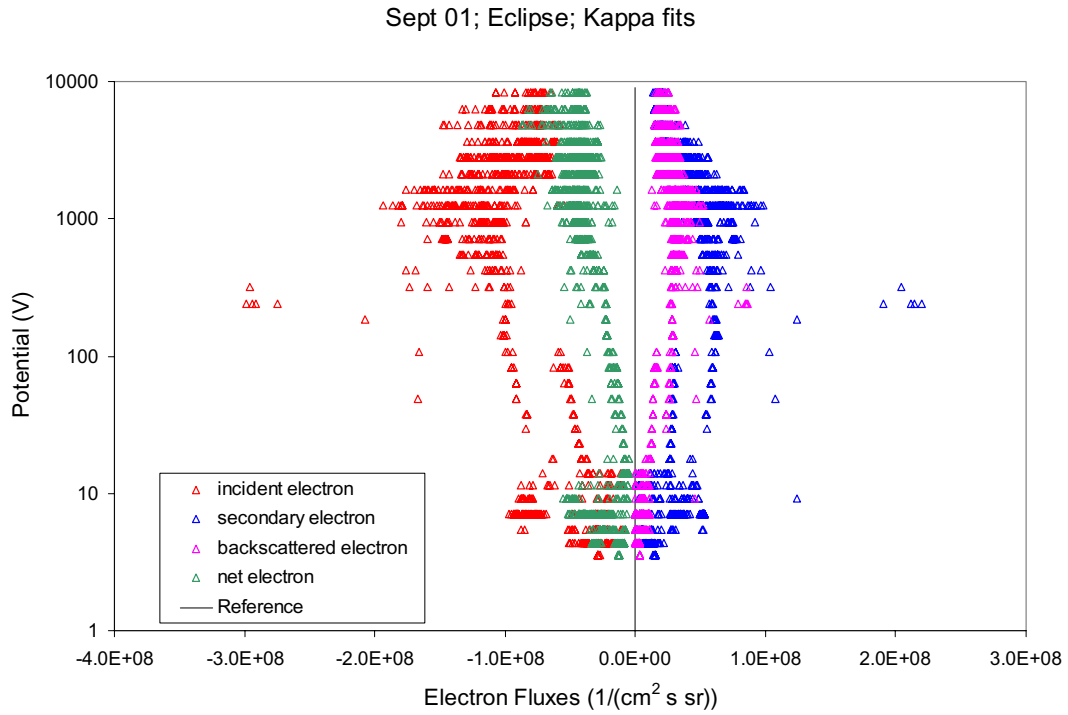


Figure 121. Electron fluxes in eclipse computed from Kappa fit at all potentials. Integral extends from 1 eV to 100 keV.

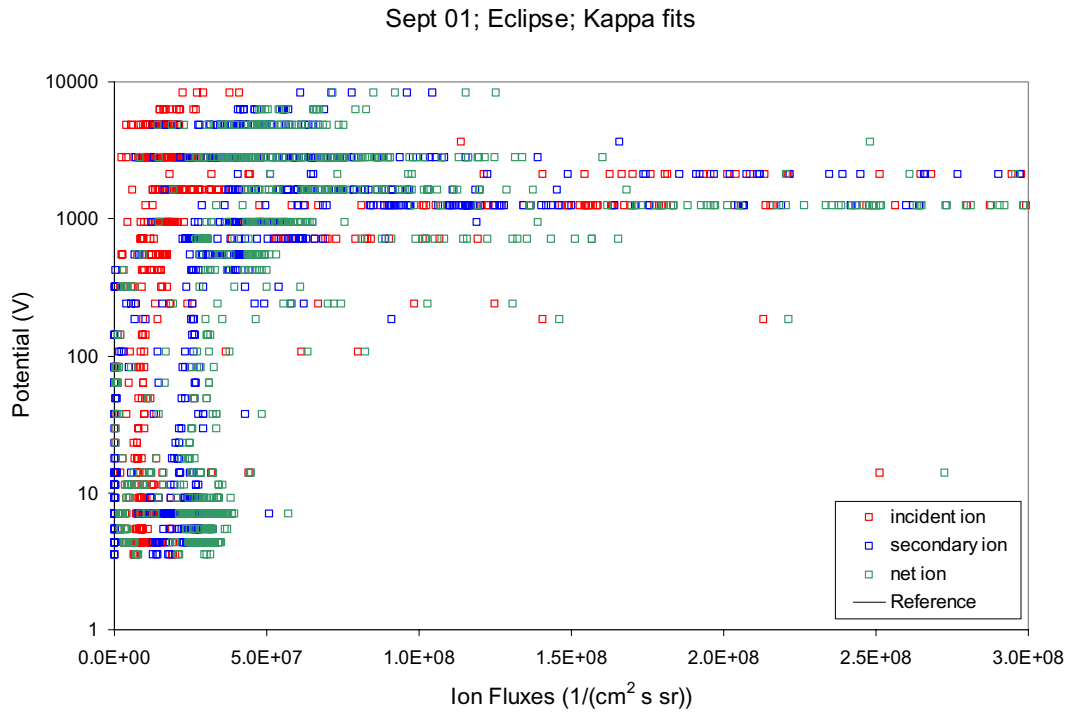


Figure 122. Ion fluxes in eclipse computed from Kappa fit at all potentials. Integral extends from 1 eV to 100 keV.

Sept 01; Eclipse; Kappa & Kappa fits

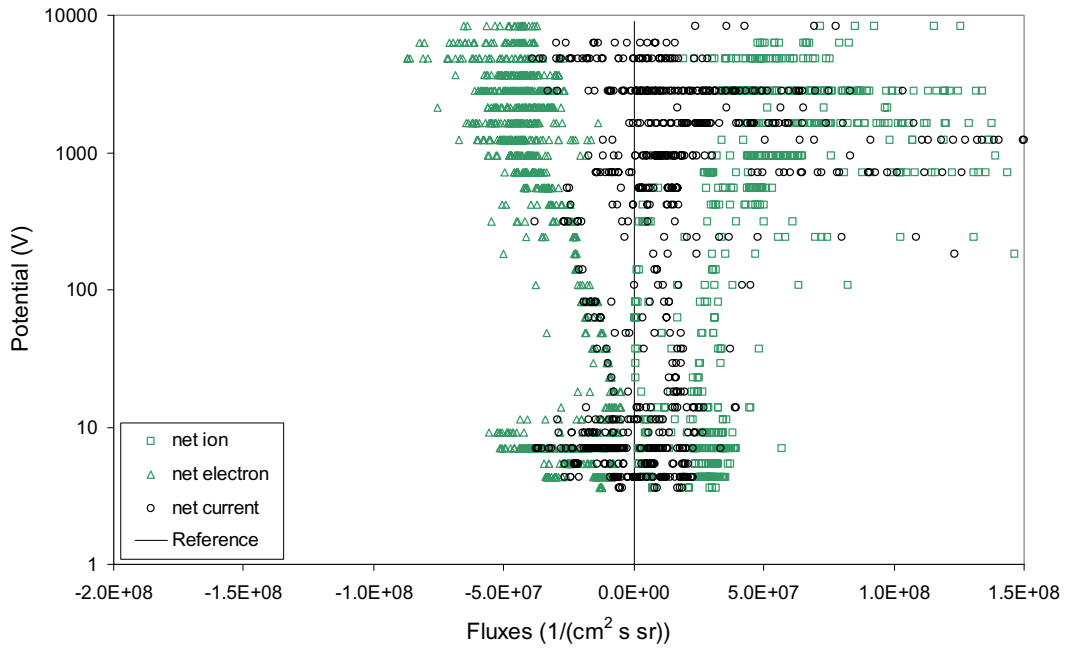
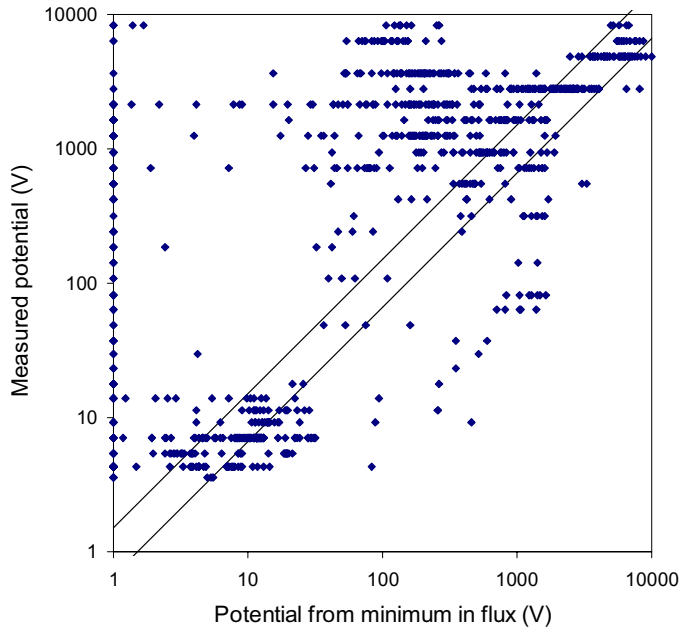


Figure 123. Net fluxes in eclipse computed from Kappa fits at all potentials. Integral extends from 1 eV to 100 keV.

Sept 01; Eclipse; Kappa & Kappa fits



Sept 01; Eclipse; Kappa & Kappa f

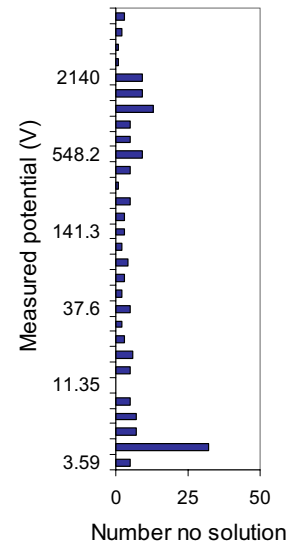


Figure 124. Measured potential as a function of the potential computed from the minimum in the net flux, where the fluxes are computed from Kappa fits to the electron and ion fluxes.

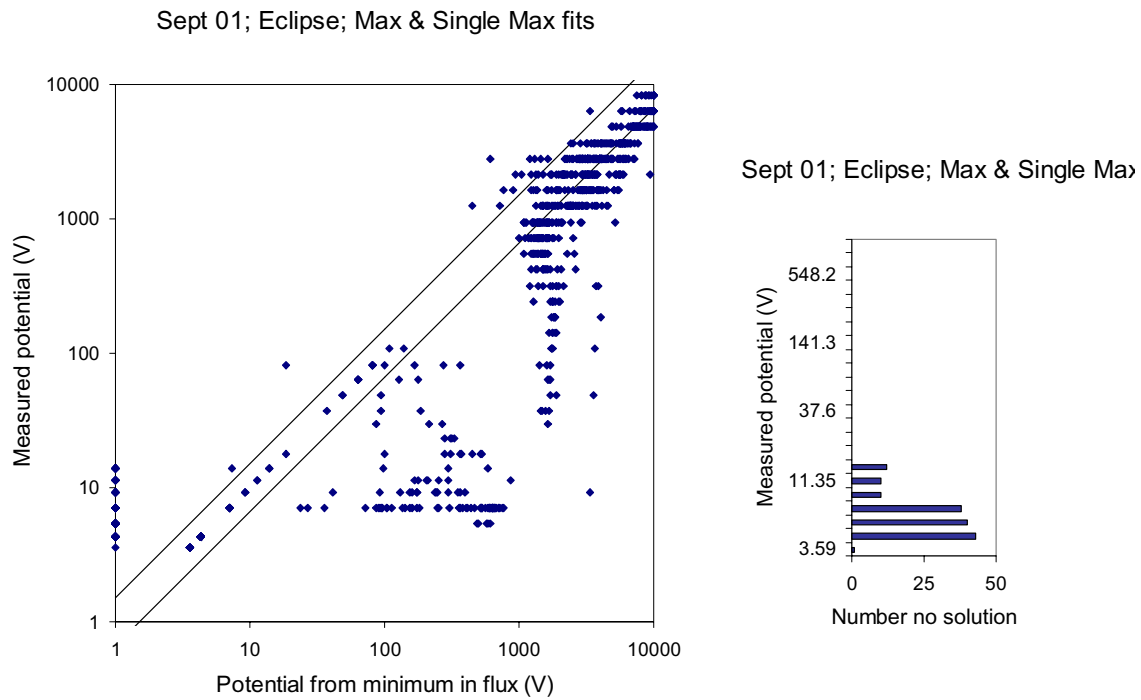


Figure 125. Measured potential computed from the minimum in the net flux, where the fluxes are computed from a Maxwellian fit to the electron flux and a Single Maxwellian fit to the ion flux.

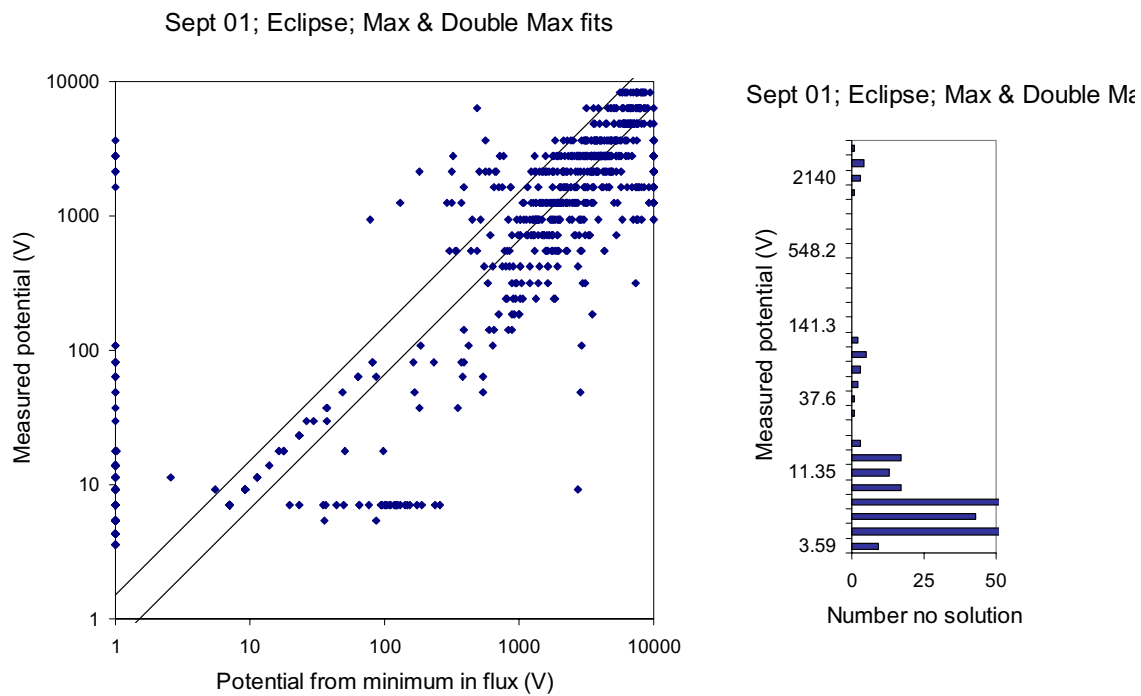


Figure 126. Measured potential computed from the minimum in the net flux, where the fluxes are computed from a Maxwellian fit to the electron flux and a Double Maxwellian fit to the ion flux.

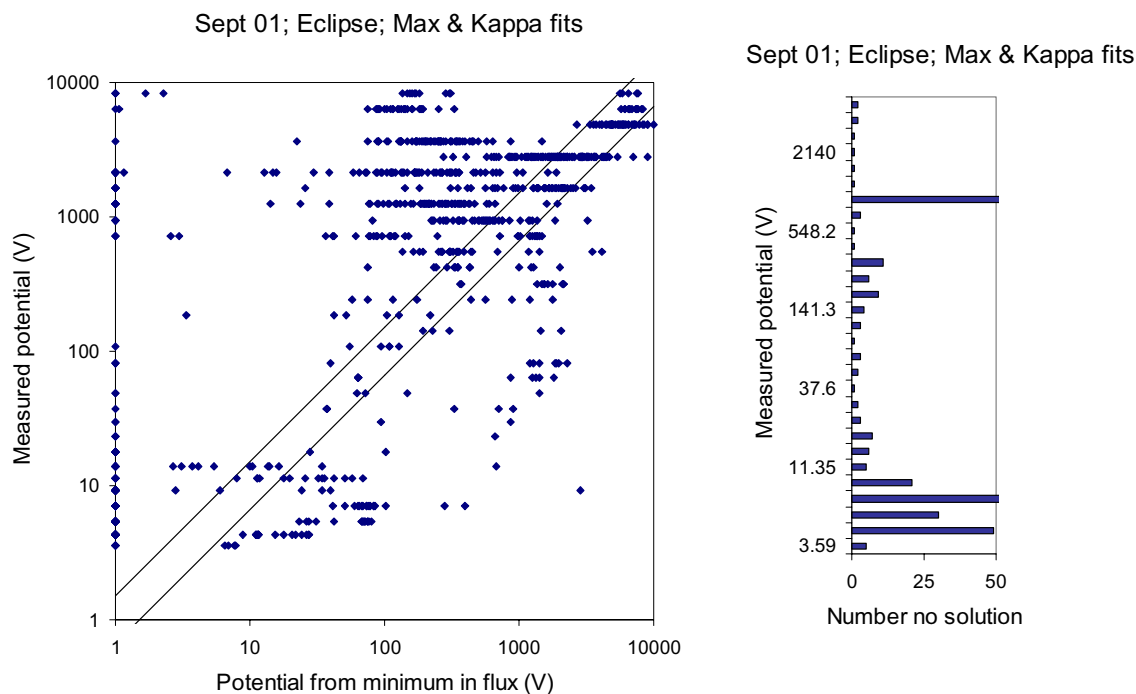


Figure 127. Measured potential computed from the minimum in the net flux, where the fluxes are computed from a Maxwellian fit to the electron flux and a Kappa fit to the ion flux.

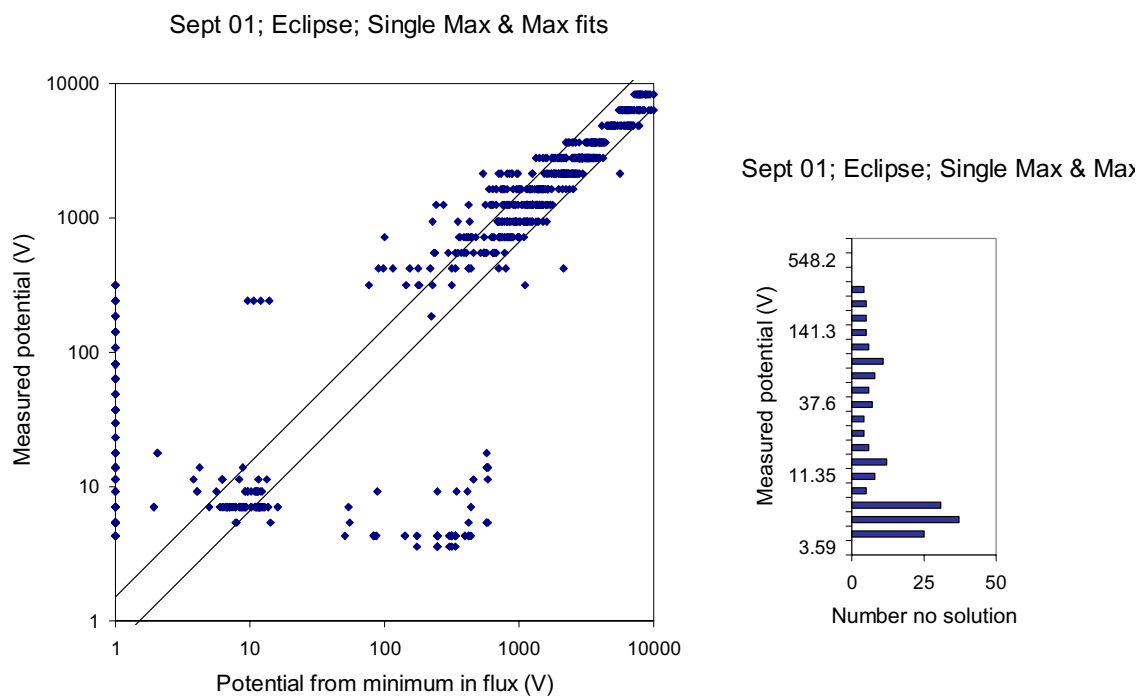


Figure 128. Measured potential computed from the minimum in the net flux, where the fluxes are computed from a Single Maxwellian fit to the electron flux and a Maxwellian fit to the ion flux.

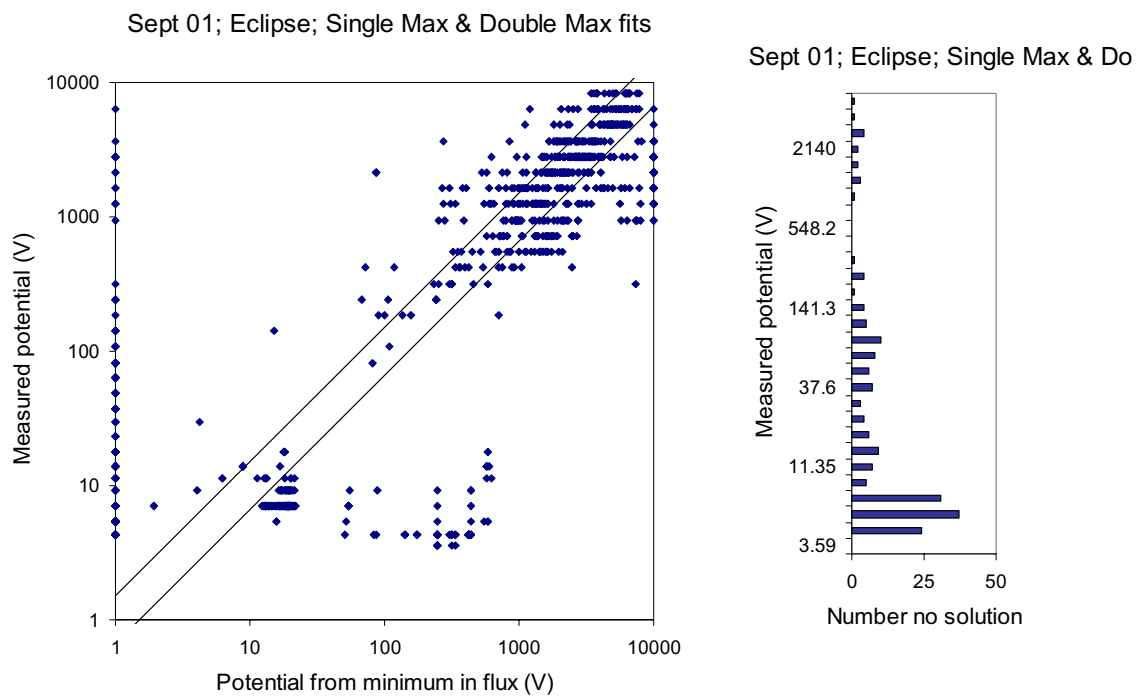


Figure 129. Measured potential computed from the minimum in the net flux, where the fluxes are computed from a Single Maxwellian fit to the electron flux and a Double Maxwellian fit to the ion flux.

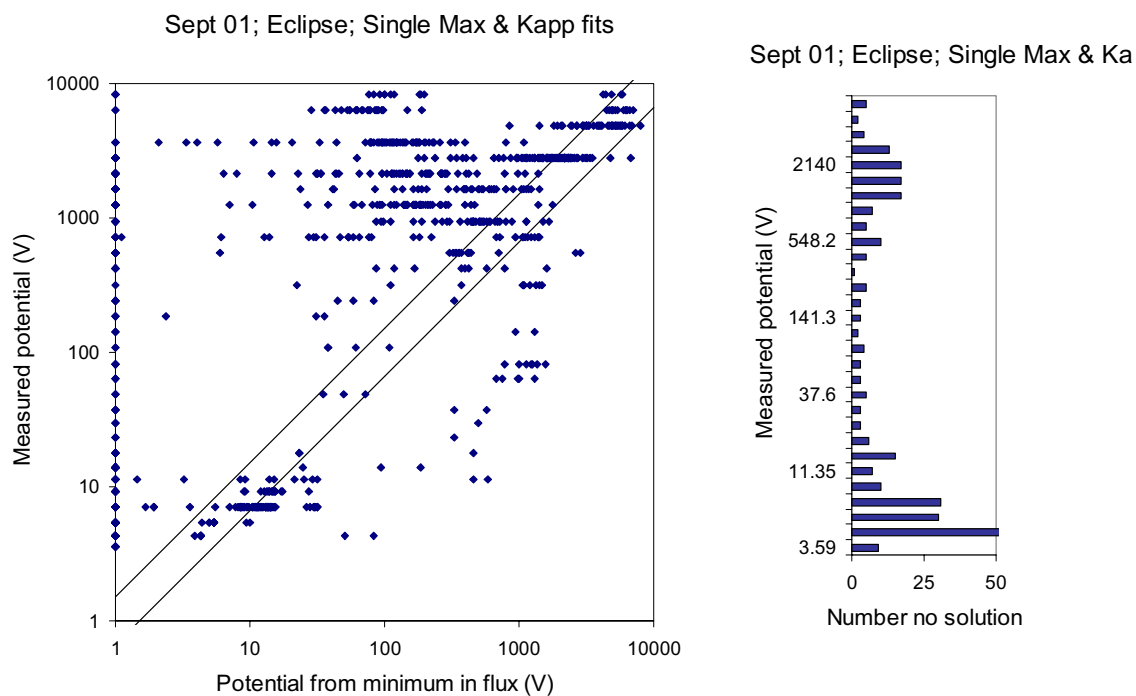


Figure 130. Measured potential computed from the minimum in the net flux, where the fluxes are computed from a Single Maxwellian fit to the electron flux and a Kappa fit to the ion flux.

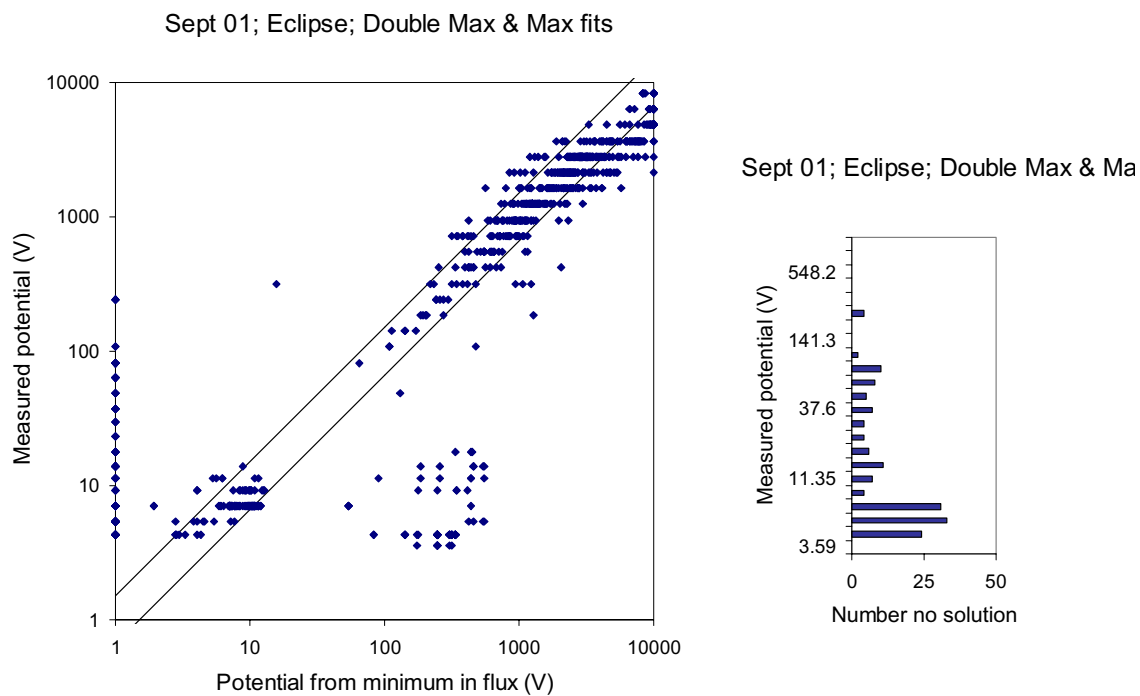


Figure 131. Measured potential computed from the minimum in the net flux, where the fluxes are computed from a Double Maxwellian fit to the electron flux and a Maxwellian fit to the ion flux.

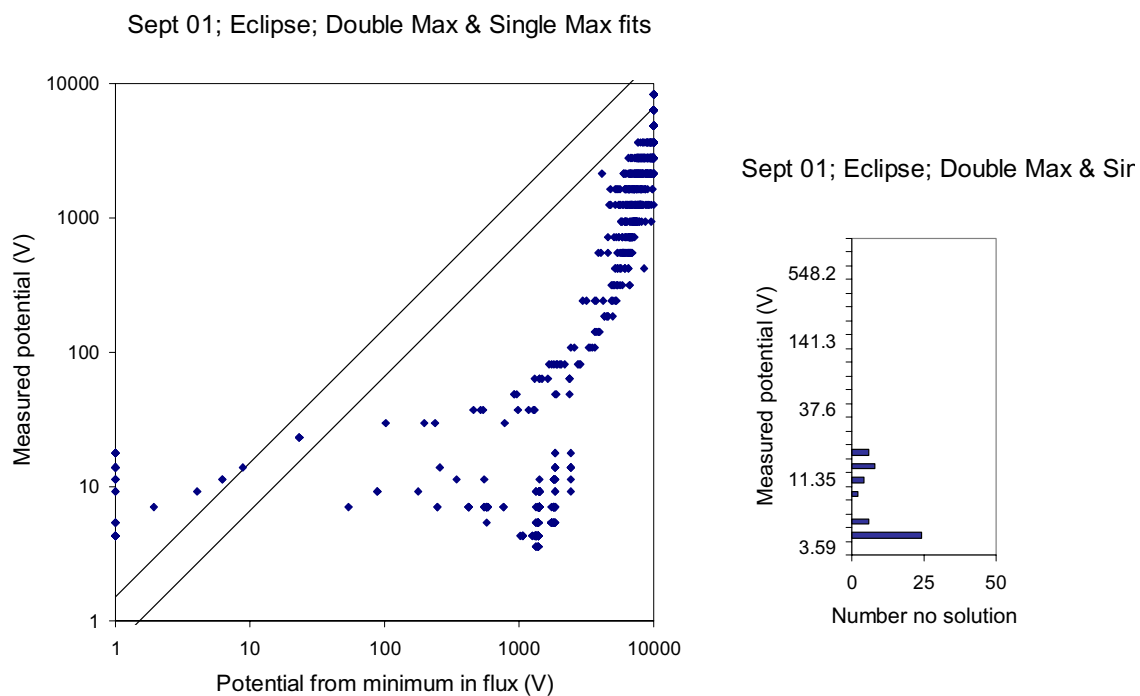


Figure 132. Measured potential computed from the minimum in the net flux, where the fluxes are computed from a Double Maxwellian fit to the electron flux and a Single Maxwellian fit to the ion flux.

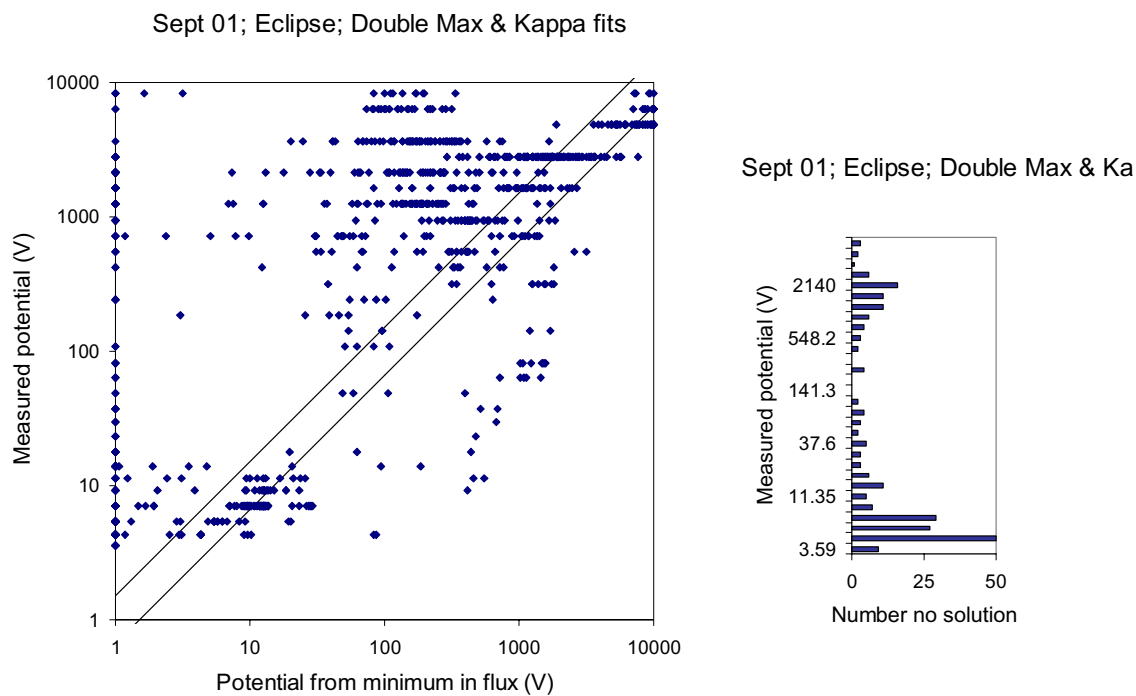


Figure 133. Measured potential computed from the minimum in the net flux, where the fluxes are computed from a Double Maxwellian fit to the electron flux and a Kappa fit to the ion flux.

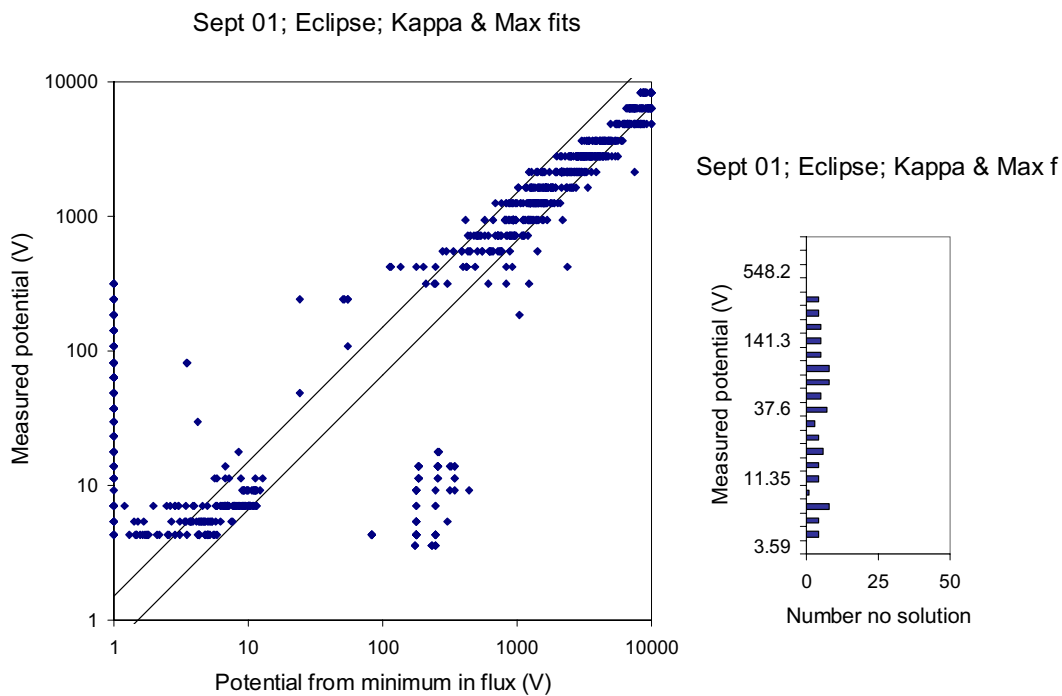


Figure 134. Measured potential computed from the minimum in the net flux, where the fluxes are computed from a Kappa fit to the electron flux and a Maxwellian fit to the ion flux.

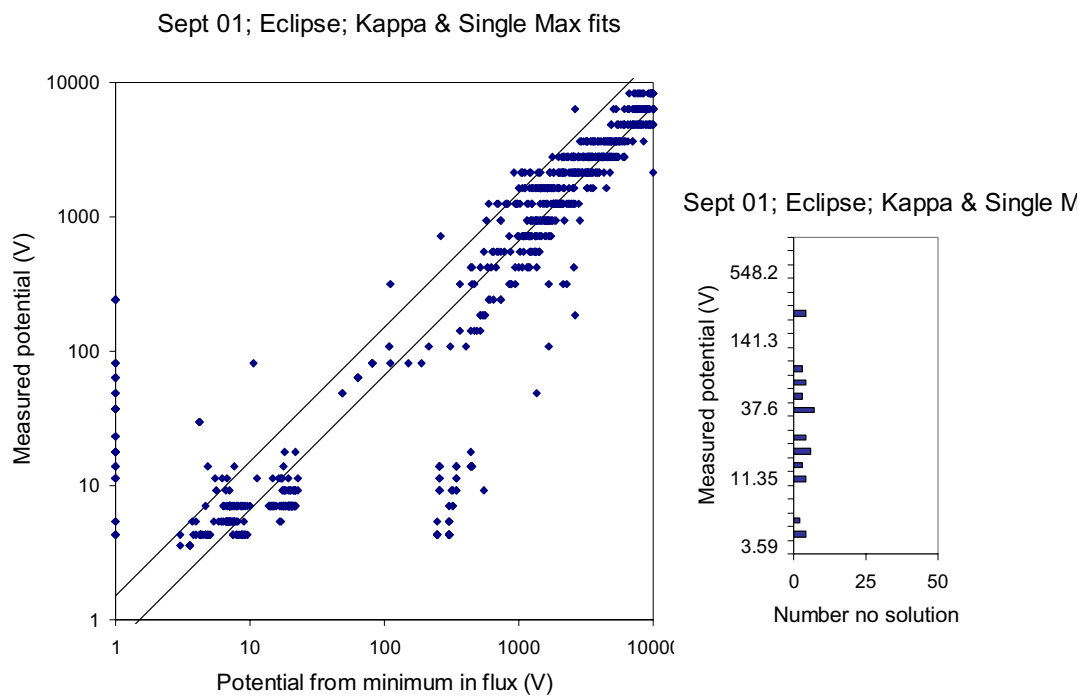


Figure 135. Measured potential computed from the minimum in the net flux, where the fluxes are computed from a Kappa fit to the electron flux and a Single Maxwellian fit to the ion flux.

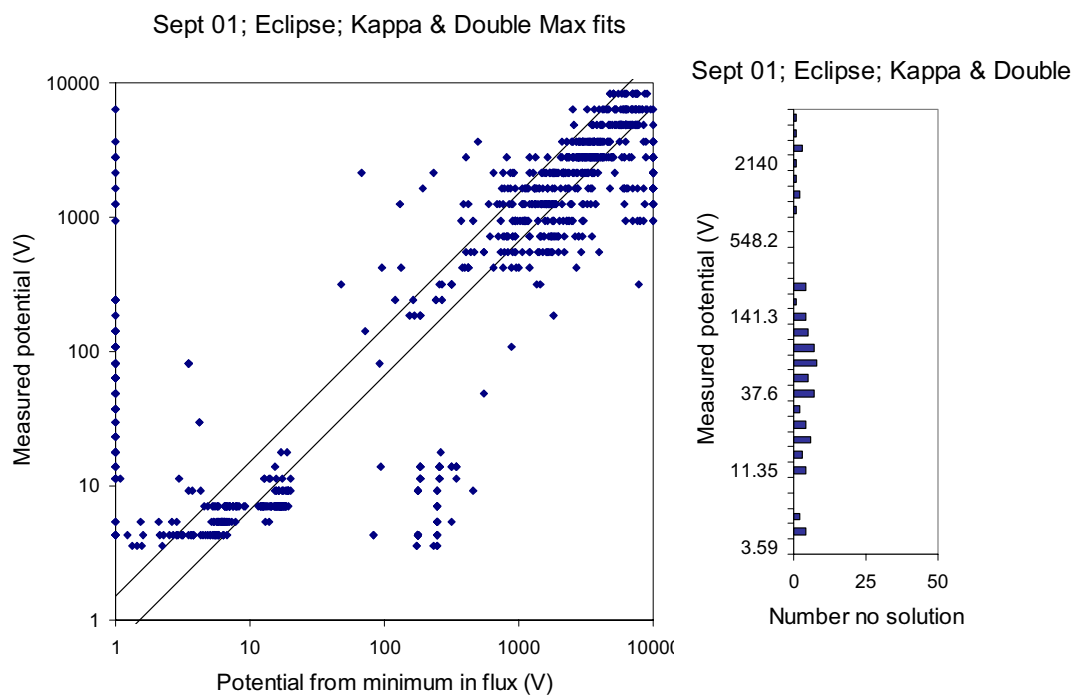


Figure 136. Measured potential computed from the minimum in the net flux, where the fluxes are computed from a Kappa fit to the electron flux and a Double Maxwellian fit to the ion flux.

Sept 01; Eclipse; Kappa & Max fits

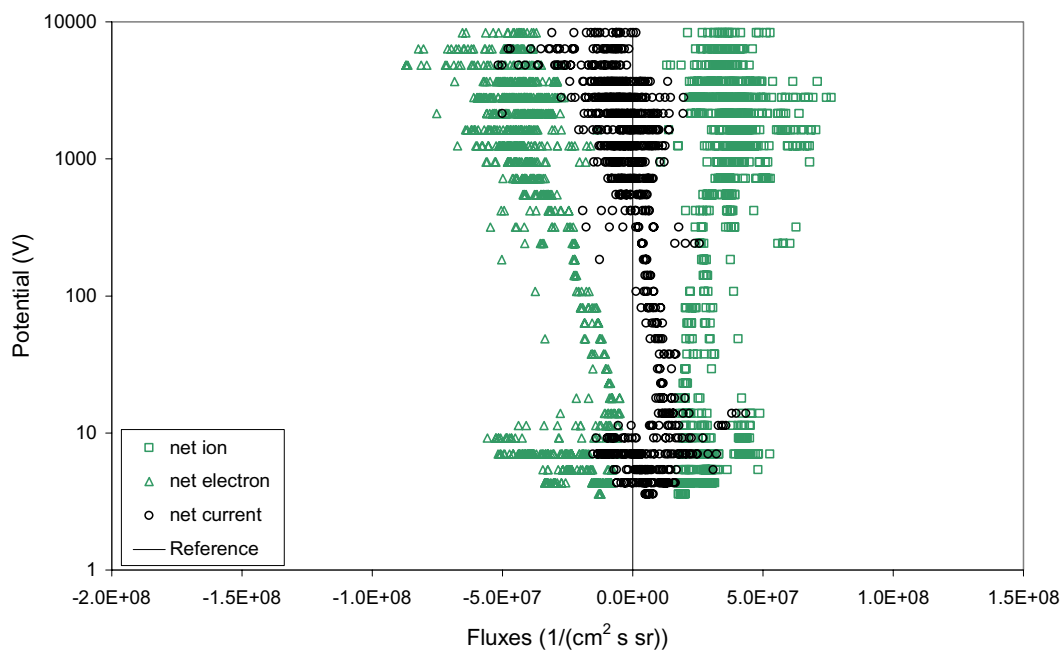


Figure 137. Net fluxes in eclipse at all potentials with electron fluxes computed from Kappa fit and ion fluxes computed from Kappa fit. Integral extends from 1 eV to 100 keV.

Table 2. Quality of potential predictions made from various fits to measured incident fluxes.

Electron fit	Ion fit	Number with no match	Average error	Number within factor of 1.5	Number within factor of 3
Maxwellian	Maxwellian	338	0.37	384	599
Maxwellian	Single Maxwellian	182	0.897	288	604
Maxwellian	Double Maxwellian	307	0.479	322	527
Maxwellian	Kappa	263	0.478	187	344
Single Maxwellian	Maxwellian	194	0.669	564	692
Single Maxwellian	Single Maxwellian	152	1.466	449	684
Single Maxwellian	Double Maxwellian	243	0.777	349	605
Single Maxwellian	Kappa	304	0.1417	169	343
Double Maxwellian	Maxwellian	239	0.642	484	654
Double Maxwellian	Single Maxwellian	207	1.22	346	70
Double Maxwellian	Double Maxwellian	257	0.707	300	597
Double Maxwellian	Kappa	251	0.1535	182	375
Kappa	Maxwellian	102	0.362	634	774
Kappa	Single Maxwellian	69	0.388	455	822
Kappa	Double Maxwellian	134	0.36	459	712
Kappa	Kappa	165	0.112	230	457

Table 3. Comparison of the accuracy of potential predictions from the fits when the flux integrals was done using only those energy bins used to create the flux and when the flux integrals extended from 1 eV to 100 keV.

Electron fit	Ion fit	Bins summed	Number with no match	Average error	Number within factor of 1.5
Maxwellian	Maxwellian	1 to 100 keV	338	0.37	384
Maxwellian	Maxwellian	Same as data	342	0.84	336
Single Maxwellian	Single Maxwellian	1 to 100 keV	152	1.466	449
Single Maxwellian	Single Maxwellian	Same as data	152	1.71	393
Double Maxwellian	Double Maxwellian	1 to 100 keV	257	0.707	300
Double Maxwellian	Double Maxwellian	Same as data	133	0.778	494
Kappa	Maxwellian	1 to 100 keV	102	0.362	634
Kappa	Maxwellian	Same as data	106	0.469	665
Kappa	Kappa	1 to 100 keV	165	0.112	230
Kappa	Kappa	Same as data	70	0.177	298

11 References

- S.J. Bame, D.J. McComas, M.F. Thomsen, B.L. Barraclough, R.C. Elphic, J.P. Glore, and J.T. Gosling, Magnetospheric plasma analyzer for spacecraft with constrained resources, *Rev Sci Instrum* 64, p 1026, 1993.
- C.F. Barnett, J.A. Ray, E. Ricci, M.I. Wilker, E.W. McDaniel, E.W. Thomas, H.B. Gilbody, *Atomic data for controlled fusion research*, Oak Ridge National Laboratory, Tennessee, (ORNL-5207, 1977.
- H. Bruining, Philips, *Technical Review*. 3, p. 80, 1938.
- S.P. Christon, D.J. Williams, and D.G. Mitchell, L.A. Frank, C.Y. Huang, Spectral characteristics of plasma sheet ion and electron populations during undisturbed geomagnetic conditions, *J. Geophys. Res.* 94, A10, p 13,409, 1989.
- S.P. Christon, D.J. Williams, and D.G. Mitchell, C.Y. Huang, L.A. Frank, Spectral characteristics of plasma sheet ion and electron populations during disturbed geomagnetic conditions, *J. Geophys. Res.* 96, A1, p 1, 1989.
- V.A. Davis, L.F. Neergaard, M.J. Mandell, I. Katz, B.M. Gardner, J.M. Hilton, J. Minor, Spacecraft Charging Calculations: NASCAP-2K and SEE Spacecraft Charging Handbook, 40th AIAA Aerospace Sciences Meeting and Exhibit, AIAA 2002-0626, 2002.
- B. Feuerbacher and B. Fitton, Experimental Investigation of Photoemission from Satellite Surface Materials, *J. Appl. Phys.* 43, 1563, 1972.
- H.B. Garrett, D.C. Schwank, P.R. Higbie, D.N. Baker, Comparison between the 30 to 80 keV electron channels on ATS 6 and 1976-059A during conjunction and application to spacecraft charging prediction, *JGR* 85, p 1155, 1980
- H. Goldstein, *Classical Mechanics*, Addison-Wesley Publishing Company, Inc. Massachusetts, p. 267, 1950a.
- H. Goldstein, *Classical Mechanics*, Addison-Wesley Publishing Company, Inc. Massachusetts, p. 67-68, 1950b.
- J. Holzl and K. Jacobi, *Surface Science*, 14, p 351, 1969.
- I. Katz, J.J. Cassidy, M.J. Mandell, G.W. Schnuelle, P.G. Steen, J.C. Roche, The Capabilities of the NASA Charging Analyzer Program, *Spacecraft Charging Technology-1978*, NASA CP-2071, AFGL-TR-79-0082, edited by R.C. Fincke and C.P. Pike, P. 101, 1979.
- I. Katz, V.A. Davis, M.J. Mandell, B.M. Gardner, J.M. Hilton, J. Minor, A.R. Fredrickson, D.L. Cooke, Interactive Spacecraft Charging Handbook with Integrated Updated Spacecraft Charging Models, 38th Aerospace Sciences Meeting and Exhibit, AIAA 2000-0247.

N. A. Krall and A. W. Trivelpiece, *Principles of Plasma Physics*, San Francisco Press, Inc., California, p. 447, 1986.

S.T. Lai, D. J. Della-Rose, Spacecraft charging at geosynchronous altitudes: new evidence of existence of critical temperature, *J Spacecr* 38, p. 922, 2001

L. N. Large and W. S. Whitlock, Secondary Electron Emission from Clean Metal Surfaces Bombarded by Fast Hydrogen Ions, *Proceedings of the Physical Society* 79, p 148, 1962.

D.J. Lawrence, M.F. Thomsen, J.E. Borovsky, and D.J. McComas, Measurements of early and late-time plasmasphere refilling, *JGR*, 104, p 14691, 1999

D.J. McComas, S.J. Bame, B.L. Barraclough, J.R. Donart, R.C. Elpheric, J.T. Gosling, M.B. Moldwin, K.R. Moore, and M.F. Thomsen, Magnetospheric plasma analyzer: initial three-spacecraft observations from geosynchronous orbit, *JGR*, 98, p 13453, 1993

W. H. Press, S. A. Teukolski, W. T. Vetterling, B. P. Flannery, *Numerical Recipes in C, The Art of Scientific Computing*, 2nd Edition, Cambridge University Press, 1992.

M. F. Thomsen, D. J. McComas, G.D. Reeves, and L.A. Weiss, An observational test of the Tsyganenko (T89a) model of the magnetospheric field, *JGR* 101, p. 24827, 1996

M.F. Thomsen, E. Noveroske, J.E. Borovsky, D.J. McComas, Calculation of moments from measurements by the Los Alamos Magnetospheric Plasma Analyzer, LA-13566-MS, 1999

REPORT DOCUMENTATION PAGE			Form Approved OMB No. 0704-0188	
Public reporting burden for this collection of information is estimated to average 1 hour per response, including the time for reviewing instructions, searching existing data sources, gathering and maintaining the data needed, and completing and reviewing the collection of information. Send comments regarding this burden estimate or any other aspect of this collection of information, including suggestions for reducing this burden, to Washington Headquarters Services, Directorate for Information Operation and Reports, 1215 Jefferson Davis Highway, Suite 1204, Arlington, VA 22202-4302, and to the Office of Management and Budget, Paperwork Reduction Project (0704-0188), Washington, DC 20503				
1. AGENCY USE ONLY (Leave Blank)	2. REPORT DATE October 2003	3. REPORT TYPE AND DATES COVERED Contractor Report		
4. TITLE AND SUBTITLE Characterization of Magnetospheric Spacecraft Charging Environments Using the LANL Magnetospheric Plasma Analyzer Data Set		5. FUNDING NUMBERS H-32492		
6. AUTHORS V.A. Davis, M.J. Mandell, and M.F. Thomsen				
7. PERFORMING ORGANIZATION NAMES(S) AND ADDRESS(ES) Science Applications International Corporation 10260 Campus Point Drive, M/S A-3 San Diego, CA 92121		8. PERFORMING ORGANIZATION REPORT NUMBER M-1089		
9. SPONSORING/MONITORING AGENCY NAME(S) AND ADDRESS(ES) NASA's Space Environments and Effects (SEE) Program George C. Marshall Space Flight Center Marshall Space Flight Center, AL 35812		10. SPONSORING/MONITORING AGENCY REPORT NUMBER NASA/CR-2003-212745		
11. SUPPLEMENTARY NOTES Prepared for NASA's Space Environments and Effects (SEE) Program by Science Applications International Corporation (SAIC) Technical Monitor: Donna Hardage, NASA Marshall Space Flight Center, 256-544-2342				
12a. DISTRIBUTION/AVAILABILITY STATEMENT Unclassified-Unlimited Subject Category 88 Availability: NASA CASI (301)621-0390			12b. DISTRIBUTION CODE	
13. ABSTRACT (Maximum 200 words) An improved specification of the plasma environment has been developed for use in modeling spacecraft charging. It was developed by statistically analyzing a large part of the LANL Magnetospheric Plasma Analyzer (MPA) data set for ion and electron spectral signature correlation with spacecraft charging, including anisotropies. The objective is to identify a relatively simple characterization of the full particle distributions that yield an accurate predication of the observed charging under a wide variety of conditions.				
14. SUBJECT TERMS plasma, charging, ions, electrons, flux, density, chassis, energy, Maxwellian, potential			15. NUMBER OF PAGES 111	
			16. PRICE CODE	
17. SECURITY CLASSIFICATION OF REPORT Unclassified	18. SECURITY CLASSIFICATION OF THIS PAGE Unclassified	19. SECURITY CLASSIFICATION OF ABSTRACT Unclassified	20. LIMITATION OF ABSTRACT Unlimited	